ISBN 978-82-326-3281-0 (printed version)
ISBN 978-82-326-3281-7 (electronic version)
ISSN 1503-8181

Doctoral theses at NTNU, 2018:245

Il Woong Park

Two-phase Flow Instabilities during Flow Boiling and Control of Wettability by Micro-structured Surfaces

NTNU
Norwegian University of
Science and Technology
Faculty of Engineering
Department of Energy and Process Engineering

NTNU
Norwegian University of
Science and Technology

Doctoral Thesis
Il Woong Park
Doctoral theses at NTNU, 2018:245
NTNU

NTNU
Norwegian University of
Science and Technology

Il Woong Park

Two-phase Flow Instabilities during Flow Boiling and Control of Wettability by Micro-structured Surfaces

Thesis for the degree of Philosophiae Doctor

Trondheim, September 2018

Norwegian University of Science and Technology
Faculty of Engineering
Department of Energy and Process Engineering

NTNU
Norwegian University of
Science and Technology

NTNU
Norwegian University of Science and Technology

Thesis for the degree of Philosophiae Doctor

Faculty of Engineering
Department of Energy and Process Engineering

ISBN 978-82-326-3281-0 (printed version)
ISBN 978-82-326-3281-7 (electronic version)
ISSN 1503-8181

Doctoral theses at NTNU, 2018:245

Printed by Skipnes Kommunikasjon as

Abstract

Boiling heat transfer is of relevance in a variety of applications in power and process industries. In spite of the vast research performed in the last decades, fundamental questions about mechanisms related to the boiling regime, heat transfer mechanisms, pressure drop and two-phase flow instabilities still remain unanswered. This thesis deals with two important points within boiling heat transfer: (i) the first part of the thesis is focused on understanding the dynamics of two-phase flow instabilities in small-diameter channels, in particular, pressure drop oscillations and their effect on the heat transfer coefficient; (ii) the second part of the thesis deals with manipulation of surface wettability by modification of the surface structure its effect on evaporative heat transfer, more precisely the Leidenfrost phenomenon.

In flow boiling systems, two-phase flow instabilities such as density wave oscillations and pressure drop oscillations have been identified as one of the impediments for achieving high heat flux due to the potential heat transfer deterioration. However, most of the fundamental characteristics of the two-phase flow instabilities and the mechanisms leading to the heat transfer deterioration remain uncharted. In this thesis, contradictions between previous studies regarding the effect of the mass flux on amplitude and period of oscillations during pressure drop oscillations are clarified experimentally. A series of designed experiments are able to show the conditions for the interaction between density wave oscillations and pressure drop oscillations. Especially, it is shown that pure pressure drop oscillations can occur in a horizontal heated tube, something that has not been reported in previous studies. When both types of oscillations occur simultaneously, it is shown that the amplitude of the superimposed density wave oscillations on the pressure drop oscillations is controlled by the surge tank upstream of the test section. This previously unknown effect of the surge tank on the density wave oscillations contributes to improving the understanding of the complex dynamics of two-phase flow instabilities. Furthermore, the deterioration of the heat transfer coefficient under controlled flow oscillations is investigated. It is observed that the averaged heat transfer

coefficient can be deteriorated by flow oscillations. In particular, the deterioration is negligible until the amplitude of the oscillations become higher than a given threshold. Above this threshold, the deterioration is attributed to the dry-out of the wall during the low mass flux part of the oscillations. Based on these findings, it can be suggested that a severe deterioration of the flow boiling heat transfer coefficient can occur because of two-phase flow instabilities, but only when the amplitude of the oscillations is above a given threshold.

Looking more in the microscale level, when it comes to the enhancement of the heat transfer from the surface to the cooling fluid, recent progress in controlling the properties of the surfaces at the micro-nanoscale by micro/nano fabrication techniques has motived a vast amount of research. However, the effect of the micro-nanoscale surface properties into the overall performance remains an open question. In the second part of the thesis, a fabrication process for nature-inspired microstructures is introduced. By mimicking conical microstructures found in nature, which can present superhydrophilic and superhydrophobic properties, a broad range of surface wettability is obtained. The fabricated surfaces show that the wettability can be controlled by adjusting the geometric parameters of the microstructure without external excitation. Remarkably, a drastic wetting transition from the Cassie-Baxter to the Wenzel state is observed by varying the spacing between the microstructures. Furthermore, the effect of the surface topology and chemical coating on the surface wettability is investigated. Silanization and replication of the geometrical microstructures into polydimethylsiloxane (PDMS) are considered to modify the chemical composition of the surfaces and to keep the similar topography of the surfaces. It is shown that the wettability in the Cassie-Baxter state is determined by the geometrical aspect in the microscale while wettability in the Wenzel state is decided by the chemical aspect. Regarding heat transfer, enhancement of the Leidenfrost temperature on the microstructured surfaces is investigated. The tested microstructures are able to increase the Leidenfrost point. Differences between all the definitions of the Leidenfrost point found in the literature are investigated. It is observed that the difference between the Leidenfrost points which is less than 10K in the smooth surface can become larger up to 70K when microstructures exist. Results indicate that with a microstructured surface, not only can the Leidenfrost be shifted to higher temperatures but phenomenological differences compared to what is observed on smooth surfaces occur, namely the observation of the transition film boiling regime.

Acknowledgements

First, I express my sincere respect for Professor Carlos Alberto Dorao and Professor Maria Fernandino, with whose help I could acquire an advanced perspective on not only research but also life in general. I believe that this perspective will inspire me to conduct interesting studies in the future. Second, I am deeply grateful to Professor Carlos Alberto Dorao and Professor Maria Fernandino for efficiently supervising my work. Your support and encouragement made all the activities of my thesis work very interesting. I offer my thanks to Manuel, Espen, Jonas, Marcel, Han, Wenwu, Wenjing, Nicolas, and Ezequiel, as well. I am delighted to have worked with such great colleagues. In addition, I am thankful to Professor Tomasz Muszyński and Professor Rafal Andrzejczyk for collaborating with me in my research efforts. I would like to thank to Professor G. C. Park, Professor H. K. Cho, Professor E. S. Kim and Professor Y. G. Lee. Further, I express my gratitude to the administrators and technical staff of the Department of Energy and Process Engineering. In particular, regarding the experimental facility, I sincerely thank Reidar Tellebon and Aung Myo Oo Mon. In addition, I thank NTNU NanoLab. Although NanoLab is not a cozy place to live, I could perform fabrication because of the institution's helpful staff. I gratefully acknowledge the PhD fellowship granted by the NTNU-SINTEF Gas Technology Centre. I further acknowledge the Research Council of Norway for the support they offered to the Norwegian micro- and nano-fabrication facility NorFab. Moreover, I extend special thanks to the members of KSSEA, PES players, the curling team, the OW team in Trondheim, and my friends in Korea and Norway. In particular, I wish Hyunwoo, Seonah, Seoungyu and Yu Hwan a beautiful future.

Finally, I express my infinite love to my father, mother, brother, and Jeongrim.

Il Woong

Trondheim, Norway

Table of Contents

List of Figures

List of Publications

Part I

1. Park, I. W., Fernandino, M., and Dorao, C. A. (2018) Experimental study on the characteristics of pressure drop oscillations and interaction with short-period oscillation in a horizontal tube. *International Journal of Refrigeration*, 91, 246.
2. Park, I. W., Fernandino, M., and Dorao, C. A. (2018) On the occurrence of superimposed density wave oscillations on pressure drop oscillations and the influence of a compressible volume. *AIP Advances,* 8, 075022.
3. Park, I. W., Fernandino, M., and Dorao, C. A. (2018) Effect of the pressure drop oscillation on the local heat transfer coefficient in a heated horizontal pipe. *ASME 2018 16th International Conference on Nanochannels, Microchannels, and Minichannels.* American Society of Mechanical Engineers. June 10-13, 2108, Dubrovnik, Croatia.
4. Park, I. W., Ryu, J., Fernandino, M., and Dorao, C. A. Can flow oscillations during flow boiling deteriorate the heat transfer coefficient? (Submitted)

Part II

5. Park, I. W., Fernandino, M., and Dorao, C. A. (2018) Wetting State Transitions over Hierarchical Conical Microstructures. *Advanced Materials Interfaces*, 5, 1701039. (This paper is selected as an Inside Front Cover of the journal.)

6. Park, I. W., Jonas, M., Fernandino, M., and Dorao, C. A. Can the wettability be transferred while the topography is replicated?: Bioinspired conical microstructures from silicon to PDMS. (Submitted)
7. Park, I. W., Fernandino, M., and Dorao, C. A. (2016) Effect of Micropillar Characteristics on Leidenfrost Temperature of Impacting Droplets. ASME 2016 14th International Conference on Nanochannels, Microchannels, and Minichannels collocated with the *ASME 2016 Heat Transfer Summer Conference and the ASME 2016 Fluids Engineering Division Summer Meeting.* American Society of Mechanical Engineers. June 10-14, 2016, Washington DC, USA.

Additional publications

8. Park, I. W., Fernandino, M., and Dorao, C. A. (2015) Effect of the Mass Flow Rate and the Subcooling Temperature on Pressure Drop Oscillations in a Horizontal Pipe. *24th International Conference Nuclear Energy for New Europe.* September 14-17, Portoroz, Slovenia.
9. Park, I. W., Fernandino, M., and Dorao, C. A. (2017) Study of the Wetting Characteristics of Patterned Silicon Micro Conical Structure. *ASME 2017 15th International Conference on Nanochannels, Microchannels, and Minichannels*. American Society of Mechanical Engineers. August 27-30, 2017, Cambridge, USA.
10. Park, I. W., Fernandino, M., and Dorao, C. A. (2018). Controlling the wetting state with bio-mimetic hierarchical conical microstructures. *ASME 2018 16th International Conference on Nanochannels, Microchannels, and Minichannels.* American Society of Mechanical Engineers. June 10-13, 2108, Dubrovnik, Croatia.

Nomenclature

f	Fraction of the surface
G	Mass flux [kg/m^{2}s]
h	Heat transfer coefficient [W/m^{2}K]
k	Thermal conductivity [W/mK]
P	Pressure [Pa]
q	Heat flux [W/m^2]
r	Ratio of the contact area
T	Temperature [K]
x	Vapour quality
z	Distance from the inlet [m]
γ	Surface tension [N/m]
θ	Contact angle [^{o}]

Subscripts

0	Expansion tank
1	Measurement point 1
2	Measurement point 2
Cassie	Cassie-Baxter model
CB	Convective boiling
LA	Liquid-air

LS	Liquid-solid
NB	Nucleate boiling
SA	Solid-Air
SL	Solid-liquid
Sat	Saturation
W	Wall
Wenzel	Wenzel model
Y	Young model

Chapter 1 Introduction

Two-phase flow boiling can be found in systems such as cryogenic heat exchanger [1], nuclear reactors [2] and electronic devices [3]. While two-phase flow boiling can show high heat transfer coefficients compared to single-phase flow, two-phase flow instabilities can be observed [4–7]. Two-phase flow instabilities can result in oscillations in temperature and flow which can cause loss of control, thermal fatigue, system breakdown and deterioration of the heat transfer. Among the types of two-phase flow instabilities, density wave oscillations and pressure drop oscillations, which can be characterized by high and low frequency oscillations respectively, have been mostly studied [4–8]. Even though a considerable amount of studies have been conducted in the last half-century, there are still open questions regarding both types of oscillations.

In the case of density wave oscillations, the mechanisms for their occurrence have been suggested in previous studies. However, a general description for different working conditions has not been achieved [7]. For pressure drop oscillations, it has been reported that the characteristics of the oscillations are related with the steady state behavior of the system, compressible volume, flow inertia and thermal capacity of the wall [8]. Even though a sufficiently large compressible volume is an essential condition for the occurrence of pressure drop oscillations, the effect of the compressible volume in the characteristics of the oscillations remains unknown. Furthermore, an effective method to control or suppress the oscillations has not been developed [7]. A particular problem that remains not well understood is related to the interactions between the instabilities and the heat transfer performance under two-phase flow instabilities [6]. An example of this is the case of the occurrence of superimposed density wave oscillations on pressure drop oscillations in a horizontal tube. In particular, pure pressure drop oscillations without superimposed density wave oscillation have not been reported in a horizontal tube, even though they can be observed in a vertical tube [9–11]. Although there have been studies of superimposed density wave oscillations [12–14], the mechanisms for their

occurrence have not been fully identified. Moreover, the large amplitude of the superimposed density wave oscillations compared with pure density wave oscillations has not been deeply studied, although it can be observed in previous studies [9–11].

Concerning the issue of heat transfer, deterioration of the heat transfer performance has been considered as one of the major drawbacks of two-phase flow instabilities. It is essential to evaluate the impact of the heat transfer deterioration under two-phase flow instabilities. This is because flow oscillations can trigger the premature critical heat flux which can cause the system breakdown [15]. Evaluation of the deterioration of the heat transfer under two-phase flow oscillations could give an idea about the margin for designing the system in two-phase flow boiling systems. However, only a few studies have focused on the effect of two-phase flow instabilities on the heat transfer coefficient [15–19]. In addition, which is the effect of the amplitude and period of the oscillations on the heat transfer coefficient remains uncovered.

Another topic that will be covered in this thesis is related to the control of the properties of the surfaces at the micro-nanoscale by micro-nano fabrication techniques. In the past decade, a vast amount of research has been focused on enhancing the heat transfer from the surface to the cooling fluid, in particular by modifying the surface properties. Recent studies have shown the possibility of controlling the wettability of the surface by micro-engineered surfaces [20–32], which in turn can result in heat transfer enhancement [25, 29–32]. However, the underlying physical mechanisms related to the heat transfer enhancement of the micro-nanoscale surface properties on the overall performance remain an open research question, Figure 1.1.

The control of the wettability is an important milestone for understanding its effect on heat transfer performance. However, how the wettability can be determined on micro-engineered surfaces has not been deeply elucidated. Experimental studies have been conducted to control the wetting state by an external excitation such as electricity or vibration [33–35]. However, such active control method for controlling the wetting state can present limitations in its application. So, it is important to understand the mechanisms that determine the wettability of the surface.

Recent progress in fabrication techniques for micro-engineered surfaces has allowed the precise control of the surface roughness regarding its shape and size [36–39]. This progress

is allowing to gain an unprecedented control of the surface wettability by obtaining surfaces with well-controlled geometrical parameters. Especially, the fabrication of microstructures by dry-etching could be difficult because it is the result of the combination of isotropic etching for sidewall profile and anisotropic etching for high aspect ratio between the height and width. Examples of some of the difficulties on dry-etching are presented in Appendix A. Further progress in microfabrication could allow the fabrication of nature-inspired surfaces with precise control of geometric parameters. In nature, surfaces with conical structures show a broad range of wettability [40]. For example, leaves of the lotus flower show superhydrophobicity for self-cleaning with droplets while the Ruellia devosiana leaf shows superhydrophilicity for the fast spreading of the water. Therefore, a broad range of wettability on nature-inspired surfaces with well-controlled geometric parameters of conical microstructures could be expected.

This thesis focuses on 1) two-phase flow instabilities in the macroscale and 2) control of wettability in the microscale. Further investigations on both subjects can contribute to the achievement of optimal design, stabilized control, and enhanced efficiency of the flow boiling concept with microstructures.

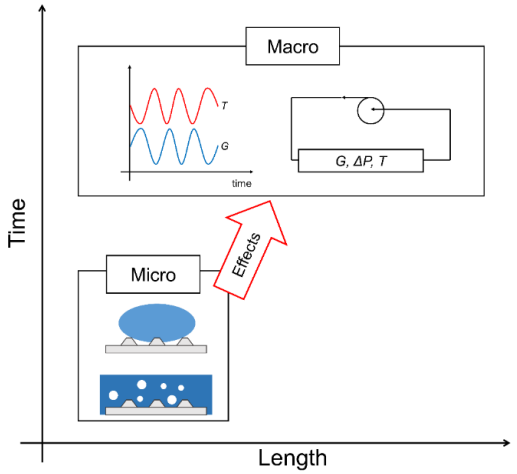

Figure 1.1 A modification in microscale for affecting the performance in macroscale

1.1 Objectives

The main goal of this thesis is to advance the understanding of the characteristics of two-phase flow instabilities and their impact on the heat transfer and to allow the development of designed micro-engineered surfaces with controlled wettability. The thesis is structured in two parts as follows.

For Part I, the main objectives are to identify the conditions for the occurrence of two-phase flow instabilities in a horizontal tube, in particular, the occurrence of superimposed density wave oscillations over pressure drop oscillations and the effect of the oscillations in the flow on the heat transfer performance. This part of the thesis will focus on the following issues:

- Identify the conditions for the interaction between instabilities
- Identify the mechanisms controlling superimposed density wave oscillations
- Quantify the deterioration of the heat transfer coefficient under pressure drop oscillations
- Quantify the deterioration of the heat transfer coefficient under oscillatory flow

For Part II, the main objectives are to investigate the wettability of micro-engineered surfaces and the possibility of enhancing the heat transfer performance of droplet impacting on a surface by micro-engineered surfaces. This part of the thesis will focus on the following issues:

- Development of bioinspired surfaces with controlled wettability
- Investigate the mechanisms of the Cassie–Wenzel wetting transition
- Investigate the control of the Leidenfrost temperature by micro-engineered surfaces.

1.2 Scope

For part I, experimental studies are conducted in an experimental facility with R134a as the working fluid, a horizontal test section with 5 mm of the inner diameter and 2m long. The details of the experimental facility are described in Appendix B. Conditions for the different types of two-phase flow instabilities are investigated by varying the inlet subcooling and the mass flux in short intervals. For Part II, the fabrication of bioinspired microstructures is considered as a first step. A characterization of the fabricated structures is conducted for identifying the wettability. Experiments of the Leidenfrost phenomenon on micro-engineered surfaces are performed for identifying the mechanisms behind the enhancement of the heat transfer.

1.3 Organization of the thesis

The structure is presented in Figure 1.2. The thesis is organized as follows:

- **Chapter 2: Theoretical Background.** This chapter presents a general introduction to two-phase flow instabilities, heat transfer in two-phase flow, the wettability of micro-engineered surfaces, and heat transfer enhancement in micro-textured surfaces.
- **Chapter 3: Two-phase flow instabilities and their influence on the deterioration of heat transfer.** This chapter presents the conditions for different modes of two-phase flow instabilities in a horizontal pipe. The mechanisms on the occurrence of the superimposed density wave oscillation and their large amplitude of oscillations of the mass flux are identified. Furthermore, deteriorations of the local heat transfer coefficient under pressure drop oscillations and controlled oscillatory conditions are presented.
- **Chapter 4: Control of wettability.** The fabrication of bio-inspired conical microstructures with well-controlled geometrical parameters on a silicon wafer is introduced. Wetting characteristics of the fabricated surfaces are investigated.

Furthermore, the dominant contribution for determining the wettability is discussed in terms of chemical and geometrical aspects.

- **Chapter 5: Enhancement of heat transfer.** The Leidenfrost point is measured in the micro-engineered surface. The nominal and dynamic Leidenfrost points and the non-wetting temperatures are compared.
- **Chapter 6: Conclusion and future work.** This chapter presents the conclusions and recommendations for future studies.

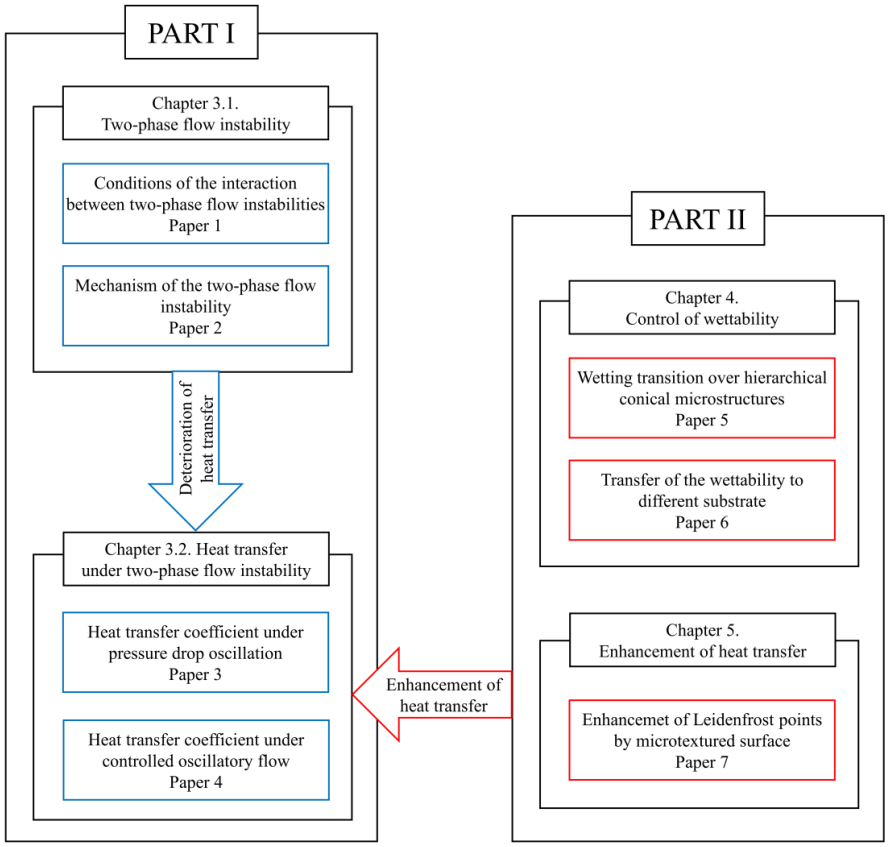

Figure 1.2 Structure of the thesis

Chapter 2 Background

2.1 Two-phase flow instabilities

Two-phase flow instabilities can be divided into two groups, namely static and dynamic instabilities. A distinction between the static instabilities and dynamic instabilities can be described as follows [6]. In static instabilities, a small perturbation causes the jump of the operating condition to a new operating condition. It occurs when the original operating condition is not in a stable equilibrium. On the other hand, in dynamic instabilities, multiple feedbacks of the flow conditions such as flow rate and pressure drop can be caused due to a sufficient interaction and a delayed feedback between the inertia of the flow and compressibility of the two-phase flow. Among the static instabilities, Ledinegg type instability is the most studied [8]. For the dynamic instabilities, density wave oscillations (DWO), pressure drop oscillations (PDO) and thermal oscillations are the most commonly occurring ones.

2.1.1 Density wave oscillations

Density wave oscillations are a particular case of two-phase flow instabilities. They can be explained by the delays from the transient distribution of the pressure drop. They occur when there is a difference in the densities of the liquid entering the channel and the two-phase mixture exiting the channel. The DWO can be triggered by a sudden perturbation of the pressure drop, which causes perturbation of the flow rate. A commonly accepted mechanism for the occurrence of the self-sustained oscillations is the following. Considering the case of a boiling channel, it is possible to assume that the channel has a constant pressure drop and that the inlet temperature of the fluid and the heat flux from the wall to the fluid are constant. A

single perturbation of the mass flux can result in a perturbation of the boiling boundary. This perturbation of the boiling boundary causes a change in pressure drop both in the single-phase and two-phase flow regions in the total heated pipe. Since the heated pipe has a constant pressure drop, this change in pressure generates a subsequent perturbation of opposite sign. Depending on the propagation speed, the existing oscillation of the pressure drop can cause subsequent oscillations. The process has also been described as the difference in the propagation speeds, which are the speed of sound in single-phase flow and the kinematic velocity in two-phase flow [41]. Which are the main parameters controlling the DWO and its effect on the frequency and amplitude of the oscillations remains not well understood. For example, it has been reported that the characteristics of the DWO can be affected by operating parameters of the system, such as the inlet pressure and inlet liquid temperature [42].

A large number of studies have been focused on the stability analysis of density wave oscillations [43–44]. For the analysis, stability maps with the phase-change number and the subcooling number have been considered. The maps present the threshold between the unstable region and stable region. However, stability maps can be affected when the operating conditions such pressure are varied [45]. For this reason, it is important to understand the fundamental underlying mechanisms controlling density wave oscillations in order to predict their occurrence in the various systems. However, there are only a few studies which focused on the mechanisms of density wave oscillations [42]. For example, it is possible to observe superimposed density wave oscillations on pressure drop oscillations [9–11]. However, which are the requisites for the occurrence of this phenomenon remains unclear. Furthermore, when density wave oscillations are superimposed on pressure drop oscillations, they have a larger amplitude of the mass flux oscillation compared with pure density wave oscillations. However, which are the mechanisms by which the density wave oscillation gets amplified in the presence of pressure drop oscillations remains not understood. Liu and Kakaç suggested that superimposed oscillations can be attributed to the complete boiling during pressure drop oscillations [12]. Menteş et al. explained that the superimposed density wave can be triggered by a sudden change in the mass flow rate which can be caused by crossing bubbles across the orifice in the inlet valve [13]. Yin et al. showed that density wave oscillations were not affected by the compressible volume while the occurrence of the pressure drop oscillations

compressible volume in the numerical study using linear frequency domain stability model [14]. Investigations on the interaction between two-phase flow instabilities and their characteristics are required for improving the understanding of the phenomenon.

2.1.2 Pressure drop oscillations

The essential conditions for pressure drop oscillations were presented in previous studies [4, 46]. They can be summarized as an existence of an expansion tank or compressible volume upstream of a heated tube, a negative slope of the part of the internal system characteristic curve, i.e. resembling an N-shape in pressure drop versus flow rate curve, and a steeper external characteristic curve than the negative slope of the part of the internal system characteristic curve.

A schematic diagram of the system and pressure drop versus mass flux curve are presented in Figure 2.1 as an explanation of the occurrence of pressure drop oscillations. The perturbation along the N-shape curve can be explained by the difference between the mass fluxes from the supply system and the heated section. If we assume that there is a positive perturbation of the inlet pressure from the unstable point U, the mass flux from the supply system becomes higher than that in the heated section. A higher mass flux in the supply system can cause an increase in the water level and an increase in the pressure in the expansion tank. Again, the pressure difference due to the difference in the mass flux triggers a greater difference between G_1 and G_2. This negative feedback continues until the system reaches point B. At this point, the system can reach a higher pressure when the flow follows the internal characteristic curve. Because of this, a flow excursion occurs and the system reaches point C. After this flow excursion, the flow that returns to the expansion tank leads the system to point D. In the case of the negative perturbation from the unstable point, because of the negative feedback between the mass flux and pressure, the system reaches point D. Moreover, the system reaches point B via A owing to the interaction between the expansion tank and heated section. This shows that a single perturbation from the unstable point can cause oscillations in mass flux and pressure along the generated limit cycle (A–B–C–D).

The essential conditions and the mechanism for the occurrence of pressure drop oscillations have been described above. However, some of the remaining research questions and suggestions for further studies on pressure drop oscillations were reviewed by Chiapero et al. [8]. Especially, it was mentioned that experiments for decoupling density wave oscillations and pressure drop oscillations in a horizontal channel would be helpful for understanding both types of oscillations. Furthermore, contradictions on the effect of the working conditions on the characteristics of the pressure drop oscillations in a horizontal tube have been reported [9–11]. For example, Yüncü et al. [9] reported that the amplitude and period decrease with increasing mass flux at low mass fluxes and increase with increasing mass flux at high mass fluxes. However, Çomaklı et al. [10] and Ding et al. [11] observed that the amplitude and period increase with increasing mass flux. These contradictions suggest that the complexity of pressure drop oscillations requires further investigation for identifying the mechanisms controlling their occurrence and characteristics.

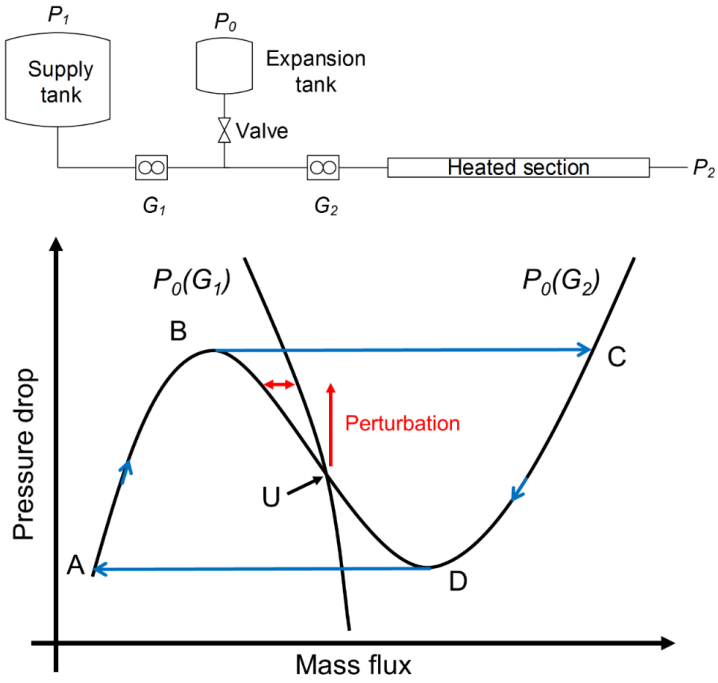

Figure 2.1 Schematic diagram for the mechanism of pressure drop oscillation

2.2 Heat transfer in oscillatory two-phase flows

Heat transfer in flow boiling has motived significant research in the past decade. Briefly, heat transfer during flow boiling can be summarized in Figure 2.2 [47]. In region A, the temperature of the wall and fluid increases simultaneously as the liquid is heated. In this region, heat is transferred by convective heat transfer through single-phase convective flow. These increases in temperatures continue until the wall reaches the temperature at which there is sufficient superheating for the nucleation of the bubbles. This point is the so-called onset of nucleate boiling (ONB) and subcooled boiling starts at this point. In region B, the wall temperature rises above the saturation temperature, nucleate boiling occurs in the superheated wall even though the liquid temperature is lower than the saturation temperature. From region C, saturated nucleate boiling can be established with the stabilized wall temperature and fluid temperature. Saturated boiling can be divided into the bubbly flow, slug flow, annular flow, and annular flow with droplets based on the flow patterns respectively in region C, D, E and F. This saturated boiling continues until dryout which represents the complete evaporation of the thin liquid film. In this point, the sudden jump of the wall temperature and superheating of the vapor take place. After this point, superheated vapor flows with liquid droplets in region G. It persists until the flow becomes single-phase vapor where all the droplets are evaporated.

The local two-phase flow boiling heat transfer coefficient can be determined by heat flux, wall temperature, and saturation temperature as:

$$h = \frac{q}{T_w - T_{sat}} \tag{2.1}$$

where q is the heat flux from the wall to fluid, T_w the wall temperature, and T_{sat} the saturation temperature of the fluid. In flow boiling, the heat transfer coefficient is commonly considered as a combination of a heat transfer coefficient for nucleate boiling (h_{NB}) and a heat transfer coefficient for convective boiling (h_{CB}) as:

$$h = f(h_{NB}, h_{CB}) \tag{2.2}$$

Nucleate boiling heat transfer refers to heat transfer from the nucleation, growth, and departure of bubbles. Convective boiling can be understood as the single-phase forced convection along a thin film. There have been numerous attempts to predict the heat transfer

coefficient as a combination of nucleate boiling heat transfer and convective boiling heat transfer, such as that by Chen [48], and Gungor and Winterton [49]. There have been attempts to adapt the prediction of the heat transfer for a vertical tube to the case of a horizontal tube, for example, by Shah [50] and Kandlikar [51]. The effect of flow patterns on the heat transfer was investigated in the earlier work by for instance Kattan et al. [52]. A correlation for the local heat transfer coefficient in a horizontal tube was developed including the effect of the flow pattern. Especially, the transition between the annular flow and stratified flow is considered in this model. The effect of the flow patterns on the heat transfer was schematically summarized by Kim and Mudawar [53]. The heat transfer coefficient along the flow patterns for dominant heat transfer in nucleate boiling and convective boiling is shown in Figure 2.3. In the condition of nucleate boiling dominant heat transfer, the heat transfer coefficient decreases following the tube distance from the inlet due to the suppression of nucleation. In the condition of convective boiling dominant heat transfer, the heat transfer coefficient increases along the tube due to the decrease of the thickness of the annular liquid film. In both conditions, the heat transfer coefficient apparently decreases after the dry-out. Further decrease of the heat transfer occurs until the dry-out completion which is referred to as critical heat flux. Dorao et al. have shown that the heat transfer coefficient during dominant convective flow boiling is equivalent to the single-phase flow heat transfer. This fact is attributed to the existence of a dominant thermal resistance close to the wall referred to as the conductive sublayer [54]. This result suggests that flow patterns are not having an influence on the heat transfer as the bubbles cannot interfere with the dominant thermal resistance. The result can be summarized in that the Nusselt numbers for single-phase flow and convective flow boiling become equivalent by assuming that the vapor affects the velocity of the two-phase flow.

In summary, the underlying physics of the heat transfer phenomena during flow boiling remains not well understood. The situation becomes more challenging during flow oscillations, and only a few studies have been conducted, although the deterioration of the heat transfer coefficient has been noted as one of the major drawbacks of two-phase flow instabilities [15]. Guo et al. studied the effect on the heat transfer coefficient under pressure drop oscillations in a helical tube [16]. In Figure 2.4, the characteristics of local heat transfer under pressure drop oscillations are depicted for a helical tube. It can be observed that heat transfer coefficient

reaches almost zero during the oscillations. In this condition, wall temperatures up to 400°C were observed which can be severe to the system. Sørum and Dorao investigated the effect of density wave oscillations on the heat transfer coefficient and critical heat flux [15]. It was observed that the presence of the density wave oscillations can cause the deterioration of the heat transfer coefficient. The effect of the density wave oscillations was more critical for low pressure, low mass flow rate, and low inlet temperature. Furthermore, premature critical heat flux about 10 % was observed with density wave oscillations. Chen et al. and Wang et al. [17–19] carried out experimental studies by using controlled flow oscillations with an amplitude below 30% of the mean mass flux. The studies show that there is no noticeable influence on the heat transfer coefficient when the mass flux oscillates. In summary, heat transfer in two-phase flow has been widely studied for predicting the heat transfer coefficient for different conditions such as configurations of the pipe and flow patterns, over the past decades. However, when we take into account two-phase flow instabilities, only a few studies have been conducted and which are the particular effects of the flow oscillations on the heat transfer remains not understood.

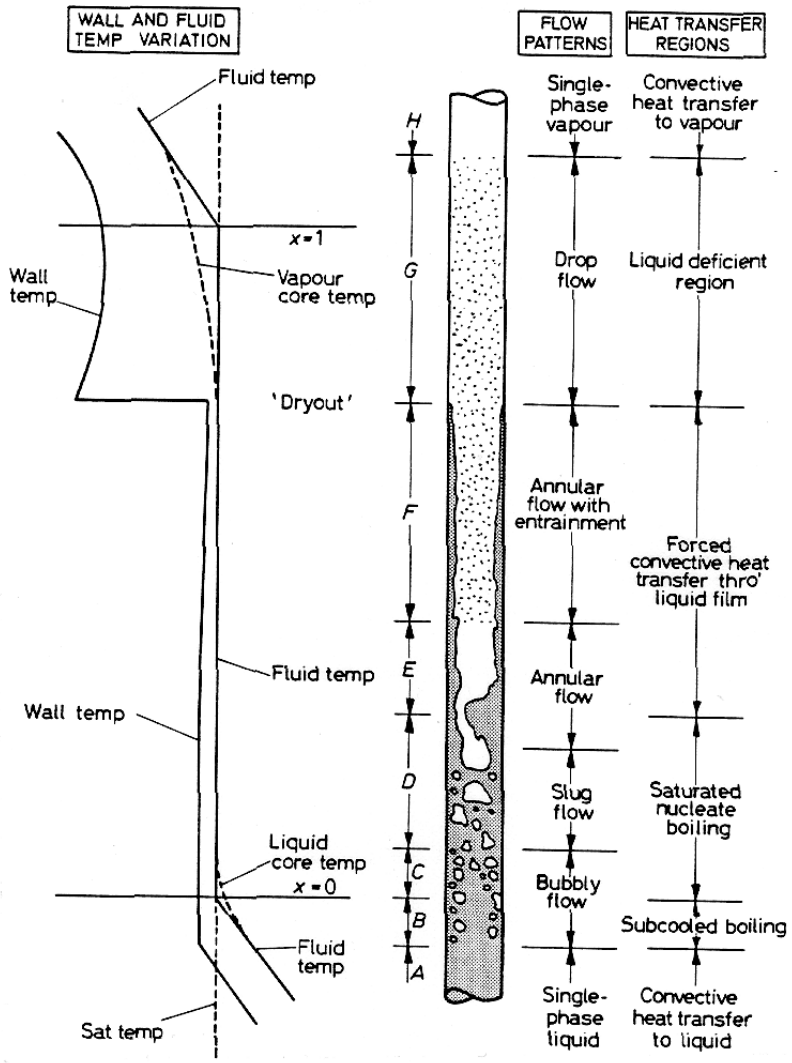

Figure 2.2 Schematic representation of convective boiling in a vertical tube [47]

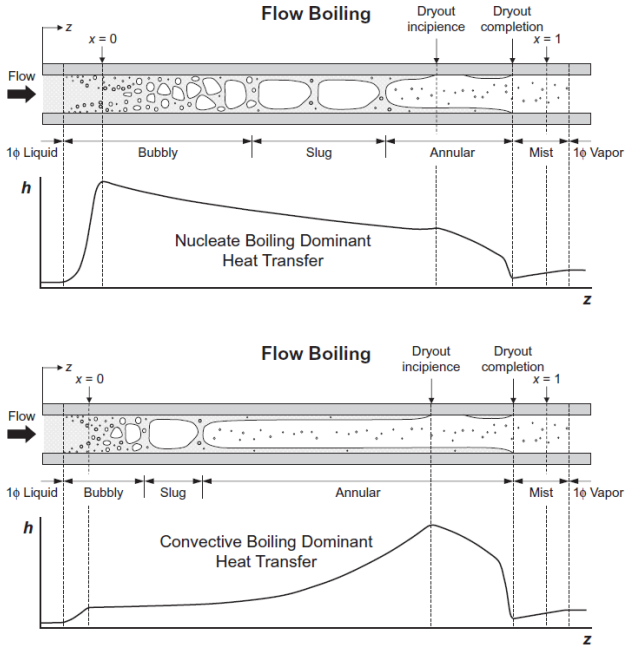

Figure 2.3 Heat transfer coefficient along the flow patterns for dominant heat transfer in nucleate boiling and convective boiling [53]

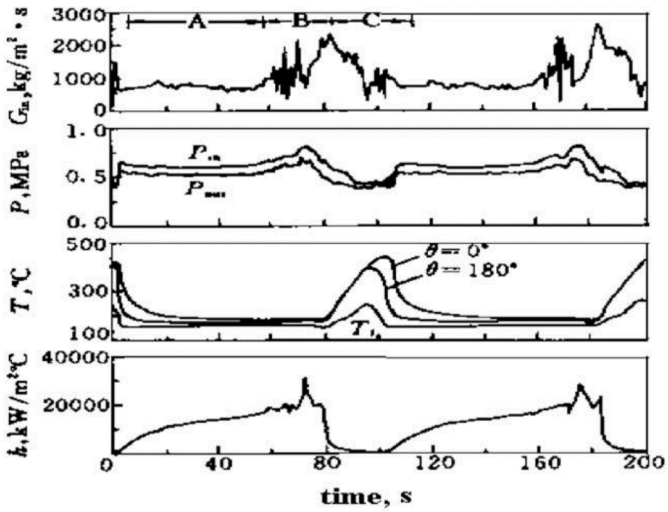

Figure 2.4 Characteristics of local heat transfer and main parameters under pressure drop oscillations in a helical tube [16]

2.3 Wettability of conical microstructures

An ideal surface assumes atomic and chemical homogeneity, non-reactivity, and non-deformability. The contact angle for the ideal surface can be characterized by the Young angle from the Young Equation [55]. The Young angle θ_Y can be written as:

$$cos\theta_Y = \frac{\gamma_{SA}-\gamma_{SL}}{\gamma_{LA}} \tag{2.3}$$

where γ_{SA}, γ_{SL}, and γ_{LA} are the surface tension at the solid-air, solid-liquid, and liquid-air interfaces, respectively.

In the case of surfaces with micro-nano structures, the Cassie-Baxter model and Wenzel model have been commonly considered for predicting the wettability of the surface. The Cassie–Baxter wetting model assumes trapped air in the pores on the solid surface [56]. The contact angle for the Cassie-Baxter state θ_{CB} can be presented as:

$$cos\theta_{Cassie} = -1 + f_{SA}(cos\theta_Y + 1) \tag{2.4}$$

where f_{SA} is the fraction of the solid and air surfaces.

For the Wenzel wetting model, the droplet wets the rough surface, which is chemically homogeneous [57]. The contact angle in Wenzel state θ_{Wenzel} can be written as:

$$cos\theta_{Wenzel} = r_{LS}cos\theta_Y \tag{2.5}$$

where r_{LS} is the ratio of the contact area between the liquid and solid to its projection on the horizontal plane. In this model, both the hydrophilic and hydrophobic states can be magnified by the surface roughness. It should be mentioned that both models have a limitation in predicting the shape of the structures, the volume of the droplet and external forces [58].

Recently, development of micro-nano fabrication techniques allows the fabrication of surfaces with controlled wetting properties by modifying the topography of the surface. In particular, the presence of microstructures on top of the surface has a major effect on the wettability [36–39]. Among possible shapes of microstructures, a conical shape of microstructures is chosen in this study, based on the existence of surfaces in nature with conical

topography that presents a broad range of wettability [40]. Moreover, fabricated conical structures with a second level of the roughness, which can be also observed in lotus leaves, have been reported as promising for achieving the superhydrophobic state [59–60].

Different methods for fabricating conical structures have been presented in previous studies [59–64]. SEM images of them are depicted in Figure 2.5–2.7. The methods for fabricating conical microstructures in the previous studies are introduced as follows. Zhang et al. reported colloidal lithography with SiO2 particle arrays [59]. In this method, reactive ion etching with a mask of colloidal particles is used to fabricate silicon cone arrays with controllable morphologies. Cones up to 1.5μm in height were reported. The roughness of the sidewall of conical structures can be controlled by the etching duration. The presented method allows control of the profile of the conical structures, but the fabrication of silica particles in the array as an additional process before the etching is required. Apparent contact angles of the fabricated samples are measured between 120 and 160 degrees depending on the etching duration. Chen et al. fabricated truncated microcones using a two-step wet etching process [60]. A pattern of photoresist was created for the array. Then the truncated microcones were fabricated by anisotropic wet-etching. Nanostructures were fabricated over the fabricated microcones by a metal-assisted chemical etching process. 23μm high microcones were reported. In this method, the aspect ratio between the height and diameter of the base is relatively low compared with the other microcones which are introduced in this chapter. After the silanization process, 165 degrees of apparent contact angle and less than 1 degree of contact angle hysteresis were measured in the fabricated surface. Kondrashov et al. fabricated microcones and nanograss in dual-scale roughness without any etching mask [61]. As a first step, microcones were fabricated by cryogenic deep reactive ion etching (DRIE) in the over-passivation regime. As a second step, nanograss were generated by the modified DRIE (Bosch) process. Cones of up to 35μm in height were reported. SF_6 and O_2 as etching gases were used for DRIE and SF_6, O_2, and C_4F_8 were used for modified DRIE. In this method, the diameter and height of the cones can be controlled by controlling the oxygen flow rate and cryogenic temperature, but the process does not allow the control of the distribution in the desired pattern. Fabricated microstructures with a dual-scale roughness presented an apparent contact angle higher than 150 degrees, while the pure nanograss with a fluoropolymer coating on top showed

an apparent contact angle around 179 degrees. Chen et al. reported the fabrication of cone-like structures [62] fabricated by plasma spray deposition of titania with the shielding plate of stainless steel mesh. As the following process, polytetrafluoroethylene/nano-copper composites were deposited by suspension flame spray over the patterned titania coating. However, this process has limited control of the morphology of the cones and topography of the surfaces. 152 degrees of the apparent contact angle was measured in the fabricated surface. Arce reported the fabrication of microstructures by using reactive ion etching [63]. A pattern for the microstructures was controlled by photolithography using OiR 907/17 photoresist. Different structures were fabricated by varying the ICP power, RF power, O_2 gas flow, and SF_6 gas flow. In particular, fabrication of one sample with conical structures of 8μm height was achieved. A parametric study can be helpful to find the conditions for the conical shape, but it is not possible to identify the effect of etching parameters on specific sidewall profile of microcones. Xue et al. fabricated microcones by reactive ion etching an inclined surface with well-defined and ordered microsphere polystyrene array [64]. From this method, geometrical parameters including diameter and height can be gradually varied in the surface. Microcones with less than 0.6 μm in height were reported. Even though the geometrical parameter can be decided by the position, further control of the parameters is limited by the size of the microsphere array. Apparent contact angles from 105 to 140 degrees were measured depending on the position. In summary, techniques for fabricating the microstructures with conical shape have been developed in the literature. However, most of these techniques present limitations regarding the control of the roughness of the sidewall of the conical structures and suppression of the randomly generated microstructures. For this reason, gaining control of the shape and geometrical parameters of the microstructures is an essential step for investigating and developing surfaces with controlled wettability.

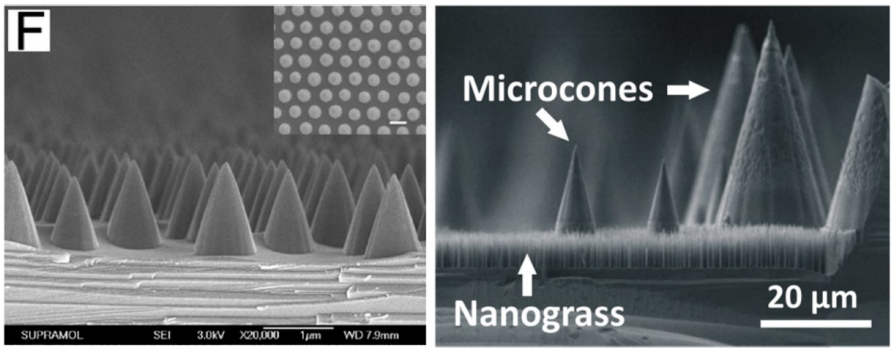

Figure 2.5 SEM images of conical microstructures [59] (left) and [61] (right)

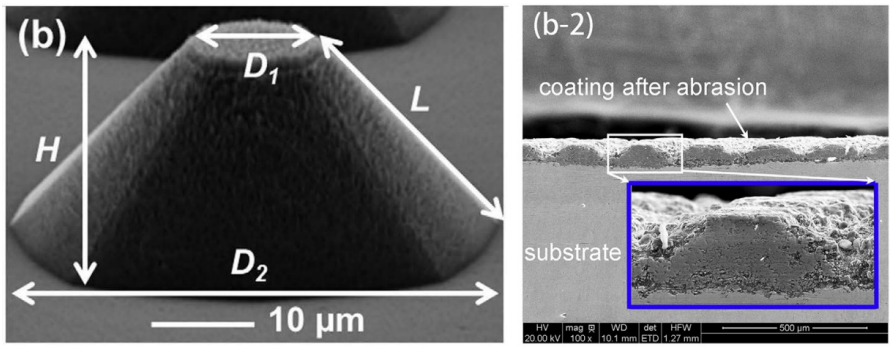

Figure 2.6 SEM images of conical microstructures [60] (left) and [62] (right)

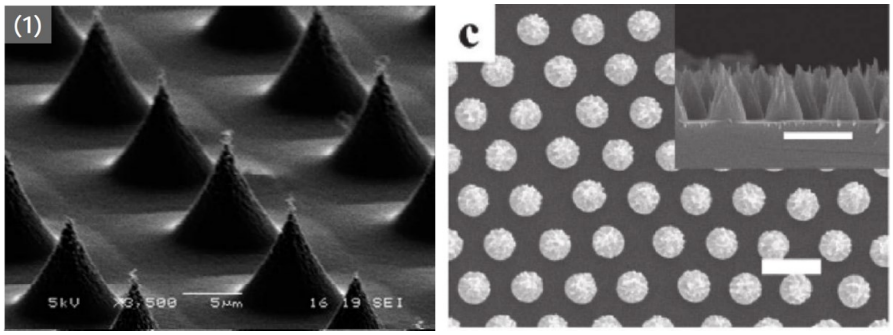

Figure 2.7 SEM images of conical microstructures [63] (left) and [64] (right)

2.4 Heat transfer enhancement by micro-engineered surfaces

Textured microstructured surfaces have been considered as a promising concept for enhancing the heat transfer. For example, the contact angle is considered as one of the important parameters for dryout and critical heat flux under flow boiling in a microchannel [65]. In particular in the case of droplet cooling, when the liquid droplet contacts a surface above the Leidenfrost point (LFP), the part of the droplet in contact with the surface vaporizes and creates an insulating vapor layer that keeps the droplet levitating and results in insufficient heat transfer between the liquid and surface. The LFP can be considered a method of estimating the thermal margin of spray cooling, even though it is based on the measurement of a single droplet. Recent studies fabricated micro/nano-engineered surfaces to increase the Leidenfrost temperature. Typical measurements of the LFP with micro or nanotextured surfaces are shown in Figure 2.8. It is expected that microstructure or nanostructures not only enhance the LFP but also reduce the droplet evaporation time under the LFP condition. Kim et al. carried out one of the first studies on the Leidenfrost effect with microstructured surfaces [25]. Fabricated silicon micropillars with nanoporous layers showed an LFP of 453 ^{o}C with a 13 µl water droplet. In further estimation, the height of the pillars and the thickness of the vapor film were compared, and the enhancement of the Leidenfrost temperature was explained by the re-initiation of the liquid-solid contact. Kwon et al. showed that micro-nano hierarchical surface structures can enhance the LFP from 270 to 370 ^{o}C with a 30 µl water droplet [26]. Micropillars in square arrays were fabricated in a silicon substrate. An increase in the Leidenfrost temperature, as well as an effect on droplet dynamics due to the micropillar, were observed. The results of the physical model for the balance of the capillary wetting pressure and vapour pressure are consistent with the experimental results. The following study suggests two parameters for deciding the shift of the Liedenfrost temperature. They are the capillary force which is related to the arrays of the microstructures, and the gap for the escaping vapor flow in terms of the pressure for the levitation of the droplet. Farokhinia et al. developed a decoupled hierarchical structure which shows an LFP higher than 570 ^{o}C with a 30 µl water droplet [66]. In this concept, a superhydrophilic nanomembrane and micropillars at high aspect ratios are considered for the two mechanisms for Leidenfrost temperature. The superhydrophilic nanomembrane assists the wetting of the droplet to the solid surface while the micropillars

supply the path for the vapor flow. Tran et al. investigated the effect of the micropillars on the dynamic Leidenfrost point [67]. They fabricated micropillars with different height and spacing between the pillars in a silicon wafer. In this study, the dynamic Leidenfrost point which can be determined by the minimum temperature of the surface which can cause an impinging droplet to bounce was considered [68]. It was observed that the dynamic Leidenfrost point is decreased with micropillars compared with a smooth surface. Previous studies show that the Leidenfrost point which is a thermal characteristic in macroscale can be affected by the structures in the micro-nano scale. However, the Leidenfrost points which were determined differently by the longest droplet evaporation time [25, 66], the minimum temperature for gentle film boiling [26] and minimum temperature for droplet impinging [67–68] becomes different from each other in the previous study [26]. Therefore, to determine the relation between these different definitions is an important step for benchmarking different studies. In short, it has been observed that the Leidenfrost point can be shifted by the presence of microstructures. However, how the microstructures affect the Leidenfrost point has not been fully identified. Furthermore, discrepancies in the reported enhancement in the heat transfer can be attributed to the different methods for determining the Leidenfrost point. Further studies are required in order to identify the effect of the microstructures on the Leidenfrost phenomenon.

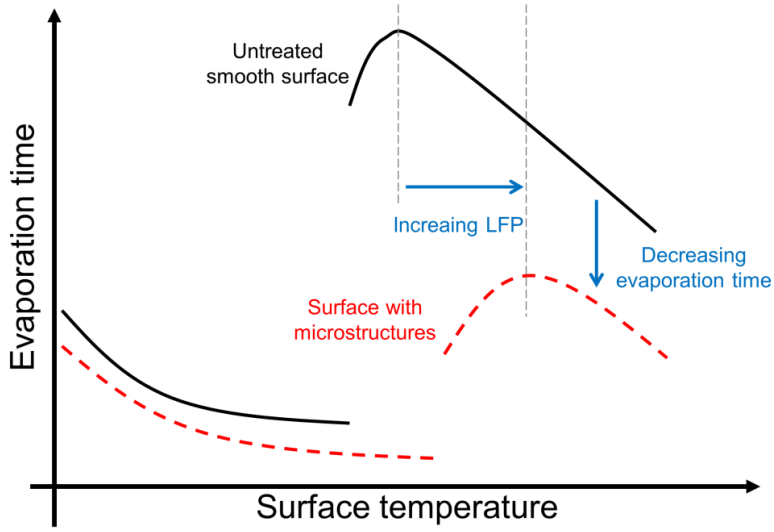

Figure 2.8 Enhancement of LFP by the micro-engineered surface

Chapter 3 Two-phase flow instabilities and deterioration of the heat transfer

3.1 Interaction between density wave and pressure drop oscillations (Papers 1 and 2)

Superimposed density wave oscillations over pressure drop oscillations (shown for example in Figure 3.1 [11]) have been previously reported and studied in the literature. However, there are discrepancies regarding their triggering mechanisms [12–14] and which parameters or operating conditions determine the characteristics of the pressure drop oscillations [9–11].

A further experimental investigation is required to clarify the characteristics of pressure drop oscillations in a horizontal tube. In **Paper 1**, an experimental study is conducted in order to clarify the discrepancies between previous studies, to investigate the occurrence of pure pressure drop oscillations in a horizontal tube and to obtain the limit cycles for different instability modes.

It is possible to observe that superimposed density wave oscillations have a large amplitude of mass flow, compared with the amplitudes of pure density wave oscillations or pure pressure drop oscillations. The reason for the larger amplitude of the superimposed density wave oscillations has not been clarified in the open literature. We assumed that the existence of the expansion volume or the flow oscillation has a dominant contribution to the occurrence of the superimposed density wave oscillations on the pressure drop oscillations and their larger amplitude. To investigate this, in **Paper 2** the flow oscillation of the pressure drop oscillations is mimicked by controlling the pump. With this experiment, the effect of oscillatory flow and the existence of the expansion tank can be decoupled in order to identify the possible superimposed density wave oscillations. The main finding in this work is that density wave oscillations can be superimposed on pressure drop oscillations when the mass flux changes

fast, while the amplitude of the mass flux oscillation during density wave oscillations can be amplified due to the upstream compressible volume. The wave shape of the pressure drop oscillations affects the existence of the superimposed density wave oscillations, while the existence of the compressible volume amplifies the amplitude of the density wave oscillations.

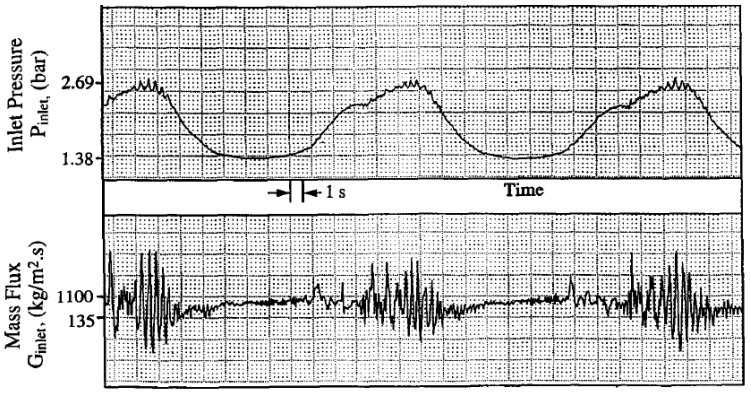

Figure 3.1 Example of the profiles of inlet pressure and mass flux under pressure drop oscillation in a horizontal tube [11]

Paper 1

Experimental study on the characteristics of pressure drop oscillations and interaction with short-period oscillation in a horizontal tube

Park, I. W., Fernandino, M., and Dorao, C. A.

International Journal of Refrigeration, 91, 246, 2018

International Journal of Refrigeration 91 (2018) 246–253

Contents lists available at ScienceDirect

International Journal of Refrigeration

journal homepage: www.elsevier.com/locate/ijrefrig

Experimental study on the characteristics of pressure drop oscillations and their interaction with short-period oscillation in a horizontal tube

Il Woong Park, Maria Fernandino, Carlos A. Dorao*

Department of Energy and Process Engineering, Norwegian University of Science and Technology, Trondheim, Norway

ARTICLE INFO

Article history:
Received 5 October 2017
Revised 7 May 2018
Accepted 9 May 2018
Available online 11 May 2018

Keywords:
Two-phase flow
Flow instability
R134a
Pressure drop oscillation
Density wave oscillation

ABSTRACT

Long-period oscillations (pressure drop oscillations) and short-period oscillations (superimposed density wave oscillations) have been observed in many studies. However, under which condition the long-period oscillations with superimposed short-period oscillations and long-period oscillations are occurring remains unknown particularly in horizontal systems. In this work, the occurrence of long-period oscillations with superimposed short-period and long-period oscillations are experimentally studied in a horizontal heated tube. It has been observed that long-period oscillations with superimposed short-period oscillations are apparently occurring in the middle of the negative slope of the pressure and mass flux internal system curve. Furthermore, as the inlet temperature subcooling is decreased the short-period oscillations disappear. Pressure drop–mass flux limit cycles are also shown for illustrating the interaction of the oscillations.

Étude expérimentale sur les caractéristiques des oscillations de chute de pression et leur interaction avec l'oscillation de courte période dans un tube horizontal

Mots-clés: Écoulement diphasique; Instabilité d'écoulement; R134a; Oscillation de la chute de pression; Oscillation de la densité des ondes

1. Introduction

Under high heat flux condition, subcooled flow boiling has the advantages of high heat transfer efficiency and high critical heat flux (Del Valle and Kenning, 1985; Vandervort et al., 1994; Yan et al., 2015). However, two-phase flow instabilities can occur in subcooled flow boiling system. A considerable amount of studies on two-phase flow instabilities has been conducted during the past decades (Boure et al., 1973; Durga Prasad et al., 2007; Kakac and Bon, 2008; Liang et al., 2010; Tadrist, 2007) due to its relevance to refrigeration, steam generators, boiling water reactors, etc. The main issue of the instabilities is the oscillations in temperature, flow, and pressure which can cause thermal fatigue, mechanical vibration, deterioration of heat transfer, and issues in the control of the system.

Among the types of the two-phase flow instabilities, a pressure drop oscillation (PDO) is characterized by a long period oscillation. This is an important phenomenon since it could trigger dry out in the multi-channel configuration (Kandlikar, 2002). The essential conditions for the occurrence of the PDOs were discussed in Boure et al. (1973) and Padki et al. (1992), which can be summarized like: the system has a compressible volume, the internal system characteristic curve presents a negative slope, i.e. resembling an N-shape, in terms of pressure drop versus flow rate curve, and the external characteristic curve is steeper than the negative slope of the internal characteristic curve. A negative slope of the internal characteristic curve can be observed when the outlet is in the two-phase flow condition.

PDOs have been studied theoretically (Doğan et al., 1983; Mawasha et al., 2001; Padki et al., 1992, 1991; Stenning and Veziroglu, 1965) and experimentally (Çomaklı et al., 2002; Ding et al., 1995; Guo et al., 1996; Ozawa et al., 1979; Yüncü et al., 1991) in the past decades. Recent studies on PDO have been reported in mini-channels (Yu et al., 2016) and microchannel system (Zhang et al., 2010). However, which are the mechanisms control-

* Corresponding author.
E-mail addresses: il.woong.park@ntnu.no (I.W. Park), carlos.dorao@ntnu.no (C.A. Dorao).

https://doi.org/10.1016/j.ijrefrig.2018.05.008
0140-7007/

Nomenclature

DP	pressure drop
G	Mass flux [Kg/m^{2}s]
P	Pressure [Pa]
T	Temperature [K]

Subscripts

l	Measurement point before the expansion tank
2	Measurement point after the expansion tank
B	Measurement point before the main tank
D	Down
F	Fluid
in	inlet
out	outlet
P	Measurement point after the pump
sub	subcooling
T	Measurement point inside the main tank
U	Up

ling the characteristics of the PDO and the impact of the oscillations on the heat transfer and pressure drop are not understood. Manavela Chiapero et al. (2012) have summarized previous studies and some of the remaining challenges on PDOs. In the case of horizontal pipes, parametric studies have been done to determine the effect of various parameters on the period and amplitude of the oscillations (Çomaklı et al., 2002; Ding et al., 1995; Yüncü et al., 1991). However, there are discrepancies between the previous studies regarding the effect of experimental conditions on the period and the amplitudes of PDO. Çomaklı et al. (2002) and Ding et al. (1995) have observed that the amplitude and period increase with increasing mass flux, while Yüncü et al. (1991) have reported that the amplitude and period increase with the mass flux at high mass fluxes and decrease with the mass flux at low mass fluxes.

PDOs have mostly been observed in the negative slope regions of the N-shape curve in previous studies but PDOs in the positive slope region have been reported by Çomaklı et al. (2002). In particular, under given conditions, the PDOs can show a superimposed high-frequency oscillation (Çomaklı et al., 2002; Ding et al., 1995; Yüncü et al., 1991). This high-frequency oscillation has been attributed to be density wave oscillations (DWO) triggered at the lowest region of the flow rate oscillation. Studies on the interaction between the PDO and DWO have been performed both experimentally (Liu and Kakac, 1991) and numerically (Schlichting et al., 2010; Yin et al., 2006). It has been observed that DWOs can be superimposed on the PDOs when the slope of the internal characteristic curve is negative (Liu and Kakac, 1991). It has been assumed that the DWOs occur during the passing through the left positive slope in the limit cycle causing a violent oscillation of the mass flux. Numerical studies have shown that the oscillation modes change in the sequence of pure DWO, transition, PDO with DWO, and pure PDO by increasing mass flux with constant inlet temperature condition (Yin et al., 2006).

Previous studies (Liu and Kakac, 1991; Manavela Chiapero et al., 2012) sketched the limit cycle for illustrating the PDOs and the superimposed DWOs as shown in Fig. 1. For the case of a pure PDO, the mechanism can be summarized as a compression in the expansion tank (A1–B), a flow excursion to liquid phase (B–C1), a decompression in the expansion tank (C1–D), and a flow excursion to gas phase (D–A1). On the other hand, for the case of a superimposed DWO and PDO, it has been suggested that it is occurring in the rising part of the pressure drop (A–B) when the complete boiling occurs (Liu and Kakaç, 1991) as shown in Fig. 1. In a previous study (Menteş et al., 1989), it is explained that

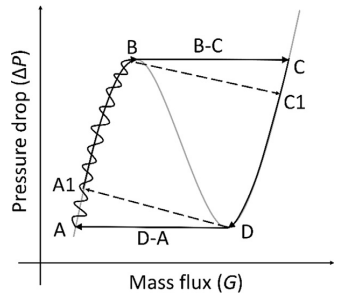

Fig. 1. Schematic diagram of limit cycle for the PDO (Manavela Chiapero et al., 2012) and the interaction between long-period oscillations and short-period oscillations in previous study (Liu and Kakac, 1991).

the occurrence of the superimposed DWOs under PDOs is triggered by bubbles which are passing through the orifice and causing a drop in the mass flow rate. The jump of the mass flow rate could cause the sudden change of the pressure by crossing the negative slope of the internal characteristic curve. Furthermore, the oscillation of the mass flow rate can be oriented by the sudden changes of the pressure and the inertia of the fluid. Schlichting et al. (2010) presented an alternative analysis of the interaction between PDOs and DWOs by using a transient lumped parameter model. However, it was observed that the limit cycle was not developed following the internal system characteristic curve in the given conditions for the analysis. Furthermore, only few research has been focused on the interaction between long-period and short-period (Yin et al., 2006), while only a few have considered the influence of the oscillations on the heat transfer and pressure drop.

Studying the shape of the limit cycle during the oscillation can help to understand the underlying mechanism of the interaction between pressure drop oscillations and short-period oscillations. The limit cycle might follow the internal characteristic curve during the phase of a flow excursion to liquid phase, a decompression in the expansion tank, and a flow excursion to the gas phase. The limit cycle under the interaction of the oscillation modes was reported by Schlichting et al. (2010) showing a large fluctuation of the mass flux after the flow excursion. Moreover, a non-linear interaction was observed in this previous analysis.

In summary, few studies have been investigating the occurrence of the long-period oscillation with superimposed short-period oscillation and the mechanisms controlling the interaction of the oscillations. In this study, the occurrence of the long-period oscillations with superimposed short-period oscillations is experimentally studied in a horizontal heated tube of 5 mm ID using R134a as working fluid.

2. Materials and methods

2.1. Experimental facility

The experimental facility for two-phase flow instability test consists of a closed main loop, a tank, a pump, a conditioner, a condenser, a test section, two flow meters, two chillers, and a visualization glass as shown in Fig. 2. R134a is used as the working fluid. A magnetically coupled gear pump is located between the main tank and the conditioner. The pressure and the temperature of the main loop are mainly controlled by the saturated conditions in the main tank. The conditions of the working fluid in the main tank are controlled by chillers connected to the condenser and conditioner in order to reach stable experimental conditions. The inlet fluid temperature and outlet fluid pressure are

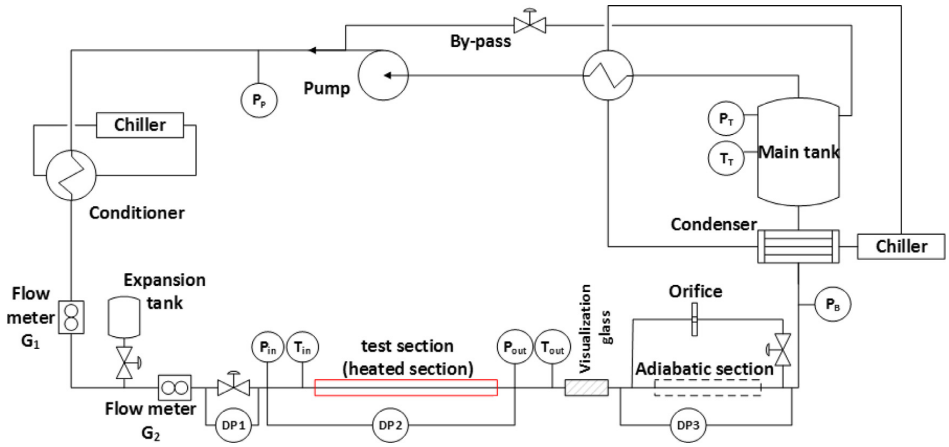

Fig. 2. Schematic diagram of the test facility.

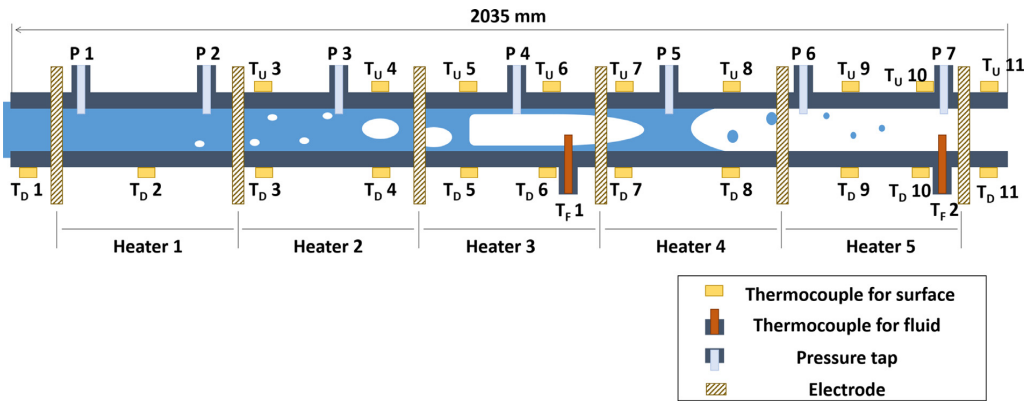

Fig. 3. Schematic diagram of the test section.

adjusted by two chillers connected to the conditioner and the condenser. Two Coriolis flow meters are located before the expansion tank (G_1) and after the expansion tank (G_2) for measuring the flow. The expansion tank is located above the closed main loop and before the test section. It has a 219 mm of diameter and 9.5×10^{-3} m^3 of volume. It is filled with R134a and nitrogen gas. The pressure and level of the expansion tank are controlled by a nitrogen tank which is connected to the top of the expansion tank. There is a manually operated valve between the expansion tank and the main loop in order to trigger the pressure drop oscillations.

The test section is a stainless steel tube has 5 mm inner diameter, 8 mm outer diameter and 2035 mm length. The schematic diagram of the heated channel is described in Fig. 3. The test section is heated electrically by electrodes in five independent sections and power input of each section is controllable. 9 and 11 thermocouples are installed on top and bottom of the test section, respectively. At two positions in the test section, there are two more thermocouples on both sides of the wall between thermocouples on the top and bottom. At these two positions, there are also thermocouples mounted inside the channel for measuring the fluid temperature directly. All the variables are logged with a National Instruments (NI) data acquisition system at an acquisition frequency of 10 Hz for all the measurements.

2.2. Measurements and accuracy

For the temperature measurements, 0.5 mm diameter T-type thermocouples have been used with an accuracy of 0.1 K (in-house calibration). The saturation temperature of the working fluid is determined by the absolute pressure transducers. Pressures at the inlet and the outlet of the test section are measured by absolute pressure transducers. They have a 0.04% accuracy at 2.5 MPa full-scale. The pressure drop between inlet and outlet of the test section is measured by a differential pressure transducer. It has a 0.075% accuracy at 0.05 MPa full-scale. The mass flow rate has a 0.2% accuracy. The accuracies of absolute pressure, pressure drop, and mass flow rate are given by the supplier. Heat flux is calibrated by means of heat transfer to the fluid in a stationary condition. For this, the input electrical power was sompared with the heat transfered between single-phase liquid and the surrounding. An accuracy of 3% is derived for the heat flux. The vapor quality along the test section is calculated based on an energy balance.

Table 1
A comparison of experimental conditions.

Parameter	Yüncü et al. (1991)	Çomaklı et al. (2002)	Ding et al. (1995)	This study
Fluid	R-11	R-11	R-11	R-134a
Inner diameter of test section	5 mm	11.2 mm	10.9 mm	5 mm
Length of test section	800 mm	3500 mm	1060 mm	2035 mm
System pressure	686,000 Pa	750,000 Pa	760,000 Pa	700,000 Pa
Mass flux (where PDO obtained)	200–560 kg/m^2 s	365–731 kg/m^2 s	240–900 kg/m^2 s	400–1000 kg/m^2 s
Heat flux	23–40 kW/m^2	121 kW/m^2	55–76 kW/m^2	35 kW/m^2
Inlet temperature	20 °C	16–28 °C	2–24 °C	−12 to −8 °C
Compressible volume	0.0084 m^2	0.05 m^3	0.0021 m^3	0.00471 m^3

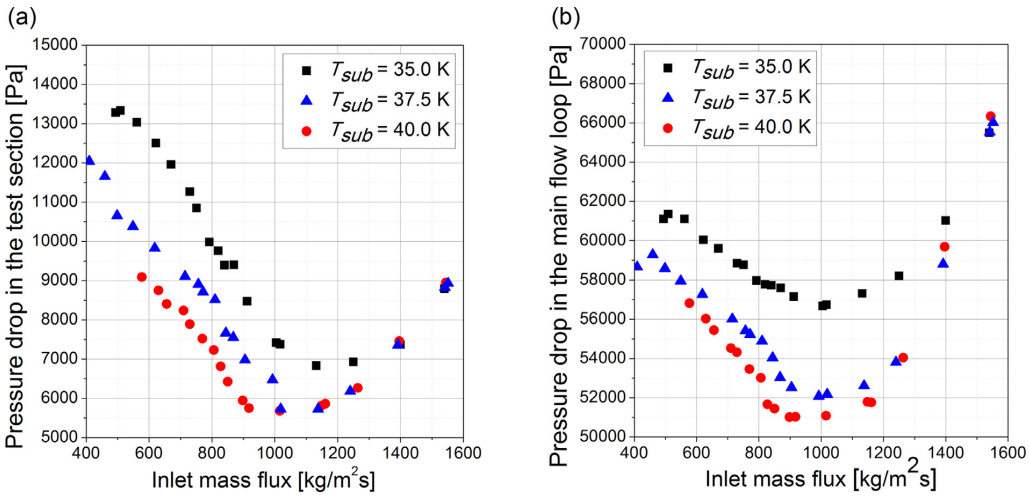

Fig. 4. N-shape curve of (a) the test section and (b) the main flow loop.

2.3. Experimental procedure and conditions

As a first step of the experimental procedure, the pump was started. In this step, sufficient flow was supplied for avoiding dry out in the test section. After obtaining a stable flow condition, a 35 kW/m^2 heat flux was gradually applied to the test section. By controlling the temperatures of the liquid in the chillers which are connected to the conditioner and the condenser, the inlet pressure (P_{in}, 700 kPa) and subcooling temperature (T_{sub}, 35.0, 37.5, and 40.0 K) were adjusted. The inlet mass flux (400–2000 kg/m^2 s) was adjusted by controlling the pump speed. In terms of the experimental conditions, it was not possible to reach the experimental condition for the low mass flux ($<$ 500 kg/m^2 s) with high subcooling temperature (40 K). That was because the minimum temperature (253.15 K) of the chiller connected to conditioner was not low enough in order to maintain high subcooling in a given condition. By adjusting temperatures of the chillers and the pump speed, the desired conditions were obtained for each test case. After this, pressure drop oscillations were triggered by opening the valve between the expansion tank and the test section. Table 1 shows a comparison of the experimental conditions with previous experimental studies on pressure drop oscillations in a horizontal channel.

For triggering the pressure drop oscillations, it was essential to obtain a negative slope in the internal system characteristic curve. Fig. 4a and b shows the internal system characteristic curves for the test section and the main flow loop for three subcooling temperatures. Negative slopes were observed in each subcooling temperature. For obtaining the internal system characteristic curve, the flow rate was decreased stepwise while the inlet pressure and subcooling temperature were maintained constant by controlling the temperature of the two chillers. The pressure drop in the main loop is obtained from the difference between the pressure after the pump (P_P) and before the main tank (P_B). The pressure drop in the test section is measured by the difference between the pressure before the test section (P_{in}) and after the test section (P_{out}).

3. Results and discussion

3.1. Different modes of instabilities

Fig. 5 summarizes the oscillation modes observed in this work in terms of the inlet mass flux and the subcooling temperature. The following oscillation modes were observed: no oscillation, decreasing long-period oscillations, long-period oscillations, and long-period oscillations followed by short-period oscillations. In particular, long-period oscillations refer to pure oscillations with a period longer than 30 s, while long-period oscillations followed by short-period oscillations refer to oscillations with a superimposed short-period oscillation with a period less than 10 s.

Long-period oscillations followed by short-period oscillations occur with high subcooling temperature in the case of 37.5 K and 40.0 K of subcooling temperature. The decreasing long-period oscillation mode was located in the high mass flux region between long-period oscillations and no oscillation regions. No oscillations were observed in both low mass flux and high mass flux region. Previous studies of oscillations in horizontal pipes (Çomaklı et al., 2002; Ding et al., 1995; Yüncü et al., 1991) have observed that density wave oscillations were superimposed on pres-

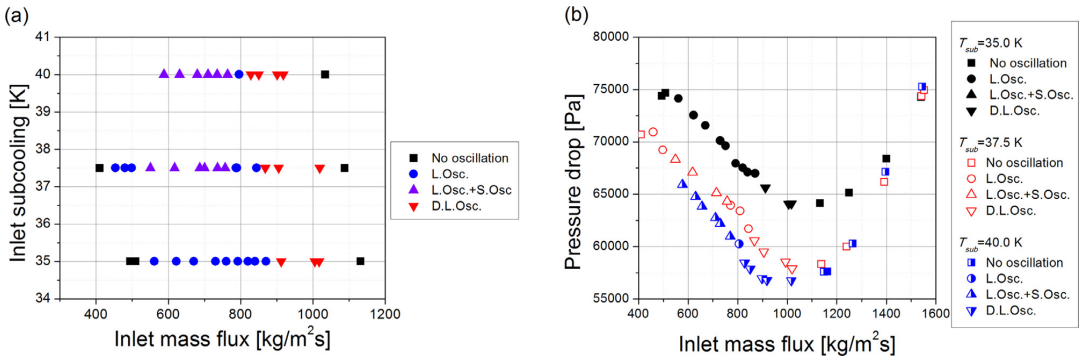

Fig. 5. Different instability modes depends on (a) subcooling temperature and (b) pressure drop (D. L. Osc.: decreasing long-period oscillation, L. Osc.: long-period oscillation, L. Osc. + S. Osc.: long-period oscillation followed by short-period oscillation).

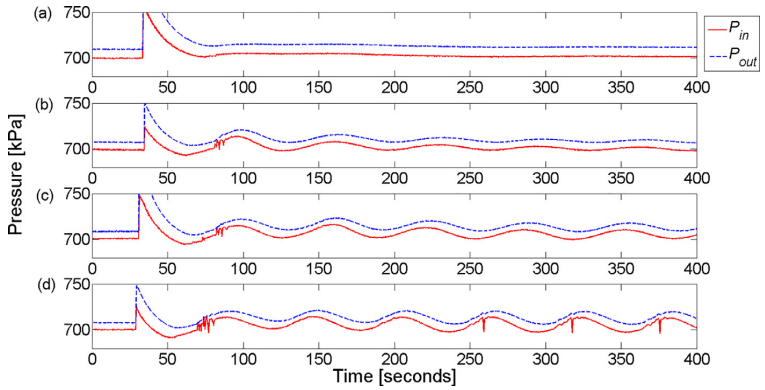

Fig. 6. Profile of the pressure of (a) no oscillation, (b) decreasing long-period oscillation, (c) long-period oscillation, and (d) long-period oscillation followed by short-period oscillation.

sure drop oscillations in horizontal pipes. However, no distinction between long-period oscillations and long-period oscillations with short-period oscillations was reported.

Fig. 5a shows the existence of the long-period oscillations and also an oscillation mode change between the long-period oscillations to long-period oscillations followed by short-period. This oscillation mode change was reported in an analytical study done by Yin et al. (2006) where the instabilities mode changes from DWO, to transition, to PDO with DWO, and to PDO with increasing mass flux and constant subcooling analytically. However, this analytical result has not been confirmed experimentally in horizontal conditions in previous studies. Fig. 5a confirms the suggested transitions derived by Yin et al. (2006).

Fig. 5b shows the different oscillation modes in the total pressure-mass flux map. The total pressure drop corresponds to the sum of the pressure drop in the test section and the main flow loop. No oscillation is observed when the slope of the N-shape curve becomes positive after the negative slope region. Yin et al. (2006) reported that the region for the superimposed DWO with PDO instability occurs when the system has high exit flow restriction which causes higher pressure drop and a steeper negative slope of the internal characteristic curve. However, in this study, it was observed that long-period oscillations followed by short-period oscillations occur in higher subcooling which causes lower pressure drop and a steeper negative slope of the internal characteristic curve. In particular, in the present work, it is observed that the negative slope apparently has no influence on the occurrence of long-period oscillations followed by short-period oscillations.

The profiles of the mass flux and the pressure are obtained for each oscillation mode as shown in Figs. 6 and 7. Initial mass fluxes for each case are (a) 1034, (b) 850, (c) 796, and (d) 710 kg/m^2 s and subcooling is 40.0 K. In Fig. 6, the pressure at the inlet (P_{in}, red solid line) and outlet (P_{out}, blue dash line) of the test section are depicted. In Fig. 7, the mass flux before the expansion tank (G_1, blue dash line) and between the expansion tank and test section (G_2, red solid line) are described. Figs. 6a and 7a represent the stable mode. In this case, there was no specific reaction after opening the valve for triggering the instability. Figs. 6b and 7b represent decreasing long-period oscillation mode. It was characterized by decreasing amplitude of oscillations with time. Figs. 6c and 7c show the long-period oscillations. In this mode, the pressure and mass flux oscillated continuously. Figs. 6d and 7d show the long-period oscillations followed by short-period oscillation mode. The short-period oscillations between the long-period oscillations were observed in both pressure and mass flux.

3.2. Limit cycles for the different oscillation modes

A parametric study on the internal characteristic curve which shows the variation of pressure as a function of mass flux for the steady states has been conducted by Manavela Chiapero et al. (2014). It has been reported that the negative slope is influenced by the level of subcooling. In particular, the negative slope be-

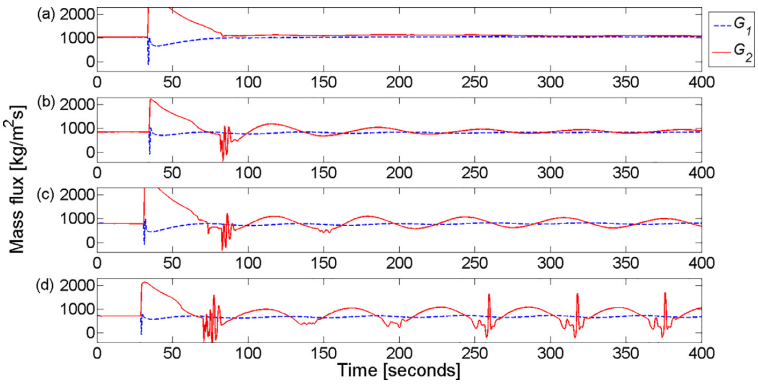

Fig. 7. Profile of the mass flux of (a) no oscillation, (b) decreasing long-period oscillation, (c) long-period oscillation, and (d) long-period oscillation followed by short-period oscillation. (For interpretation of the references to color in this figure, the reader is referred to the web version of this article.)

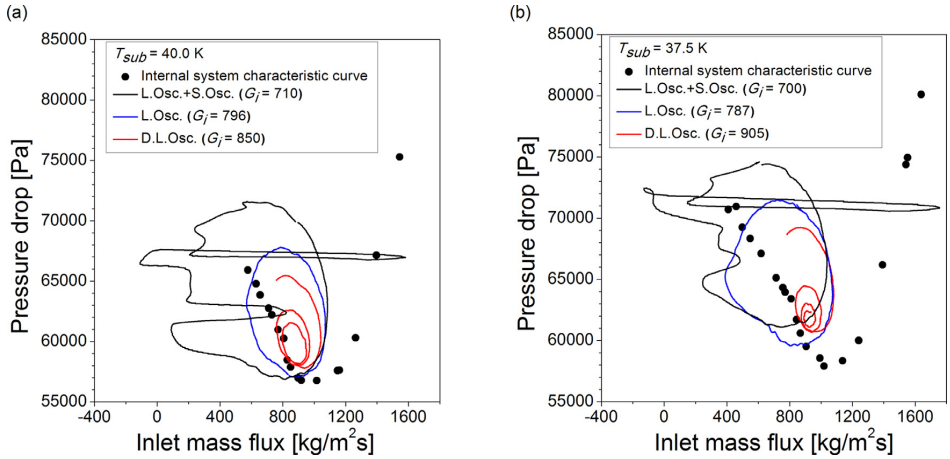

Fig. 8. The limit cycle for different oscillation modes for different subcooling (a) 40.0 K and (b) 37.5 K. (For interpretation of the references to color in this figure, the reader is referred to the web version of this article.)

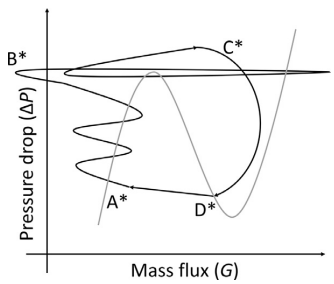

Fig. 9. Schematic diagram for the mechanism of interaction between long-period oscillations and short-period oscillations from experimental data in this study.

comes steeper as the subcooling is increased. In this study, the internal characteristic curve was obtained for three subcooling temperatures.

Mass flux and pressure under the oscillation can be plotted as a trajectory along time. The limit cycle can be presented as a closed line of the trajectory for mass flux and pressure. This limit cycle can represent the interaction between two parameters which are mass flux and pressure for this case in the dynamic system. It became possible to obtain the trajectory due to the development of the acquisition system. Limit cycles for the different oscillation modes are shown over the internal characteristic curve in Fig. 8. Initial mass flux (G_i) and subcooling temperature are described in each graph. Black circles are representing the internal characteristic curve from Fig. 5b. The synchronized data of pressure drop and inlet mass flux are depicted over the internal characteristic curve. It is possible to observe that there is a large fluctuation of the mass flux in the case of long-period oscillations with short-period oscillations. In the case of the long-period oscillations, the limit cycle presents a circular shape. It seems like that the flow excursion to liquid phase (B–C) and a flow excursion to gas phase (D–A) was not fully relaxed compared with the schematic diagram from the previous study in Fig. 1. It could be explained that it was because the compressible volume was not large enough and the thermal capacity was not small enough. This shrinkage of the limit cycle under PDO has been discussed by Manavela Chiapero et al. (2013), and attributed to the ratio of the thermal time constant and the residence time of a fluid particle. It has been reported that the thermal

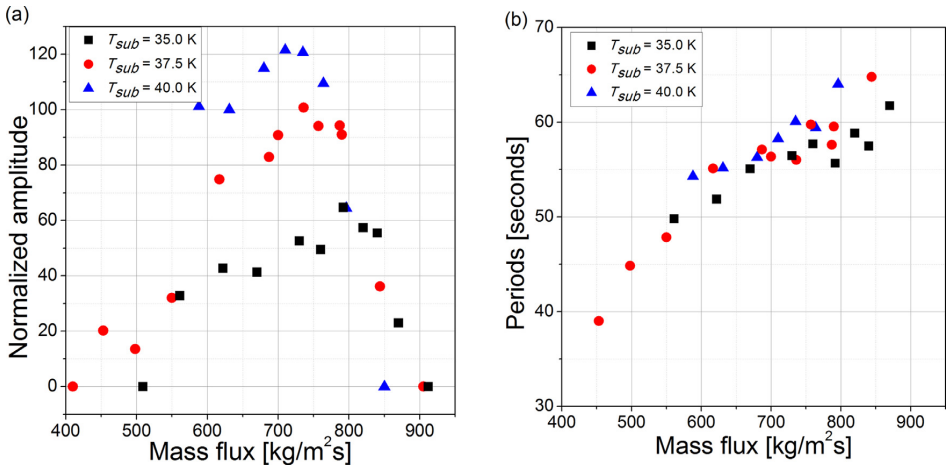

Fig. 10. Effect on the amplitude (a) and the period (b) of PDOs.

Table 2
Summary of effect on the amplitude and the period.

Parameter	Author	Yüncü et al. (1991)	Ding et al. (1995)	Çomaklı et al. (2002)	This study
Increasing mass flux	Effect on the amplitude	No effect	Increase	Increase	Increase/Decrease
	Effect on the period	Decrease/Increase	Increase	Increase	Increase
Increasing subcooling temperature	Effect on the amplitude	–	Increase	Increase	Increase/Decrease
	Effect on the period	–	Increase	Increase	Increase

capacity of the wall becomes dominant when the thermal time constant is relatively higher compared to the residence time of a fluid particle in the system. The shrinkage of the limit cycle was observed when the thermal characteristic time increases.

Fig. 9 shows the schematic diagram of the long-period oscillations with short period oscillations from Fig. 8. It is observed that the short-period oscillations occurred before the end of the flow excursion to the liquid phase (C*). Two types of short-period oscillations are occurring corresponding to the first short-period oscillations (A*–B*) and to the second short-period oscillations (B*–C*). An overshoot of pressure drop over the first inflection point of the internal characteristic curve is observed during the second short-period oscillations. It has not been considered for illustrating the mechanism of the PDO in the previous study by Liu and Kakaç (1991). It was shown that the flow excursion to the liquid phase was not fully relaxed (C*–D*). And it was observed that after the flow excursion from the two-phase to a liquid phase, the flow didn't reach the complete liquid phase due to the high heat flux condition. In summary, the limit cycle following the internal characteristic curve was observed in the phase of C*–D*–A*, the fluctuation of mass flux was observed in the phase of A*–B*, and an overshoot of the pressure drop was newly observed in the phase of B*–C*.

3.3. Effect of subcooling temperature and mass flux

In order to clarify the discrepancies on the effect on amplitude and period between the previous studies, both amplitude and period are measured for the test cases. The average of peak-to-peak amplitude per mean value of the mass flux is considered for the comparison. Only long period oscillations are considered and short period oscillations are not considered when calculating the amplitude of the oscillations. Decreasing long-period oscillations are considered as a zero amplitude of oscillation in order to clarify the effect on amplitude. The inlet pressure, the heat flux, the volume of liquid in the expansion tank, and the pressure in the expansion tank are kept constant in every case.

The effect of subcooling temperature and mass flux on amplitude and period is depicted in Fig. 10. In Fig. 10a, the *y*-axis represents the peak-to-peak amplitude of the mass flux normalized in terms of the average mass flux. In case of the mass flux, the amplitude of the oscillation increases with increasing mass flux until certain mass flux. After that, the amplitude of the oscillation decreases. In the case of subcooling temperature, it can be observed that the amplitude of oscillation increases as subcooling temperature increases. This can be explained by the shape of the internal characteristic curves. The pressure difference between the inflection points of the internal characteristic curve becomes higher when the subcooling is high. This pressure difference will affect the compression and decompression of the expansion tank during the PDO. The level of compression and decompression of the expansion tank will determine the level of the oscillation which can be presented by the amplitude. As depicted in Fig. 10b, the period of the PDOs increases with increasing mass flux and also subcooling temperature. The effect on the amplitude and period of the oscillations is summarized, including previous studies (Çomaklı et al., 2002; Ding et al., 1995; Yüncü et al., 1991) as described in Table 2.

4. Conclusion

In this work, the occurrence of long-period oscillations and long-period oscillations with superimposed short-period oscillations is experimentally studied in a horizontal heated tube. It has been observed that the long-period oscillation with superimposed short-period oscillation are apparently occurring in the intermedi-

ate part of the negative slope of the internal characteristic curve. The superimposed short-period oscillations disappear when the subcooling temperature is decreased. Moreover, it is observed that the negative slope of the internal characteristic curve apparently has no influence on the occurrence of the superimposed short-period oscillations. Pressure drop to mass flux limit cycles are also shown for illustrating the interaction of the oscillations.

Acknowledgments

The Ph.D. fellowship (Il-Woong Park) financed by the NTNU-SINTEF Gas Technology Centre is gratefully acknowledged.

References

Boure, J.A., Bergles, A.E., Tong, L.S., 1973. Review of two-phase flow instability. Nucl. Eng. Des. 25, 165–192.

Çomaklı, Ö., Karslı, S., Yılmaz, M., 2002. Experimental investigation of two phase flow instabilities in a horizontal in-tube boiling systems. Energy Convers. Manag. 43 (2), 249–268.

Del Valle, V.H., Kenning, D.B.R., 1985. Subcooled flow boiling at high heat flux. Int. J. Heat Mass Transf. 28, 1907–1920.

Ding, Y., Kakaç, S., Chen, X.J., 1995. Dynamic instabilities of boiling two-phase flow in a single horizontal channel. Exp. Therm Fluid Sci. 1777 (95), 327–342.

Doğan, T., Kakaç, S., Veziroğlu, T.N., 1983. Analysis of forced-convection boiling flow instabilities in a single-channel upflow system. Int. J. Heat Fluid Flow 4, 145–156. doi:10.1016/0142-727X(83)90060-7.

Durga Prasad, G.V., Pandey, M., Kalra, M.S., 2007. Review of research on flow instabilities in natural circulation boiling systems. Prog. Nucl. Energy 49, 429–451. doi:10.1016/j.pnucene.2007.06.002.

Guo, L.J., Feng, Z.P., Chen, X.J., Thomas, N.H., 1996. Experimental investigation of forced convective boiling flow instabilities in horizontal helically coiled tubes. J. Therm. Sci. 5, 210–216.

Kakac, S., Bon, B., 2008. A review of two-phase flow dynamic instabilities in tube boiling systems. Int. J. Heat Mass Transf. 51, 399–433. doi:10.1016/j.ijheatmasstransfer.2007.09.026.

Kandlikar, S.G., 2002. Two-phase flow patterns, pressure drop, and heat transfer during boiling in minichannel flow passages of compact evaporators. Heat Transf. Eng. 23 (1), 5–23.

Liang, N., Shao, S., Xu, H., Tian, C., 2010. Instability of refrigeration system – a review. Energy Convers. Manag. 51, 2169–2178. doi:10.1016/j.enconman.2010.03.010.

Liu, H.T., Kakac, S., 1991. An experimental investigation of thermally induced flow instabilities in a convective boiling upflow system. Heat Mass Transf. 26, 365–376. doi:10.1007/bf01591669.

Manavela Chiapero, E., Fernandino, M., Dorao, C.A., 2012. Review on pressure drop oscillations in boiling systems. Nucl. Eng. Des. 250, 436–447. doi:10.1016/j.nucengdes.2012.04.012.

Manavela Chiapero, E., Fernandino, M., Dorao, C.A., 2013. Numerical analysis of pressure drop oscillations in parallel channels. Int. J. Multiphase Flow 56, 15–24.

Manavela Chiapero, E., Doder, D., Fernandino, M., Dorao, C.A., 2014. Experimental parametric study of the pressure drop characteristic curve in a horizontal boiling channel. Exp. Therm Fluid Sci. 52, 318–327.

Mawasha, P.R., Gross, R.J., Quinn, D.D., 2001. Pressure-drop oscillations in a horizontal single boiling channel. Heat Transf. Eng. 22, 26–33. doi:10.1080/01457630152496296.

Menteş, A., Kakaç, S., Veziroğlu, T.N., Zhang, H.Y., 1989. Effect of inlet subcooling on two-phase flow oscillations in a vertical boiling channel. Wärme Stoffübertrag. 24, 25–36.

Ozawa, M., Nakanishi, S., Ishigai, S., Mizuta, Y., Tarui, H., 1979. Flow instabilities in boiling channels: Part 1. Pressure drop oscillations. Bull. JSME 22, 1113–1118.

Padki, M.M., Liu, H.T., Kakac, S., 1991. Two-phase flow pressure-drop type and thermal oscillations. Int. J. Heat Fluid Flow 12, 240–248. doi:10.1016/0142-727X(91)90058-4.

Padki, M.M., Palmer, K., Kakaç, S., Veziroğlu, T.N., 1992. Bifurcation analysis of pressure-drop oscillations and the Ledinegg instability. Int. J. Heat Mass Transf. 35, 525–532. doi:10.1016/0017-9310(92)90287-3.

Schlichting, W.R., Lahey, R.T., Podowski, M.Z., 2010. An analysis of interacting instability modes, in a phase change system. Nucl. Eng. Des. 240, 3178–3201. doi:10.1016/j.nucengdes.2010.05.057.

Stenning, A.H., Veziroglu, T.N., 1965. Flow Oscillation Modes in Forced-Convection Boiling. Heat Transfer and Fluid Mechanics Institute, University of Michigan, pp. 301–316 NASA Grant NsG-424.

Tadrist, L., 2007. Review on two-phase flow instabilities in narrow spaces. Int. J. Heat Fluid Flow 28, 54–62. doi:10.1016/j.ijheatfluidflow.2006.06.004.

Vandervort, C.L., Bergles, A.E., Jensen, M.K., 1994. An experimental study of critical heat flux in very high heat flux subcooled boiling. Int. J. Heat Mass Transf. 37, 161–173.

Yan, J., Bi, Q., Liu, Z., Zhu, G., Cai, L., 2015. Subcooled flow boiling heat transfer of water in a circular tube under high heat fluxes and high mass fluxes. Fusion Eng. Des. 100, 406–418. doi:10.1016/j.fusengdes.2015.07.007.

Yin, J., Lahey Jr., R.T., Podowski, M.Z., Jensen, M.K., 2006. An analysis of interacting instability. Multiph. Sci. Technol. 18, 359–385.

Yu, Z., Yuan, H., Chen, C., Yang, Z., Tan, S., 2016. Two-phase flow instabilities of forced circulation at low pressure in a rectangular mini-channel. Int. J. Heat Mass Transf. 98, 438–447. doi:10.1016/j.ijheatmasstransfer.2016.03.047.

Yüncü, H., Yildirim, O.T., Kakac, S., 1991. Two-phase flow instabilities in a horizontal single boiling channel. Appl. Sci. Res. 48, 83–104.

Zhang, T., Peles, Y., Wen, J.T., Tong, T., Chang, J.-Y., Prasher, R., Jensen, M.K., 2010. Analysis and active control of pressure-drop flow instabilities in boiling microchannel systems. Int. J. Heat Mass Transf. 53, 2347–2360. doi:10.1016/j.ijheatmasstransfer.2010.02.005.

Paper 2

On the occurrence of superimposed density wave oscillations on pressure drop oscillations and the influence of a compressible

Park, I. W., Fernandino, M., and Dorao, C. A.

AIP Advances, 8, 075022, 2018

On the occurrence of superimposed density wave oscillations on pressure drop oscillations and the influence of a compressible volume

Il Woong Park, Maria Fernandino, and Carlos A. Dorao[a]
Kolbjørn Hejes v1b, 7491 Trondheim, Norway

(Received 14 May 2018; accepted 16 July 2018; published online 25 July 2018)

Although two-phase flow instabilities are attributed to be one of the impediments for achieving high heat flux in boiling systems, most of their fundamental characteristics remain uncharted. In particular, pressure drop oscillations and density wave oscillations are two types of dynamic two-phase flow instabilities that can cause large variations in pressure and temperature. Under particular working conditions, both oscillations have been observed to interact, resulting in long-period pressure drop oscillations with superimposed short-period density wave oscillations. However, in this situation, the amplitude of the density wave oscillations is typically larger than the corresponding to a pure density wave oscillation. Here, we show that a compressible volume in the system, essential for the occurrence of pressure drop oscillations, plays a major role in amplifying the amplitude of the superimposed density wave oscillations. https://doi.org/10.1063/1.5040113

I. INTRODUCTION

Flow boiling is characterized by a complex interplay of hydrodynamic and thermal effects that can exhibit flow instabilities. These two-phase flow instabilities can result in transient and dynamic events that can induce mechanical and thermal fatigues, in addition, to deteriorate heat transfer in boiling systems.[1,2] In order to overcome the drawbacks of the flow instability, recent studies show the efforts for controlling and suppressing the oscillations.[3–5] Two typical types of dynamic two-phase flow oscillations are density wave oscillations and pressure drop oscillations which are characterized by short and large period oscillations respectively.[6–8] Since the 60s research has been carried out for unveiling the physics of the process and developing suitable models for predicting and controlling the occurrence of such instabilities.

Under particular working conditions, density wave and pressure drop oscillations can interact establishing a long-period oscillation with superimposed short-period oscillations at the minimum of the long-period oscillations. However, the corresponding superimposed density wave oscillation shows a larger amplitude compared with the pure density wave oscillation. For example, in previous studies, it is possible to observe that the amplitude of the superimposed density wave oscillation has been amplified about five to ten times.[9–11]

Only a few studies have been focused on understanding the interplay of density wave and pressure drop oscillations. Briefly, a typical boiling system where two-phase flow oscillations may occur consists in a heated section, inlet and outlet valves (or orifice plates) is characterized by a compressible volume due to the presence of vapor in the system. This compressible volume is typically represented in experimental studies with a surge tank connected upstream of the test section. Liu and Kakaç (1991)[12] suggested that superimposed density wave oscillations could occur due to complete boiling during the pressure increase stage in the pressure drop oscillation limit cycle. Menteş et al.

[a]Author to whom correspondence should be addressed. Electronic mail: carlos.dorao@ntnu.no

(1989) explained that the superimposed density wave oscillations could be triggered by a sudden change in the mass flow rate due to bubbles crossing the orifice in the inlet valve.[13] Moreover, in this case, the sudden change of the pressure is accompanied by a change in the mass flux. Using linear frequency domain stability models, Yin et al. (2006) showed that pressure drop oscillations occur due to the compressible volume at the heater inlet, while density wave oscillations are not affected by the latter.[14] In summary, in the previous studies, the superimposed oscillations have been attributed either to the complete boiling during pressure drop oscillations,[12] or sudden change of the mass flux in the orifice valve during the pressure drop oscillations[13] or the interaction of the oscillations.[14] In this letter, we show that the compressible volume in the surge tank upstream of the test section plays a major role in controlling the amplitude of the superimposed density wave oscillations.

II. EXPERIMENTAL SECTION

To investigate the interplay of density wave and pressure drop oscillations an experimental facility was constructed consisting of a horizontal test section of 5mm ID stainless steel pipe heated with Joule effect using R134a as working fluid, Figure 1. A surge tank was located just upstream of the test section to control the available compressible volume in the system. Details of the experimental facility, experimental procedures, calibration tests and uncertainty analysis are presented in the supplementary material.

III. RESULTS AND DISCUSSIONS

Figure 2(a) and 2(c) show a reference case for the superimposed density wave oscillations during pressure drop oscillations. The selected conditions of the experiment were a mass flux of 700 kg/m^{2}s, subcooling of 37.5 K, the inlet pressure of 7.0 kPa and 0.0043 m^3 of compressible volume in the surge tank. For this experiment, the valve connected to the surge tank was opened for triggering the pressure drop oscillations. In this case, it is possible to observe short-period, high-amplitude density wave oscillations superimposed on the long-period pressure drop oscillations. In order to exclude the effect of the compressible volume on the pressure drop oscillations, the approach consisted in mimicking the mass flux oscillations observed during the pressure drop oscillations by controlling the pump while maintaining the surge tank closed. Figure 2(b) and 2(d) show the profile of the mass flux

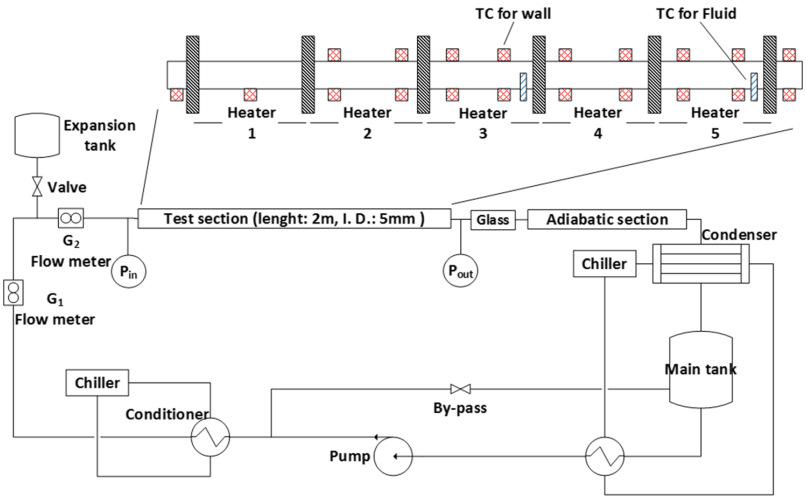

FIG. 1. Sketch of the experimental facility and test section.

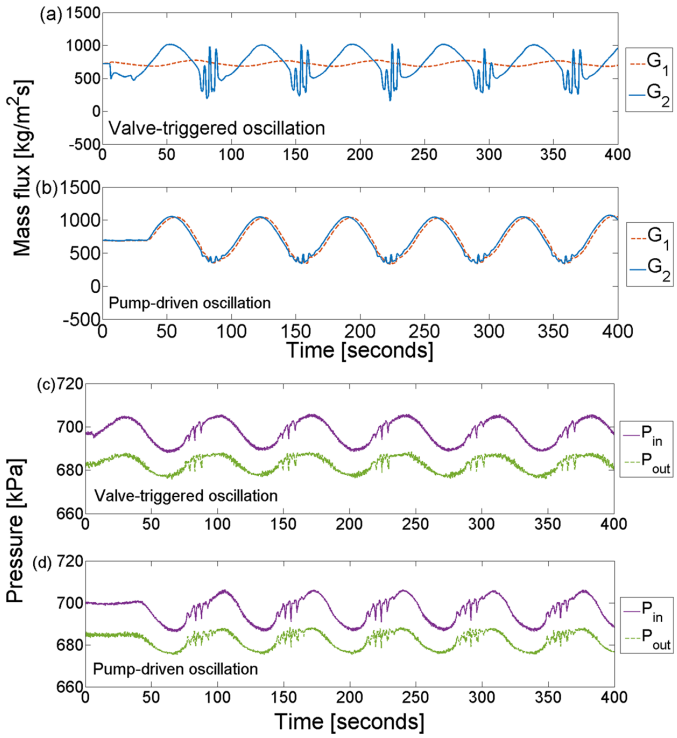

FIG. 2. Mass flow rate and pressure of valve-triggered oscillation (a, c) and pump-driven oscillation (b, d).

and the pressure under the pump-driven oscillatory condition. Comparing these two cases, i.e. the pressure drop oscillations with superimposed density wave oscillations and the mimicked pressure drop oscillations by controlling the flow with the pump, the amplitude of the mass flux oscillation during the density wave oscillations was significantly suppressed. However, it is possible to see short-period superimposed oscillations in the evolution of the pressure. This shows that the occurrence of the superimposed density wave oscillations during pressure drop oscillations does not depend on the presence of a compressible volume.

The previous experiments suggest that the compressible volume controls the amplitude of the density wave oscillations, amplifying it. In order to confirm this, the following experiment was performed. For a particular initial condition of 300 kg/m^{2}s of mass flux, 0.0043 m^3 of compressible volume and 30.0 K of subcooling (where pressure drop oscillation cannot occur even if the valve for the expansion tank is opened) the influence of the compressible volume on the pure density wave oscillations is studied. The valve for the compressible volume was opened (at 50 and 250 seconds) and closed (at 150 seconds and 350 seconds) as shown in Figure 3(a) and 3(d). The profiles of the mass flux and pressure evolution are depicted in Figure 3(b) and 3(e) for the closed valve and in Figure 3(c) and 3(f) for the opened valve. With the compressible volume not connected, density wave oscillations do not fully develop and only small amplitudes (~20 kg/m^{2}s) are observed. However, with the compressible volume connected, density wave oscillations develop fast reaching large amplitudes (~700 kg/m^{2}s). This experiment confirms the role of the compressible volume not only for the occurrence of pressure drop oscillations but also in the amplification of the density wave oscillations. In particular, this experiment shows that the occurrence of large-amplitude density wave oscillations superimposed on pressure drop oscillations is a consequence of the presence of the compressible volume.

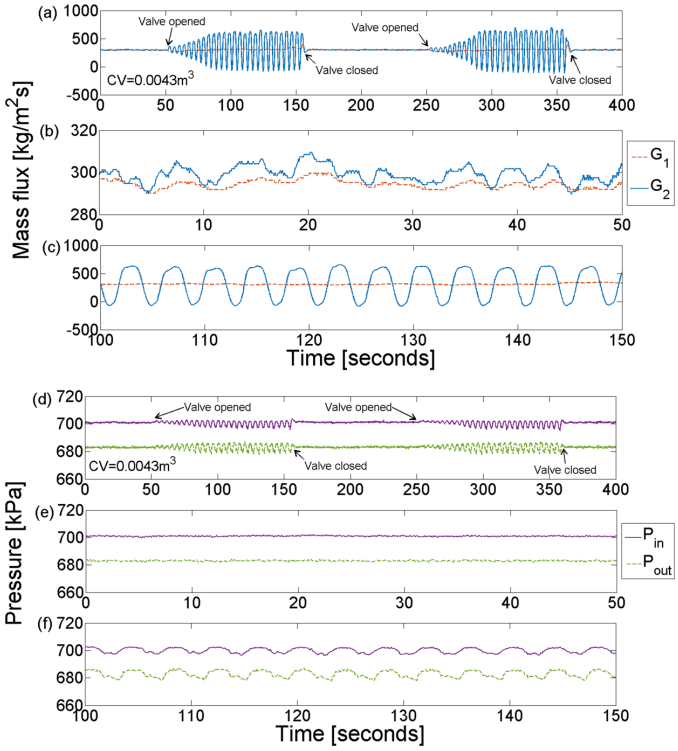

FIG. 3. Effect of the existence of the compressible volume on mass flux (a-c) and pressure (d-f) during density wave oscillations. The valve for the compressible volume was opened at 50 and 250 seconds and it was closed at 150 and 350 seconds.

In the next part of this study, the influence of the compressible volume on the magnitude of the amplitude of pure density wave oscillations is studied. Compressible volumes of 0.0013 m^3 and 0.0094 m^3 are tested as shown in Figure 4. It is observed that the compressible volume is essential

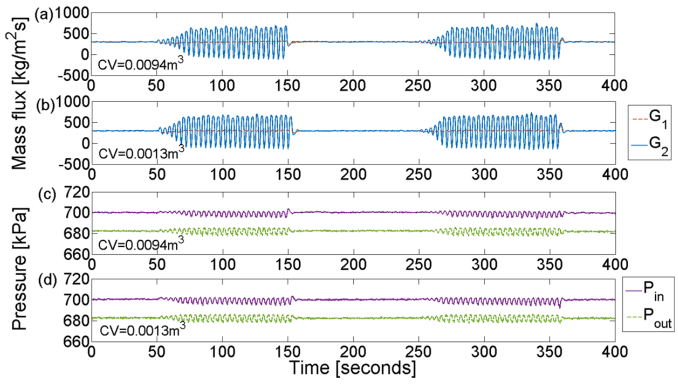

FIG. 4. Mass flux and pressure during amplified density wave oscillations with 0.0094 m^3 (a, c) and 0.0013 m^3 (b, d) of compressible volume. The valve for the compressible volume was opened at 50 and 250 seconds and it was closed at 150 and 350 seconds.

for the large amplitude of the density wave, but it is not possible to observe a dependency of the amplitude of the density wave on the value of the compressible volume for the studied cases.

Now, under pressure drop oscillations condition, the influence of the magnitude of the compressible volume on the amplitude of the density wave oscillations is studied by setting the compressible volume at 0.0013 m^3, 0.0043 m^3 (corresponds to the reference case in Figure 2(a)) and 0.0094 m^3, with a mass flux of 700 kg/m^2s and 37.5 K of subcooling as the initial conditions. As shown in Figure 5, the magnitude of the compressible volume influences the characteristics of both the pressure drop and superimposed density wave oscillations. In the case of the large compressible volume (Figure 5(a) and (b)), a larger amplitude of mass flux oscillations and the longer period of pressure drop oscillations were observed as compared to the low compressible volume case. Moreover, the amplitude of the superimposed density wave oscillations is more enhanced when the compressible volume is large. On the other hand, superimposed density wave oscillations disappeared in the case of small compressible volume, as shown in Figure 5(c) and (d). According to the findings above, it seems like the rate of change of the mass flux was not large enough to be considered as a sudden perturbation for triggering density wave oscillations. The small amplitude of the pressure drop oscillations was a consequence of the level of the compressible volume. This shows that the operating conditions could change the profile of the pressure drop oscillations while the occurrence of the superimposed density wave oscillations is controlled by the rate of change of the mass flux during pressure drop oscillations.

Superimposed density wave oscillations can be triggered by the sudden perturbation of the pressure drop which causes the perturbation of the flow rate. In the last part of this study, it is studied whether the pressure drop oscillations can be considered as a sudden perturbation of the mass flux for

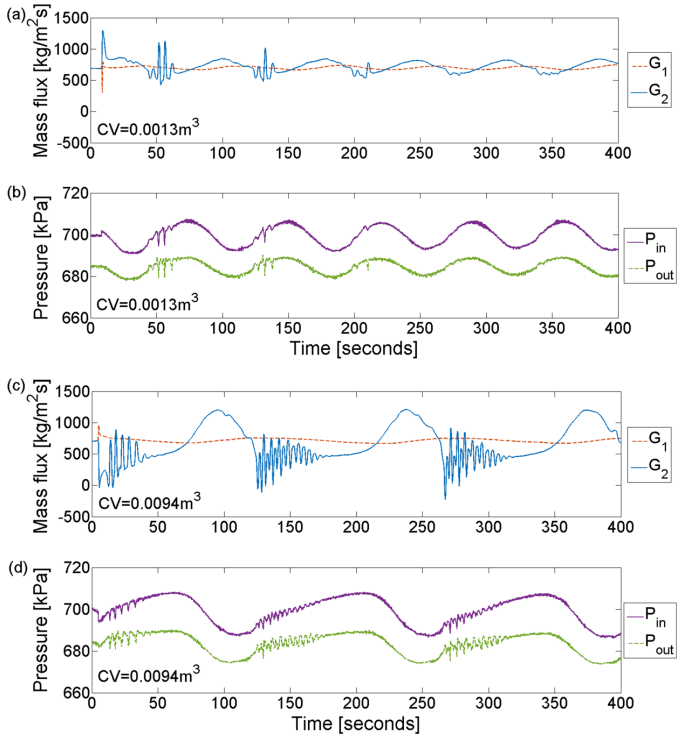

FIG. 5. Mass flux and pressure during pressure drop oscillations with 0.0094 m^3 (a, b) and 0.0013 m^3 (c, d) of compressible volume.

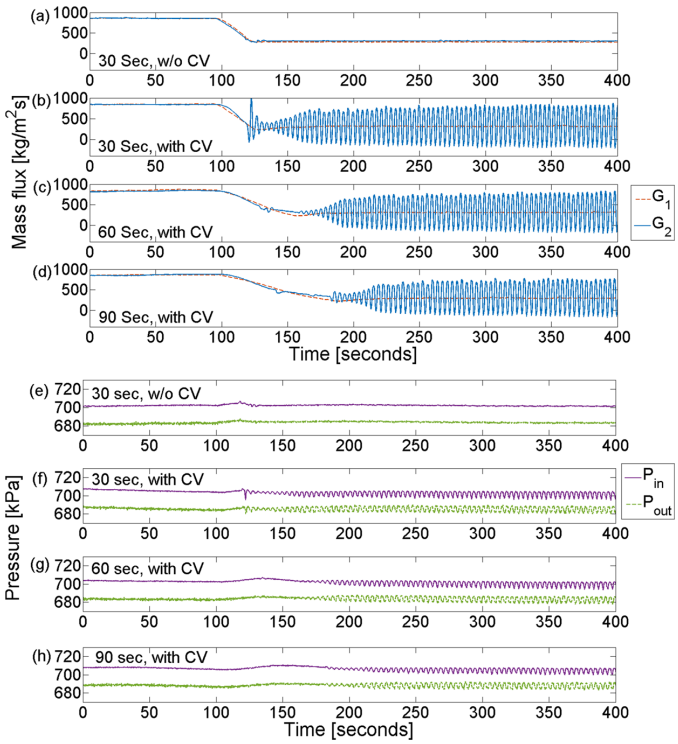

FIG. 6. Occurrence of density wave oscillations by reducing the mass flux without compressible volume during 30 seconds (a, e), with compressible volume during 30 seconds (b, f), 60 seconds (c, g), and 90 seconds (d, h).

triggering density wave oscillations. It is assumed that the superimposed density wave oscillations could instantly develop when the rate of change in the mass flux is fast enough. The experiment consists in suppressing the oscillatory condition of the pressure drop oscillations and mimicking the decreasing profile of the mass flux under the pressure drop oscillations by controlling the mass flux with the pump. As initial conditions, 850 kg/m^{2}s of mass flux, 30.0 K of subcooling and 7.0 kPa of inlet pressure were selected. The mass flux was varied decreasingly from 850 to 300 kg/m^{2}s as shown in Figure 6. The same variation of mass flux was performed in a time interval of 30 seconds (Figure 6(a) and 6(b)), 60 seconds (Figure 3(c)) and 90 seconds (Figure 6(d)). The corresponding profiles of the pressure are also depicted in Figure 6(e), 6(f), 6(g) and 6(h). The valve between the compressible volume and the test section was closed in the case of Figure 6(a) while the valve was opened in the case of Figure 6(b–d). As shown in Figure 6(a), small perturbations of the mass flux were observed in this case. However, density wave oscillations did not develop under these conditions (i.e. no compressible volume) even though the mass flux was varied fast. As observed in Figure 6(b), density wave oscillations can develop instantly during the mass flux decreasing. In the other cases (Figure 6(c) and 6(d)), density wave oscillations were gradually developed after the decrease in mass flux is finished. Interestingly, the large-amplitude peak observed just after the sudden drop of the mass flux in Figure 6(b) is similar to the large-amplitude oscillations observed during the superimposed density wave oscillations in Figure 2(a) and 5(a). This could imply that a fast change in the mass flux during a pressure drop oscillation can be considered as a sudden perturbation and is an essential condition for the occurrence of the superimposed density wave oscillations.

The objectives and findings for each experiment are summarized in order to present overall picture clearly as shown in table I.

TABLE I. List of the objective of the experiments and finding from each experiment.

Figure	The objective of the experiments	Finding from the experiments
2	Mimicking of the valve-triggered (self-induced) oscillations by controlling the pump	Mass flux of superimposed density wave oscillations amplified for valve-triggered cased.
3	Decoupling of the effect of the existence of the compressible volume from the pressure drop oscillations	Amplitude of the density wave oscillation is amplified because of the existence of the compressible volume.
4	Identifying the effect of the level of the compressible volume on the pure density wave oscillations	There is no dependency of the amplitude of the pure density wave oscillations.
5	Identifying the effect of the level of the compressible volume on the superimposed density wave oscillations	Level of the compressible volume affect the characteristics of superimposed density wave oscillations and pressure drop oscillations.
6	Decoupling the effect of the transition of the mass flux from the oscillatory flow	Essential condition for the superimposed density wave oscillations is the fast change in the mass flux.

It can be noticed that an effective method has not been developed for the complete elimination of the two-phase flow oscillations.[15] Thus, investigation on two-phase flow instability is still necessary. It is shown for the first time that density wave oscillations over imposed on pressure drop oscillations are having a larger amplitude compared to pure density wave oscillations as a consequence of the expansion tank. Besides, it is shown for the first time that the rate of change of the flow plays a major role in triggering the density wave oscillations. These two findings can provide a new insight into the physics of two-phase flow instabilities.

IV. CONCLUSION

In summary, in this study superimposed density wave and pressure drop oscillations were decoupled with an experimental technique for identifying the characteristics of the oscillations. It was found that density wave oscillations can be superimposed on pressure drop oscillations when the large-period oscillations corresponding to the pressure drop oscillations imposes a fast rate of change in the mass flux. The amplitude of the mass flux oscillations during density wave oscillations can be amplified due to the existence of the compressible volume which is the essential condition for pressure drop oscillations. The level of the compressible volume can affect the characteristics of the pressure drop oscillations, while the latter can, in turn, trigger the density wave oscillations when accompanied by a fast change in mass flux.

SUPPLEMENTARY MATERIAL

See supplementary material for the details of the experimental setup and procedure.

ACKNOWLEDGMENTS

The authors gratefully acknowledge the NTNU-SINTEF Gas Technology Centre for the Ph.D. fellowship (Il-Woong Park).

[1] S. G. Kandlikar, J. Heat Transfer **134**, 3 (2012).
[2] T. Zhang, Y. Peles, J. T. Wen, T. Tong, J. Y. Chang, R. Prasher, and M. K. Jensen, Heat Mass Transfer **53**, 2347 (2010).
[3] Y. Zhu, D. S. Antao, D. W. Bian, S. R. Rao, J. D. Sircar, T. Zhang, and E. N. Wang, Appl. Phys. Lett. **110**, 033501 (2017).
[4] A. K. Vutha, S. R. Rao, F. Houshmand, and F. Y. Peles, Appl. Phys. Lett. **108**, 134104 (2016).
[5] W. Li, X. Qu, T. Alam, F. Yang, W. Chang, J. Khan, and C. Li, Appl. Phys. Lett. **110**, 014104 (2017).
[6] J. A. Boure, A. E. Bergles, and L. S. Tong, Nucl. Eng. Des. **25**, 165 (1973).
[7] S. Kakaç and B. Bon, Int. J. Heat Mass Transfer **51**, 399 (2008).
[8] E. M. Chiapero, M. Fernandino, and C. A. Dorao, Nucl. Eng. Des. **250**, 436 (2012).
[9] C. A. Dorao, Chem. Eng. Sci. **134**, 767 (2015).
[10] Y. Ding, S. Kakaç, and X. J. Chen, Exp. Therm. Fluid Sci. **11**, 327 (1995).

[11] I. W. Park, M. Fernandino, and C. A. Dorao, Effect of the Mass Flow Rate and the Subcooling Temperature on Pressure Drop Oscillations in a Horizontal Pipe, 24th international conference nuclear energy for new Europe, Slovenia, Portoroz, 14–17 September.
[12] H. T. Liu and S. Kakaç, Heat Mass Transfer **26**, 365 (1991).
[13] A. Menteş, S. Kakaç, T. N. Veziroğlu, and H. Y. Zhang, Wärme-und Stoffübertragung **24**, 25 (1989).
[14] J. Yin, R. T. Lahey, Jr., M. Z. Podowsk, and M. K. Jensen, Multiph. Sci. Technol. **18**, 359 (2006).
[15] N. Liang, S. Shao, H. Xu, and C. Tian, "Instability of refrigeration system–A review," Energy Convers. Manag. **51**, 2169 (2010).

3.2 Deterioration of heat transfer due to flow oscillations (Papers 3 and 4)

Even though research has been performed for identifying the characteristics of the pressure drop oscillation, how the pressure drop affects the heat transfer coefficient remains unclear. It is important to evaluate how the heat transfer coefficient can be affected by pressure drop oscillation because severe deteriorations have been observed in the literature [16]. In **Paper 3**, the heat transfer coefficient during pressure drop oscillation conditions was investigated. Contrary to previous findings in the literature, a significant deterioration of the heat transfer coefficient was not observed for the conditions tested.

Based on these contradictory observations, further investigation of the heat transfer coefficient under oscillatory conditions was required. In order to be able to determine whether flow oscillations can actually affect the heat transfer coefficient under certain circumstances, it is necessary to have a proper control of the amplitude and frequency of the oscillations. In the case of self-sustained oscillations, such as density wave and pressure drop oscillations, such control is not feasible since the characteristics of the oscillations depend on the system configuration. In **Paper 4**, it is assumed that the deterioration of the heat transfer is closely related to the amplitude and period of the flow oscillations. To prove this hypothesis, flow oscillations are generated by controlling the pump to force a sinusoidal profile. The results confirmed that flow oscillations can deteriorate the heat transfer coefficient. Moreover, it was observed that the deterioration depends on the period and amplitude of the oscillations. Furthermore, the occurrence of dry-out is considered as the main contributor to the deterioration of the heat transfer coefficient.

Paper 3

Effect of the Pressure Drop Oscillation on the Local Heat Transfer Coefficient in a Heated Horizontal Pipe

Park, I. W., Fernandino, M., and Dorao, C. A.

In ASME 2018 16th International Conference on Nanochannels, Microchannels, and Minichannels

American Society of Mechanical Engineers.

Paper 4

Can flow oscillations during flow boiling deteriorate the heat transfer coefficient?

Park, I. W., Ryu, J. R., Fernandino, M., and Dorao, C. A.

Can flow oscillations during flow boiling deteriorate the heat transfer coefficient?

I-W Park,[1] J. Ryu,[1] M. Fernandino,[1] and C.A. Dorao[1, a)]
Department of Energy and Process Engineering
Norwegian University of Science and Technology
Trondheim, Norway.

(Dated: 24 June 2018)

Two-phase flow instabilities have been attributed to be one of the impediments for achieving high heat flux in boiling systems due to its potential heat transfer deterioration. However most of the fundamental characteristics of the two-phase flow instabilities and the mechanisms leading to the heat transfer deterioration remain uncharted. In particular up to what extend the self-induced oscillations can deteriorate the heat transfer coefficient is not well understood. Here we measure flow boiling heat transfer coefficient under controlled oscillatory flow conditions. We show that flow oscillations can deteriorate the heat transfer coefficient significantly, but the deterioration depends on the amplitude and period of the oscillations. In particular the deterioration is primarily a consequence of dry-out at the wall that increases the averaged wall temperature.

PACS numbers: 44, 47
Keywords: Two-phase flow boiling; Two-phase flow instabilities; Heat transfer coefficient

Flow boiling inside tubes is characterised by a complex interplay of hydrodynamic and thermal effects where the dominant mechanisms controlling heat transfer remains not understood[1]. Under particular conditions two-phase flow instabilities can be observed. These transient and dynamic events can induce mechanical and thermal fatigues. Two typical two-phase flow instabilities are pressure drop oscillations (PDO) and density wave oscillations (DWO). The former is characterised by long period oscillations while the later by short period oscillations. In addition the amplitude of the oscillations is strongly dependent on the characteristics of the external system, i.e. the mass flux-pressure drop response of the device driving the flow in the system. Although two-phase flow instabilities have been attributed to be one of the impediments for achieving high heat flux in boiling systems, most of its fundamental characteristics remains uncharted. A large number of studies have investigated alternatives for controlling and suppressing the oscillations for overcoming the drawbacks attributed to the two-phase flow instabilities[2–4]. However up to what extend the oscillations can deteriorate the heat transfer coefficient is not understood as only few studies has focused on the deterioration of the heat transfer coefficient during two-phase flow instabilities[5,6]. In particular, it has been reported that in experiments with controlled flow oscillations the critical heat flux is a decreasing function of the amplitude and period of the flow oscillation, and reaches almost 40% of the steady state value[7]. In the case of pressure drop oscillations, it has been observed that the flow oscillations deteriorates the heat transfer coefficient in the case of helical tubes compared to the stable condition[5]. On the other hand, controlled flow rate oscillations in the form of a triangular wave with an amplitude lower than 30 % of the mean mass flux are not showing a noticeable influence on the heat transfer coefficient[8]. A major challenge when studying the influence of two-phase flow instabilities on the heat transfer coefficient is that the period and amplitude of the oscillations depend on the external system and the characteristics of the test section. For this reason, here we measure the heat transfer coefficient of controlled sinusoidal flow oscillations. In this letter, we show that flow oscillations can deteriorate the heat transfer coefficient, but the deterioration is strongly dependent on the amplitude and period of the oscillation.

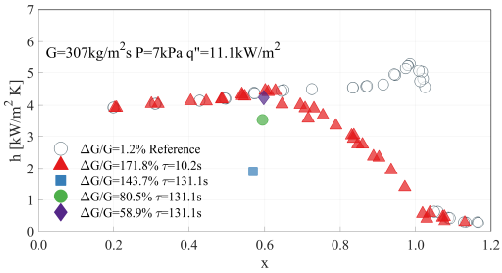

FIG. 1: Deterioration of the heat transfer coefficient during controlled flow oscillations in an horizontal heated pipe of 5mm ID with refrigerant R134a.

To investigate the deterioration of the heat transfer coefficient under oscillatory flows a test section consisting of a 5 mm ID stainless steel pipe heated with Joule effect is used. The facility is equipped with a conditioning section to heat up the working fluid (R134a) to the desired local thermodynamic quality where the heat transfer coefficient is determined by 4 thermocouples installed at the outer wall of the pipe and one inner thermocouple for determining the fluid temperature. The oscillation

a)Electronic mail: carlos.dorao@ntnu.no.

of the flow was done by controlling the pump speed in a sinusoidal profile. Details of the experimental facility, experimental procedures, calibration tests, and uncertainty analysis are presented in the supplementary material. In the case of oscillatory flows, the dynamic response of the tube wall temperature can be affected by the wall heat capacity. Therefore the measured temperature at the outer wall can suffer from damping and phase lag. The thermal penetration depth can be estimated by

$$\delta = \sqrt{\frac{2\alpha_w}{\omega}} \tag{1}$$

where α_w represents the thermal diffusivity of the tube material and ω the angular frequency. The thermal penetration is 11mm for oscillations with a period τ of 1s and the penetration depth increases with the oscillation period. The present experiments are able to capture the variation of the inner wall temperature as the wall-thickness of the test section is 1.5mm. Considering a lumped-capacitance approximation of the response of the tube wall, the thermal time constant of the wall is defined as

$$\tau_t = \frac{\rho_w Cp_w (D_o^2 - D_i^2)}{h4D_i} \tag{2}$$

where Cp_w is the thermal capacity, ρ density, D_o external diameter, D_i internal diameter and h the heat transfer coefficient from the wall to the fluid. This gives an estimation of $\tau_t \approx 15s$ for the heat transfer coefficient corresponding to post-dryout conditions, while $\tau_t \approx 2s$ for an averaged heat transfer coefficient in the two-phase flow region.

In order to determine wether flow oscillations can deteriorate heat transfer compared to the stable condition, the temporal averaged heat transfer, h, is computed, where

$$h = \frac{1}{T}\int_0^T \frac{q"}{T_{wall} - T_{fluid}} dt \tag{3}$$

with T_{wall} and T_{fluid} the the internal wall temperature and fluid temperature respectively and $q"$ the heat flux. In particular T_{fluid} is assumed to be the saturation temperature at the working pressure, i.e. $T_{sat}(P)$. However, it will be shown that this assumption is not appropiate in the case of large amplitude oscillations. The averaged heat transfer coefficient is based on at least 10 cycles in the case of the oscillatory flow.

Fig. 1 shows measurement during stable and oscillatory conditions of the averaged heat transfer coefficient in functions of the averaged thermodynamic quality. The amplitude of the oscillations are characterised in terms of normalised oscillation amplitude defined as the peak-to-peak amplitude divided by the mean mass flux, i.e. $\Delta G/G$, and the period of the oscillation τ. These values are computed using Fast Fourier Transform. These experiments show the complexity of assessing wether flow oscillations deteriorates the heat transfer coefficient as it depends on the local averaged quality, amplitude and period of the oscillation for a given working condition. In particular, the quality at the inception of the heat transfer deterioration, x_i, depends on the amplitude and the period of the oscillation. It is noted that for qualities above x_i, the deterioration of the heat transfer coefficient increases monotonously as the thermodynamic quality increases, while for qualities below x_i no effect of the oscillation is observed. The dependency of the heat transfer deterioration on the averaged local quality implies a dependency on the local liquid mass fraction. Increasing the averaged qualities, the amplitude of the oscillation for reaching a periodic dryout of the pipe wall reduces.

In Fig. 2, the time evolution of the wall and fluid temperatures, instantaneous heat transfer coefficient and mass flux are despicted. It is possible to identify four stages in the case of large flow oscillations, Fig. 2 (c). In the first stage, when the mass flux goes to the minimum of the oscillation a sudden increases of both wall and fluid temperatures are observed. The heat transfer coefficient based on the saturation temperature decreases due to the increase of the wall temperature. In a second stage, as the mass flux increases from the minimum value the fluid temperature start to decrease while the wall temperature increase further due to the wall inertia. In particular only a few studies have discussed the influence of the wall inertia during flow instabilities[9]. In the third stage, the wall temperature starts to decrease when the fluid temperature becomes close to the saturation temperature. This could be attributed to the rewetting of the surface. In the last step, the temperature of the wall and fluid remain constant. In the case of relative small amplitude flow oscillations Fig. 2 (a), the heat transfer coefficient is not affected by the flow oscillation.

Fig. 3 shows the time-averaged local heat transfer coefficient under oscillatory flow condition as a function of the oscillation amplitude for selected oscillations periods at a local averaged quality of 0.6. As it has been shown that the fluid temperature departs from the saturation temperature at large oscillations amplitudes, in this case the heat transfer coefficient is approximated as

$$h = \frac{q"}{T_{wall} - T_{fluid}} \tag{4}$$

with T_{wall}, T_{fluid} and $q"$ averaged values, where in particular T_{fluid} is the measured fluid temperature. This approximation of the heat transfer coefficient is considered as large oscillations amplitudes will be studied. It is noticed that flow oscillation deteriorates the heat transfer coefficient for normalised amplitudes above 70% and the deterioration is more pronounced as the period of the oscillation increases. This result agrees with previous experiments showing that for controlled flow rate oscillations in the form of a triangular wave with an amplitude lower than 30 % of the mean mass flux no noticeable influence on the heat transfer coefficient was observed[8,10].

The results also indicate that the heat transfer deteri-

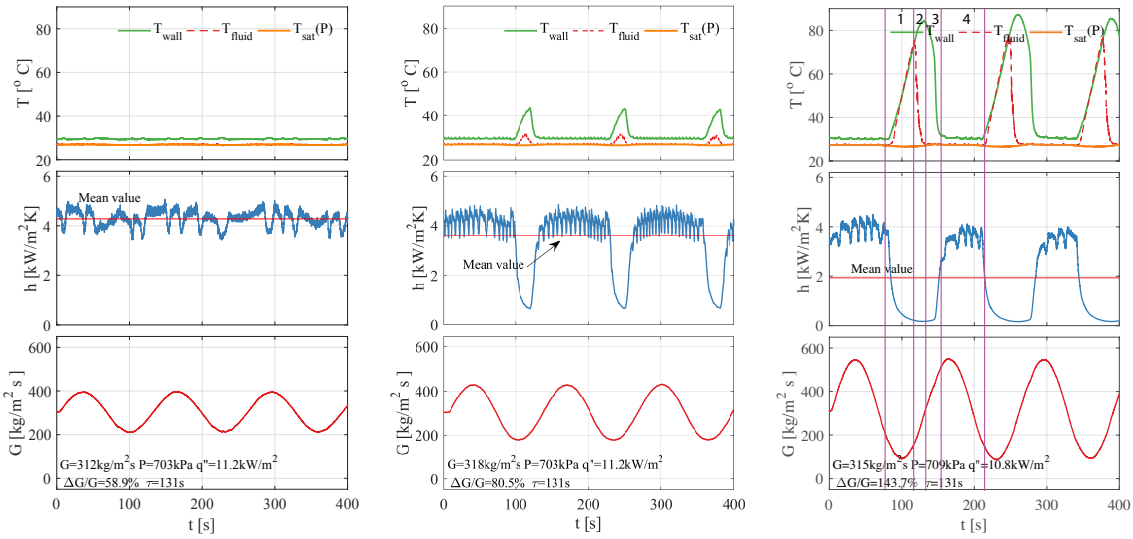

(a) (b) (c)

FIG. 2: Effect of the flow oscillation on the wall temperature and local heat transfer when increasing the amplitude of the oscillation for a given period of the oscillation.

oration is triggered when the mass flux is lower than 200 kg/m^{2}s at an averaged quality of 0.6, see Fig. 2 (b). Assuming that the heat transfer follows a power law above the inception of heat transfer deterioration, it is possible to write

$$h \propto \left(\Delta G/G\right)^{-\beta} \tag{5}$$

where β depends on the period of the oscillation. Fig. 3 (b) shows that β increases monotonously by increasing the period τ and above 100s, approaches a maximum. The previous results indicates that i) there is a threshold of the oscillation amplitude for observing heat transfer deterioration, ii) the heat transfer deterioration increase with the period of the oscillation until reach a maximum.

In summary, the deterioration of the heat transfer coefficient during flow boiling in the case of controlled flow oscillations is shown experimentally. It is observed that flow oscillations can deteriorate the average heat transfer coefficient, but the deterioration depends on the amplitude and period of the oscillation. In particular the deterioration is not noticeable until the amplitude of the oscillations reaches a given threshold. The deterioration of the heat transfer coefficient during flow oscillation is attributed to the dry-out of the wall during the low mass flux part of the oscillation. Therefore, self-induced oscillations occurring during two-phase flow instabilities can be detrimental to the heat transfer coefficient but only if the amplitude of the oscillations are above a given value. This result indicates the presence of two-phase oscillations is not directly implying a deterioration of the heat transfer performance.

SUPPLEMENTARY MATERIAL

See supplementary material for details of the heat transfer experiments and experimental data base.

ACKNOWLEDGMENTS

The authors gratefully acknowledge the NTNU-SINTEF Gas Technology Centre for the Ph.D. fellowship (Il-Woong Park).

[1] C. Dorao, S. Drewes, and M. Fernandino, "Can the heat transfer coefficients for single-phase flow and for convective flow boiling be equivalent?" Applied Physics Letters **112**, 064101 (2018).

[2] Y. Zhu, D. S. Antao, D. W. Bian, S. R. Rao, J. D. Sircar, T. Zhang, and E. N. Wang, "Suppressing high-frequency temperature oscillations in microchannels with surface structures," Applied Physics Letters **110** (2017), 10.1063/1.4974048.

[3] A. K. Vutha, S. R. Rao, F. Houshmand, and Y. Peles, "Active control of flow boiling oscillation amplitude and frequency using a transverse jet in crossflow," Applied Physics Letters **108** (2016), 10.1063/1.4945334.

[4] W. Li, X. Qu, T. Alam, F. Yang, W. Chang, J. Khan, and C. Li, "Enhanced flow boiling in microchannels through integrat-

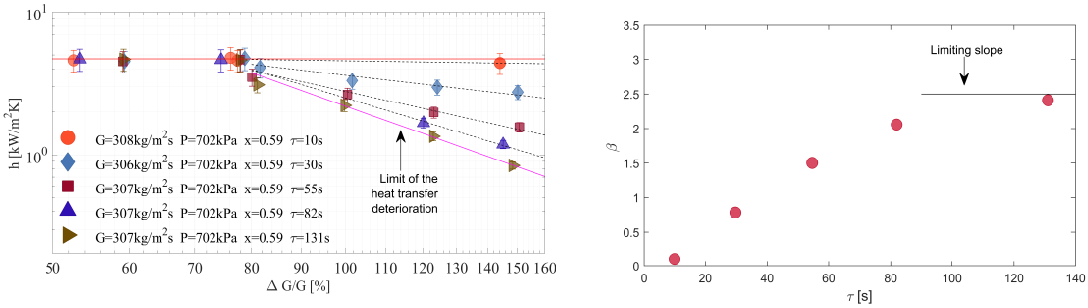

(a) (b)

FIG. 3: Heat transfer coefficient deterioration for controlled flow oscillations for fixed periods for an averaged thermodynamic quality of 0.6.

ing multiple micro-nozzles and reentry microcavities," Applied Physics Letters **110** (2017), 10.1063/1.4973495.

[5]L.-j. Guo, Z.-p. Feng, and X.-j. Chen, "Transient convective heat transfer of steam water two-phase ow in a helical tube under pressure drop type oscillations," International Journal of Heat and Mass Transfer **45**, 533–542 (2002).

[6]M. Sørum and C. Dorao, "Experimental study of the heat transfer coefficient deterioration during density wave oscillations," Chemical Engineering Science **132** (2015), 10.1016/j.ces.2015.03.039.

[7]M. Ozawa, H. Umekawa, K. Mishima, T. Hibiki, and Y. Saito, "CHF in Oscillatory Flow Boiling Channels," Chemical Engineering Research and Design **79**, 389–401 (2001).

[8]S. Wang, C. Chen, and T. Lin, "Oscillatory subcooled flow boiling heat transfer of R-134a and associated bubble characteristics in a narrow annular duct due to flow rate oscillation," International Journal of Heat and Mass Transfer **63**, 255–267 (2013).

[9]E. Manavela Chiapero, M. Fernandino, and C. Dorao, "On the influence of heat flux updating during pressure drop oscillations - A numerical analysis," International Journal of Heat and Mass Transfer **63** (2013), 10.1016/j.ijheatmasstransfer.2013.03.047.

[10]C. A. Chen, T. F. Lin, W. M. Yan, and M. Amani, "Time periodic evaporation heat transfer of R-134a in a narrow annular duct due to mass flow rate oscillation," International Journal of Heat and Mass Transfer **118**, 154–164 (2018).

Chapter 4 Control of surface wettability

4.1 Wetting transition on bioinspired conical microstructures (Paper 5)

An interaction between a surface and liquid, which can be represented by the wettability, has been considered as an important aspect for improving heat transfer performance. Tuning the wettability of a surface by fabricating microstructures on it has been the focus of previous studies. Among the fabrication strategies, biomimetic surfaces have been considered among the most promising for controlling wettability. However, how the biomimetic surface quantitatively affects wettability has not been explained. In this study, conical microstructures are chosen due to their ability to show a wide range of wetting properties. Here, it is assumed that the geometric parameters such as the spacing and height of the conical microstructures, have an important role in controlling the wettability. In **Paper 5**, a parametric study on the wettability in relation to the geometric parameters of conical microstructures is performed in order to determine the effect of biomimetic structures on wettability. A sensitive control of the geometric parameters was successfully managed in the fabrication step. Example for the difficulties in fabrication is presented in Appendix A. A transition from the superhydrophobic state to the superhydrophilic wetting state was observed by varying the geometric parameters. A major finding of this work is the possibility of controlling the wettability by geometric parameter without external excitation and the observation of the drastic wetting transition between Cassie-Baxter and Wenzel states with varying geometric parameter.

Paper 5

Wetting State Transitions over Hierarchical Conical Microstructures.

Park, I. W., Fernandino, M., and Dorao, C. A.

Advanced Materials Interfaces, 5, 1701039, 2018.

Vol. 5 • No. 5 • March 9 • 2018

www.advmatinterfaces.de

ADVANCED MATERIALS INTERFACES

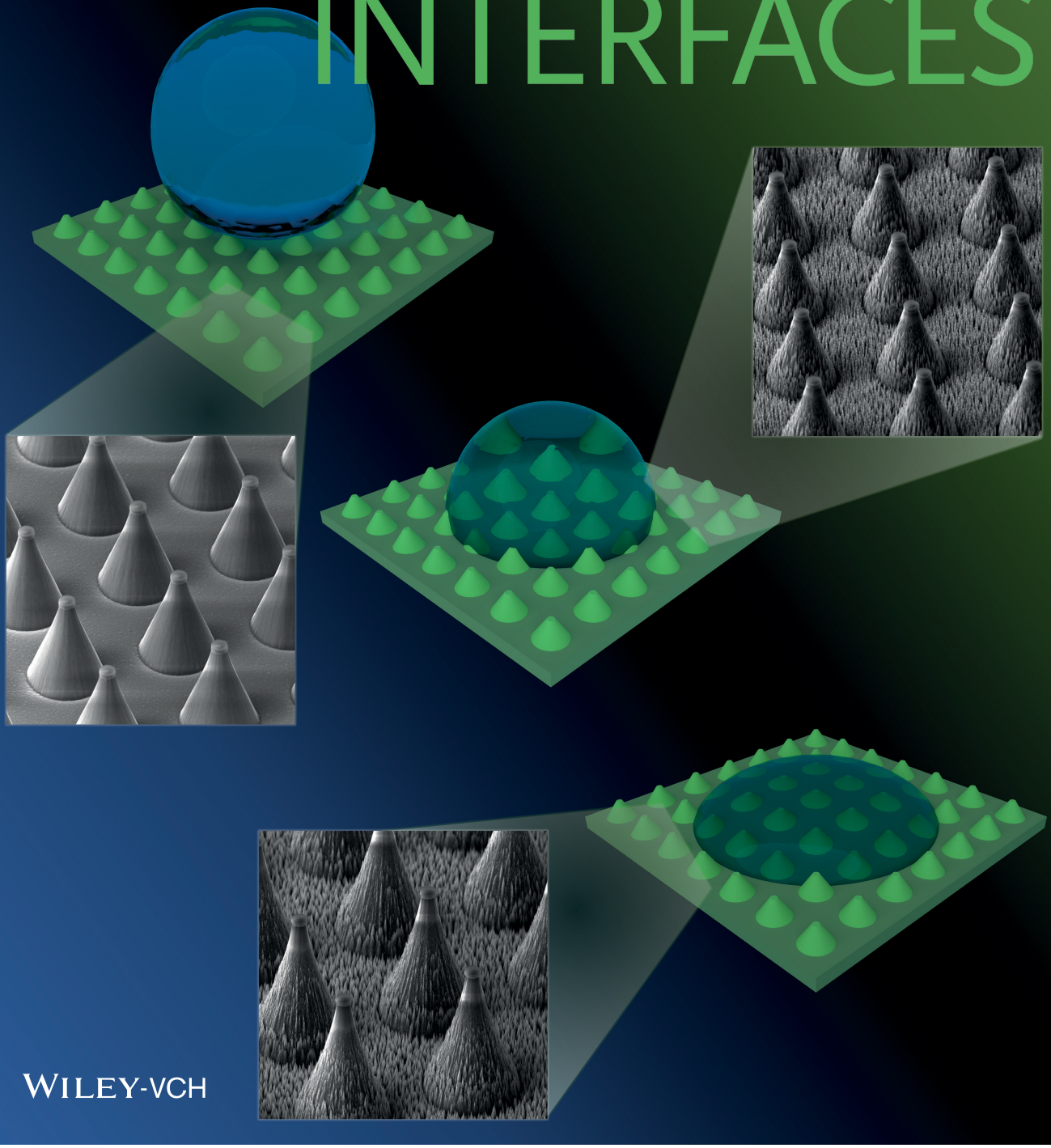

WILEY-VCH

ADVANCED MATERIALS INTERFACES
www.advmatinterfaces.de

Wetting State Transitions over Hierarchical Conical Microstructures

*Il Woong Park, Maria Fernandino, and Carlos A. Dorao**

Advancing in a better understanding of the physics of wetting requires to be able to develop surfaces with well-controlled roughness by controlling the microstructure morphology. In this study, patterned truncated cones and hierarchical conical structures are fabricated. The wetting properties of the fabricated surfaces are measured for identifying the importance of the geometrical parameters on the wetting states ranging from superhydrophobic to superhydrophilic. In particular, the wetting transition from Cassie–Baxter to Wenzel state and its dependence on the geometrical parameters is investigated. It is observed that the transition is dependent on the center-to-center distance and the height of the structures.

1. Introduction

The wettability of a surface is a fundamental physical property with relevance in many scientific and industrial applications.[1,2] It has been observed that many surfaces in nature exhibit superhydrophobic and superhydrophilic characteristics tailored to some particular functionality.[3,4] The properties of such surfaces have motivated researchers mimicking them with the goal of developing novel surfaces with customized properties.[5–7] However, major challenges have remained related to the fabrication techniques for achieving optimal controllability of the properties of the surfaces which can also contribute to a better understanding of the wetting phenomena.[5]

Recent progress in fabrication techniques has allowed a precise control of the surface properties in particular in terms of shape and size for studying wetting phenomena.[8–15] For example, Liu and Kim[8] fabricated a superhydrophobic surface with a doubly re-entrant nano overhangs structure. This surface has shown a high apparent contact angle even for liquids with low surface tension. Chu and Nemoto[9] fabricated surfaces with micropillars and hierarchical structures showing a superhydrophobic state. In addition, a negative relation between the apparent contact angle and the dynamic contact angle was observed. Xue et al.[14] fabricated microcones by etching an inclined surface with polystyrene array in order to study the effect of geometrical parameters of microcones on the apparent contact angle, the contact angle hysteresis, and the sliding angle. Cai et al.[15] studied the effect of the geometrical parameters of the microstructures and side wall angle on the wetting properties. In particular, it was observed that the microstructures having a side wall angle lower than 90° give higher contact angle compared with the microstructures having side wall angle higher than 90°.

The wetting phenomena in roughened surfaces are normally referred to as the Wenzel and Cassie–Baxter states.[16–19] The Wenzel state describes a homogeneous wetting regime where the liquid is contacting with the surface, while the Cassie–Baxter state describes a regime where an empty volume between a liquid droplet and solid surface is observed. Several studies have been focused on the transition between the Cassie–Baxter state and the Wenzel state (Cassie–Wenzel transition)[20–26] and also the stability of the Cassie wetting state.[27] However, which are the dominant physical phenomena controlling each state and its transition remains an open research issue. In particular, the transition has been explained in terms of the threshold of the energy barrier, meniscus touching on the substrate, air cushions beneath the droplet, and critical pressure.

The control of the Cassie–Wenzel transition between superhydrophilic and superhydrophobic surfaces can contribute to the design of surfaces with customized properties in a diverse range of applications. At the same time, controlling the Cassie–Wenzel transition can contribute to an improvement of the understanding of the wetting states transition. For this reason, experimental studies have attempted to gain control of the Cassie–Wenzel wetting transition by an external excitation such as vibration or electricity.[28–30] However, such active control techniques of the Cassie–Wenzel wetting state can present limitations in some applications. This fact has motivated the need for controlling the Cassie–Wenzel wetting in a passive manner by varying the geometrical parameters of the surface without external excitations. Achieving a stable condition of the Cassie–Wenzel state could be helpful for potential applications on microfluidics.[31]

The aim of this study is to fabricate surfaces presenting superhydrophobic and superhydrophilic states with a wide range of geometric parameters. The selected surfaces are motivated in conical structures observed in nature showing both superhydrophilic and superhydrophobic properties.[4] For example, the Ruellia devosiana leaf shows impressive rapid spreading of water and its leaves present a conical topography. The leaves of the lotus flower which have a hierarchical conical topography

I. W. Park, Prof. M. Fernandino, Prof. C. A. Dorao
Kolbjørn Hejes v1b
7491 Trondheim, Norway
E-mail: carlos.dorao@ntnu.no
The ORCID identification number(s) for the author(s) of this article can be found under https://doi.org/10.1002/admi.201701039.

DOI: 10.1002/admi.201701039

show self-cleaning properties as result of superhydrophobicity. Two types of biomimetic microstructures are fabricated with the silicon substrate in this work, namely, truncated cones which are motivated from the Ruellia devosiana leaf and hierarchical conical structures which are motivated from the lotus leaf. It has been reported in the literature that microstructures with lower than 90° of sidewall angle have an advantage in achieving high apparent contact angle.[15] Moreover, fabrication of these structures with a conical shape in a silicon substrate could be beneficial in terms of the mechanical response.[32] In this work, in order to cover both superhydrophobic and superhydrophilic states, the height and the center-to-center distance of the structures were controlled. The fabrication of the samples is based on photolithography and cryogenic reactive ion etching (RIE). The wetting properties and wetting transition of the fabricated surfaces are measured and correlated with the geometrical properties.

2. Results and Discussion

Both truncated and hierarchical cones were fabricated by lithography and dry etching process as shown in **Figure 1**. Three different heights were used for the microcones surface, namely, 35, 55, and 75 μm, while 16 different center-to-center distances between cones varying from 15 to 360 μm were used.

The apparent contact angle[33] and the contact angle hysteresis were measured. **Figure 2**a shows the apparent contact angle and the contact angle hysteresis as a function of the varying center-to-center distance of the truncated cones and hierarchical cones with a height of 75 μm, named TC75 and HC75 samples, respectively. The center-to-center distance is varied from 15 to 360 μm observing three distinctive regions for the truncated cones, that is, TC75 samples. The first region corresponds to the Cassie–Baxter state for the center-to-center distance from 15 to 60 μm. The apparent contact angle and contact angle hysteresis of the Cassie–Baxter state shows a linear dependency of the center-to-center distance. The second region corresponds to the Cassie–Wenzel transition corresponding to center-to-center distance from 60 to 70 μm. The apparent contact angle decreases abruptly in this region. This trend has also been observed for flat-top micropillars.[24] Finally, the third region corresponds to the Wenzel state and the contact angle shows independence of the center-to-center distance of the cones.

The hierarchical cones, that is, HC75 samples, show three distinctive regions. The first region corresponds to the Cassie–Baxter state for the center-to-center distance from 15 to 50 μm, that is, coinciding with the truncated cones. The apparent contact angle of the truncated cones and hierarchical cones are similar in the Cassie–Baxter state indicating that the microstructure has no influence in the contact angle. The area fraction or the roughness of the contacting surface on the top part can be considered an important parameter controlling the apparent contact angle in Cassie–Baxter state. The second region corresponds to a sharp Cassie–Wenzel transition occurring for the center-to-center distance from 50 to 60 μm, that is, quite similar to the case of truncated cones. The third region corresponds to a superhydrophilic state. It is remarkable that the surface with hierarchical cones shows a transition from the superhydrophobic state to the superhydrophilic state by a change in the center-to-center distance. In particular, the transition occurs in less than 10 μm of the center-to-center distance. Both truncated cones and hierarchical cones show decreasing and overlapping contact angle hysteresis with increasing center-to-center distance in the Cassie–Baxter state. Similar to the apparent contact angle, the hierarchical structure has no apparent influence on the contact angle hysteresis. In terms of applicability, a low contact angle hysteresis surface possesses the property of self-cleaning when the apparent contact angle is high. In this sense, the fabricated surface shows a decreasing contact angle hysteresis and increasing apparent contact angle between 15 and 60 μm of center-to-center distance. Therefore, a surface with low contact angle hysteresis and high apparent contact angle for self-cleaning applications can be fabricated by modifying the spacing of microstructures. At the Cassie–Wenzel transition, the contact angle hysteresis shows a sharp increase, and then the contact angle hysteresis decreases for the case of the truncated cones while slightly increases for the case of the hierarchical

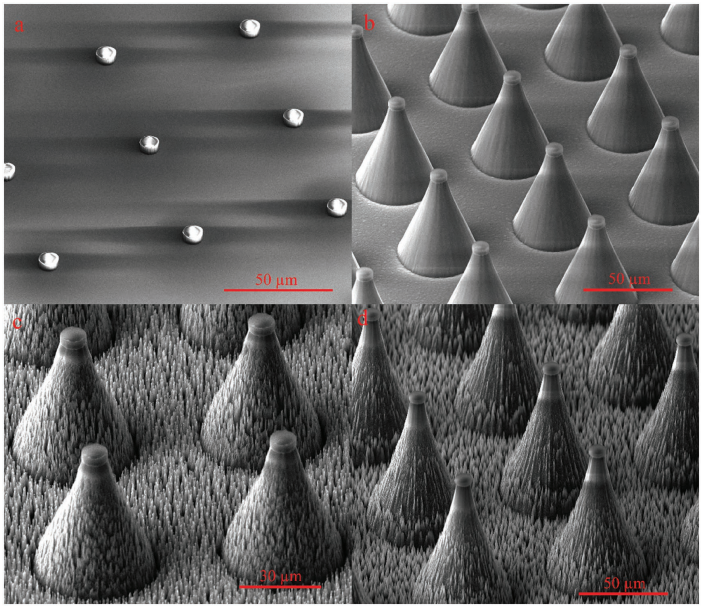

Figure 1. SEM images of microconical structures. a) SU-8 structures (4 μm of height). b) Truncated microcones (55 μm of height). c) Hierarchical microconical structures (55 μm of height). d) Hierarchical microconical structures (75 μm of height).

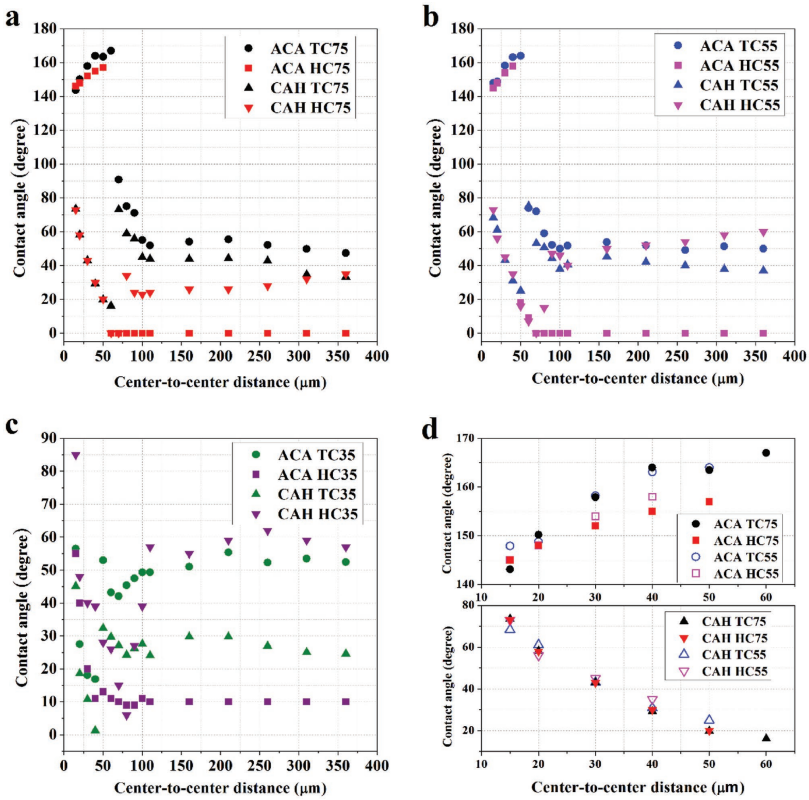

Figure 2. Apparent contact angle (ACA) and contact angle hysteresis (CAH) of truncated cone (TC) and hierarchical cone (HC) of a) 75 μm of height, b) 55 μm of height, c) 35 μm of height, and d) Cassie–Baxter state.

cones. In Figure 2a, it is possible to see that the advancing and receding angles were measured as zero for the cases of 60 and 70 μm of center-to-center distance because a droplet was soaked fast into the surface. These two samples show zero apparent contact angle with zero contact angle hysteresis.

Figure 2b shows both apparent contact angle and contact angle hysteresis of truncated cones and hierarchical cones with a height of 55 μm, named TC55 and HC55 samples, respectively. In general, similar characteristics compared to the TC75 and HC75 samples are observed. However, for the case of the hierarchical cones with 50 and 60 μm of center-to-center distance impregnating Cassie state[16] are observed. It seems like that there was a lack of the volume between the structures to be a superhydrophilic state, and the leftover liquid which was not soaked between structures formed a droplet on top of the impregnating surface.

In Figure 2c, the apparent contact angle and the contact angle hysteresis of truncated cones and hierarchical cones with a height of 35 μm are presented, named TC35 and HC35 samples, respectively. In these samples, the hydrophobic state was not observed. It could be assumed that there is a threshold height of the microstructure or volume of the air cushion for maintaining droplets in Cassie–Baxter state. In these samples, impregnating Cassie state was observed in both truncated and hierarchical cone.

In Figure 2d, the apparent contact angle and the contact angle hysteresis for the Cassie–Baxter state are highlighted. The apparent contact angle and contact angle hysteresis show an opposite trend on the center-to-center distance as observed by Chu[9] and Xue.[14] The highest apparent contact angle of 167° with a contact angle hysteresis of 16° was achieved with the truncated cones with 60 μm of center-to-center distance. In terms of the lotus effect, a higher apparent contact angle and lower contact angle hysteresis are desired. The plot shows that the apparent contact angle and contact angle hysteresis are in negative relation. There is a difference of 10 μm of center-to-center distance between the truncated cones and hierarchical cones in terms of the location of the Cassie–Wenzel transition. In addition, there were differences of 10 μm of center-to-center distance between 75 μm of the height of the microconical structures and 55 μm of them. In summary, this plot shows that the surface with truncated cones with higher structures provides the Cassie–Baxter state in higher center-to-center distance condition. For achieving the desired wetting state with respect to the lotus effect, it seems like that higher center-to-center distance

provides higher apparent contact angle with lower contact angle hysteresis. Thus, fabrication of high truncated cones could be a solution for fabricating a surface with a high apparent contact angle with low contact angle hysteresis.

Figure 3a,b illustrates different wetting states for the truncated cones and for the hierarchical cones in this study. Four different wetting states which are the Cassie–Baxter state, the Wenzel state, superhydrophilic state, and the impregnating Cassie state were observed with the different microstructures. As reported by Liu[25] and Shahraz,[26] the apparent contact angle or the wetting states could be connected with structural or morphological parameters such as height, or ratio between diameter, pitch, and groove width. Both theoretical studies show that the Cassie–Baxter state exists where the spacing between the structures is low which is also observed in this work. In terms of the height of the microstructures, it has been reported that the Cassie–Baxter state is observed when the height of the structures is high.[26] The Cassie–Wenzel transition is not affected by the height of the structures, as reported by Liu.[25]

The maps in Figure 3a,b depict that the Cassie–Wenzel transition could occur due to changes in both height and spacing of the structures. Barbieri[24] has observed that the transition from the Cassie–Baxter state to Wenzel state can be occurred by increasing the pitch and decreasing the height of the structure. The maps also show the occurrence of superhydrophilic and impregnating Cassie states. It was possible to observe that the presence of the hierarchical structures transforms the Wenzel state to superhydrophilic or the impregnating Cassie state by comparing the two graphs. Furthermore, it shows that the hierarchical structures enhance the spreading of the liquid. It was observed that there is a change between the superhydrophilic and impregnating Cassie state in the sample with hierarchical cones. This fact could be explained in terms of the amount of the volume between the microstructures which can capture the liquid. This could be the reason why the superhydrophilic state was able to be achieved when the condition is in the upper right corner of the map, which represents the large volume between the structures in the graph. Therefore, the geometric parameters have a significant effect on the wetting states and the wetting transition.

In this part, the experimental results in this work are discussed in terms of models for the wetting transition from previous studies.[15,34–36] The theoretical result of the critical transition pressure was calculated in terms of the width of the microstructures by Cai et al.[15] in a previous study. Blow and Yeomans[34] adapted the surface evolver algorithm in order to predict the Cassie–Wenzel wetting transition. This algorithm was validated with the models of the free energy and the Laplace pressure from the previous study by Crisp and Thorpe.[35] It has been observed that the high spacing between the structures can cause the low-pressure drop for leading to the collapse of the droplet. Based on this model, the critical pressure was calculated for the experimental points in this study as shown in **Figure 4**. The used model for the critical pressure can be written in Equation (1), where D_T is the diameter of the top surface of the microstructure, γ is the surface tension, θ_A is the apparent contact angle, and P is the spacing between the microstructures

$$\Delta P_{\text{critical}} = \frac{-2\pi D_T \gamma \cos\theta_A}{P^2 - \pi D_T^2} \tag{1}$$

In Equation (1), the measured apparent contact angle in case of the TC55 was adapted. The effect of the height of the microstructures and the shape of the microstructures were not considered in this model. The diameter of the top surface was selected as a diameter of the micropillars from the model in this calculation. The model suggests that the increase of the spacing of the structures can result in a lower critical pressure. Furthermore, a lower critical pressure could collapse the hydrophobic state. However, the model is directly dependent on the measured apparent contact angle.

Two types of the breakdown of Cassie–Baxter state which were observed in this experiment could be compared with the developed models in previous studies. Two types of the breakdown which are due to the increased spacing between the microstructures and the decreased height of the microstructure could be identified. The first type of the breakdown could

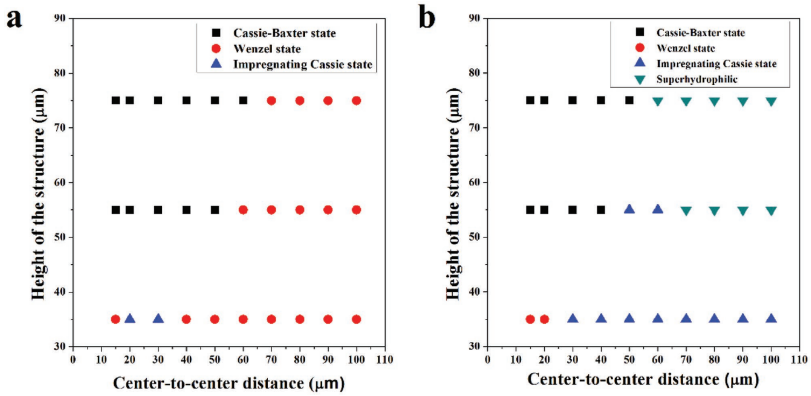

Figure 3. Different wetting states depend on geometrical parameter for a) truncated cones and b) hierarchical cones.

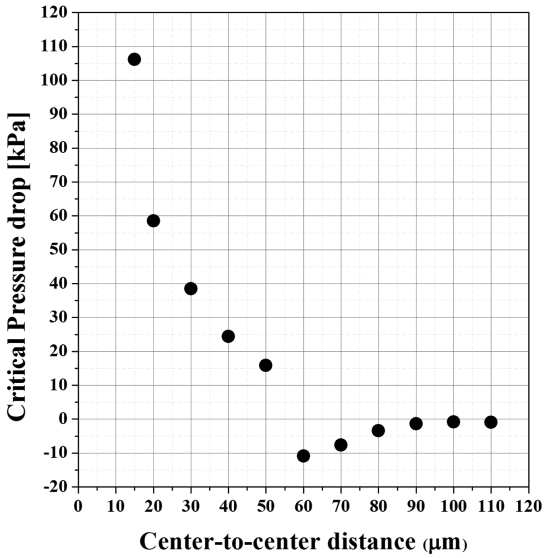

Figure 4. Calculated critical pressure drop for leading to the collapse of the droplet depends on the center-to-center distance based on the parameter from the experiment.

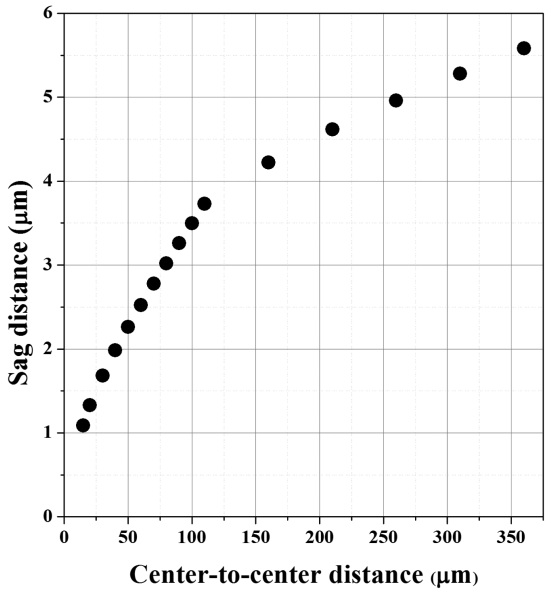

Figure 5. Calculated critical sag distance depends on the center-to-center distance based on the parameter from the fabricated microstructures.

be explained with the concept of the critical pressure.[34–36] As shown in Figure 4, the critical pressure for leading the collapse becomes low when the spacing between the structures becomes high.

To identify the effect of the height regarding the breakdown of the hydrophobicity, the model with the height of the microstructures should be considered. For the case of the sag transition,[37,38] Patankar[37] suggests a model for obtaining a minimum height to avoid the sag transition to maintain the Cassie state. In the sag transition, it is assumed that the bending of the liquid–gas interface oriented from the corner of the microstructures. The minimum height to avoid the sag transition was calculated based on the geometrical parameter from the experiment as shown in **Figure 5**. The model for the minimum height is given by Equations (2) and (3)

$$H = R\left(1-\sqrt{1-\frac{P^2}{2R^2}}\right) \tag{2}$$

$$R = \frac{2P\left(1+\frac{P}{2D_T}\right)}{-2\cos\theta_A} \tag{3}$$

We assumed the apparent contact angle as 150°, and the right angle of the sidewall. If the sag distance was calculated in a range between 35 and 55 μm, it could be concluded that the sag transition was the dominant effect to break the hydrophobicity in this experiment. However, the calculated sag distance based on the model was less than 6 μm. It could imply that the sag transition was not the dominant effect to collapse the hydrophobicity in this experiment when the height of the structures decreased. On the other hand, it could be explained that there was a touchdown between the liquid–gas interface and the sidewall as the solid–gas interface in the experiment. It could be meaningful to evaluate the possibility of the touchdown between the interfaces when the structures have a conical shape.

3. Conclusion

Microconical structures with well-organized geometric parameters have been fabricated by photolithography and RIE process. In total, 96 different samples were fabricated comprising two structure types, three heights, and 16 center-to-center distances. Different wetting properties were identified ranging from superhydrophobic state to superhydrophilic. In the case of superhydrophobic state, surfaces with high apparent contact angle and low contact angle hysteresis were obtained. With regard to the lotus effect, it has been observed that a path for fabricating a surface with a high apparent contact angle with low contact angle hysteresis can be achieved with high truncated cones. Furthermore, a drastic wetting transition from Cassie–Baxter state to Wenzel state was observed in the case of hierarchical cones compared to the more gradual transition for the case of truncated cones. It is important to note that the transition was not forced by external excitation but instead due to changes in the geometrical characteristics of the surface. Finally, the present study covers geometrical structures over a scale of the dozens of micrometers compared to previous studies limited to a narrower range of dimensions opening the possibility of bringing a broader view of the surface wettability problem.

4. Experimental Section

Fabrication Procedure of Microconical Structures: The challenge in the present work was to fabricate two types of conical structures, namely, truncated cones and hierarchical cones. The main challenge in this work is to have control of the position of the relatively large microconical structures called truncated cones and being able to add small microconical structures on top of the previous one for producing the hierarchical cones.

The structures were fabricated on top of a silicon wafer using photolithography and dry etching. Single-side polished silicon wafers ({100}, P-type, containing boron as dopant) were prepared for constructing microstructures. The silicon wafer was rinsed with ethanol, isopropanol (IPA), acetone, deionized water in sequence and then dried with the N_2 flow. Additionally, the wafer was treated with oxygen plasma for 3 min in order to remove impurities and contaminants in a plasma chamber (Diener Electronics Femto). After the cleaning steps, photolithography was conducted for imprinting patterns on top of the wafer. For this process, a film of 4 μm thickness of SU-8 negative photoresist from MicroChem was spin-coated. After spin-coating, the wafer was baked on the heating plate for 1 min at 65 °C and 2 min at 95 °C. After the pre-baking step, ultraviolet (UV) light exposure was conducted on top of the coated wafer. In this exposure step, a photomask which is a 5 in. chrome glass mask (Micro Lithography Services, UK) was placed between the UV light source and the silicon wafer. There were 16 patterns of circles in the square grid on top of the photomask. These patterns were imprinted on top of the wafer by exposing UV light with a Mask Aligner (Karl Süss, MA-6). A wavelength of 365 nm and 200 mJ cm^{-2} of exposure dose were used as parameters for the UV exposure. After UV light exposure, the wafer was baked again on the heating plate for 1 min at 65 °C and 2 min at 95 °C. The patterns on the wafer were developed in Mr-DeV 600 (Micro Resist Technology GmbH, Germany) bath. After the development step, the wafer was cleaned with IPA and deionized water in sequence and dried with the N_2 flow. By following this procedure, pillars of SU-8 in size of 9 µm of diameter and 4 µm of height were constructed on top of the silicon wafer as shown in Figure 1a. The conical structures were fabricated based on these SU-8 pillars.

The hierarchical conical structures were fabricated by two steps of cryogenic RIE processes. The first RIE process step produced the large truncated cones and the second RIE process step added the microcones to the surface. In the previous study, the superoleophobic surface was achieved with the hierarchical nanoscaled topography of fluorinated polyethylene surface by the plasma etching.[39] The two RIE steps were done in an ICP-RIE Cryo Reactor (Plasmalab 100 – ICP180, Oxford Instruments, UK). The fabrication of the cones was achieved by controlling the etching profile such that the side wall angle is less than 90°. This side wall angle and the taper angle are highly dependent on cryogenic temperature and composition of gas flows.[40,41] In particular, microcones can be generated with a random distribution with the RIE process.[42] In the present work, the etching recipe was developed for fabricating only large truncated cones at precise locations determined by the SU-8 pillars suppressing the random generation of microcones. The etching parameters were developed for achieving the desired side angle of etching profile while suppressing of randomly generated structures. Etching parameters including capacitive coupled plasma (CCP) radio frequency (RF) power, inductively coupled plasma (ICP) power are described as first RIE in **Table 1**. For producing small cones, black silicon method was selected.[43] It was reported that DRIE etching process is suitable for producing small-size structures on top of the microstructures.[44,45] Selected parameters for second RIE process are described in Table 1.

In summary, truncated cones TC were obtained after a first RIE step with three different heights of 35, 55, and 75 µm on top of the silicon wafer and the samples are named TC35, TC55, and TC75, respectively. Each TC35, TC55, and TC75 set include 16 samples with different center-to-center distances. A scanning electron microscopy (SEM) image of TC55 is shown in Figure 1b. In the figure, it is able to observe truncated cones on top of the silicon surface and SU-8 pillars on top of the truncated cones. The hierarchical conical structures were obtained by adding a second RIE process to TC35, TC55, and TC75 samples. The samples are named HC35, HC55, and HC75 following the height of the truncated cones. SEM images of HC55 and HC75 are shown in Figure 1c,d. Small structures were produced not only on the bottom surface between truncated cones but also on the side surface of truncated cones. In this process, the bottom and the side surfaces were roughened selectively when the top surface of SU-8 was kept as a smooth surface. Parameters of the microstructures are described in **Table 2**. The main parameters of the structures are height of the truncated cone H_T, height of photoresist H_P, height of silicon H_C, diameter of top surface of truncated cone D_T, diameter of bottom part of conical structure D_B, and center-to-center distance P. In total, 96 samples (48 samples of truncated cone and 48 samples of hierarchical cone) were prepared for identifying wetting parameters.

The silicon substrate of the silicon wafer {100} was used as hard microstructures. Silicon-based microfabrication could be important to overcome the robustness of the microstructures. The hard matter as a rigid solid part could give more consistent interaction between the liquid in terms of the three-phase contact line compared with the soft matter which could be deformed as an elastic solid substrate. It could be the reason why the drastic wetting transition was observed with changing the geometric parameter with the hard solid substrate.

It could be helpful to discuss the reproducibility and the shelf-life of the samples. In case of the lithography step, it was able to obtain close geometrical parameters of the photoresist structures. However, reproducing of the conical shape in dry etching step should be considered much sensitively. It means that the same etching recipe could not provide identical geometrical parameters of the cones. This is because the condition of the chamber of the cryo affects the etching profile sensitively. For easier reproduction, it was important to make the chamber condition stable, by repeating cleaning steps and etching steps with a bare wafer. After this, the amounts of the oxygen and sulfur hexafluoride which are dominant parameters for deciding the sidewall angle could be adjusted for obtaining targeted sidewall angle of the structures by trial and error. In order to check the shelf-life of the structures, SEM images of the samples were obtained again after ten months. In the SEM images, there was no significant change after ten months.

Scanning Electron Microscope: An FEI Helios dual-beam focused ion beam scanning electron microscope (FIB-SEM) was used to characterize microstructures. Especially, the height of microstructures was measured by tilting the sample 52° inside the microscope. 15 and 20 kV of voltages were used for taking SEM images. This is because there was a deformed image of the SU-8 part due to the scattering in low voltage condition such as 5 or 10 kV.

Contact Angle Measurement: The apparent contact angle and the dynamic contact angle were measured for each sample. An optical

Table 1. RIE etching parameters.

	ICP power [W]	RF power [W]	Temperature [°C]	Pressure [mTorr]	SF_6 flow [sccm]	O_2 flow [sccm]	Time [s]
First RIE striking	300	20	−80	20	100	20	10
First RIE etching	500	20	−80	50	100	20	1200, 1800, 2400
Second RIE striking	300	20	−120	20	100	17.5	10
Second RIE etching	500	20	−120	50	100	17.5	1200

Table 2. Parameters of the microstructures.

	TC[a] 35	TC 55	TC 75	HC[b] 35	HC 55	HC 75
H_T[c] [μm]	35	55	75	37	58	79
H_P[d] [μm]	4	4	4	4	4	4
H_S[e] [μm]	31	51	71	33	54	75
D_T[f] [μm]	9	9	9	9	9	9
D_B[g] [μm]	30	45	55	30	45	55
P[h] [μm]	15–315	15–315	15–315	15–315	15–315	15–315

[a]Truncated cone; [b]Hierarchical cone; [c]Height of truncated cone; [d]Height of photoresist; [e]Height of silicon; [f]Diameter of top surface of truncated cone; [g]Diameter of bottom part of conical structure; [h]Center-to-center distance.

tensiometer (Attension Theta, Biolin Scientific, Sweden) was used for measuring contact angles. The apparent contact angle was measured with 12.6 μL of gently dropped distilled water droplet. Droplets were generated with a rotating type of syringe (Hamilton Co, Reno, NV). For obtaining contact angle hysteresis, advancing and receding angles were measured with a changing volume of the DI water. Both sessile and meniscus options were applied depending on the shape of liquid on the surface. After measuring the apparent contact angle of the droplet, the contact angle hysteresis was obtained by measuring advancing and receding contact angle. For measuring two contact angles, the needle penetrated softly into the droplet. After inserting the needle, the liquid was injected and ejected for changing the volume of the liquid. The liquid was injected from 10 to 80 μL for measuring the advancing angle and ejected from 40 to 5 μL for measuring the receding angle. By recording the high-speed images, the advancing and receding angle of the droplet was obtained when the volume of the liquid was changing. For the contact angle hysteresis, the reproducibility was focused during the experiments. From this, the minimum and maximum point were obtained when the minimum or maximum dynamic contact angle can be obtained in repeat test.

Apparent Contact Angle of Reference Surfaces: As the fabricated surfaces are presenting particular properties, the local wetting properties of each surface type which are the top surface of the truncated cone, the bottom surfaces between truncated cones with and without the small cones were evaluated as a reference surface. For this evaluation, three different surfaces were treated by the same RIE processes but without the patterned SU-8 pillars resulting in reference surfaces mimicking the local characteristics of the conical surfaces. For fabricating the first reference surface, the silicon surface was treated by 20 and 40 min of the first RIE process. After this etching, the apparent contact angles were measured as 54° and 58°. This wetting property represents the bottom surface between truncated cones when the small cones are not present. For the second reference surface, the second RIE process was conducted on the previous reference surfaces. The apparent contact angles of the second reference surfaces were measured as 62° and 65°. The apparent contact angles of the second reference surfaces are in good agreement with a previous study[46] which shows an apparent contact angle of 62.3° for a black silicon surface. The second reference surface represents the bottom surface between truncated cones when the small cones are present. For the third reference surface, a wafer was spin-coated with a uniform layer of SU-8 that was baked and exposure by UV light without a mask. After this step, the surface was treated by both types of RIE processes showing an apparent contact angle 66°. The apparent contact angle was measured to be less than 2° before and after the etching process. This wetting property represents the top surface of the SU-8 surface on top of the truncated cones. During the fabrication steps, the small differences in the apparent contact angle between the reference surfaces were considered. The parameters for both RIE steps were adjusted based on the wetting properties of the reference surfaces. As a consequence, the three reference surfaces have an apparent angle in the range from 54° to 66°. From this, it was possible to avoid significant differences of wetting properties between the local surfaces of microconical structures. This is because the polished silicon surface which is expected to exist on a top surface of a structure where the SU8 is removed has a hydrophilic state. In short, the SU8 has a role in controlling the local wetting condition in the similar range.

Acknowledgements

The Ph.D. fellowship (Il-Woong Park) financed by the NTNU-SINTEF Gas Technology Centre is gratefully acknowledged. The Research Council of Norway is acknowledged for the support to the Norwegian Micro- and Nano-Fabrication Facility, NorFab, for the fabrication and characterization of samples at the NTNU Nanolab facility.

Conflict of Interest

The authors declare no conflict of interest.

Keywords

biomimetic, hierarchical cone, microstructure, superhydrophobic/philic surfaces, wetting transition

Received: August 21, 2017
Revised: November 6, 2017
Published online:

[1] Z. Wang, M. Elimelech, S. Lin, *Environ. Sci. Technol.* **2016**, *50*, 5.
[2] L. Wen, Y. Tian, L. Jiang, *Angew. Chem., Int. Ed.* **2015**, *54*, 11.
[3] W. Barthlott, C. Neinhuis, *Planta* **1997**, *202*, 1.
[4] K. Koch, W. Barthlott, *Philos. Trans. R. Soc., A* **2009**, *367*, 1893.
[5] Y. Y. Yan, N. Gao, W. Barthlott, *Adv. Colloid Interface Sci.* **2011**, *169*, 2.
[6] L. Zhang, N. Zhao, J. Xu, *J. Adhes. Sci. Technol.* **2014**, *28*, 8.
[7] C. Frankiewicz, D. Attinger, *Nanoscale* **2016**, *8*, 7.
[8] T. Liu, C. J. Kim, *Science* **2014**, *346*.
[9] D. Chu, A. Nemoto, *Appl. Surf. Sci.* **2014**, *300*, 117.
[10] H. Bellanger, T. Darmanin, E. T. de Givenchy, F. Guittard, *Chem. Rev.* **2014**, *114*, 5.
[11] H. Ems, S. Ndao, *Appl. Surf. Sci.* **2015**, *339*, 137.
[12] M. Kanungo, S. Mettu, K. Y. Law, S. Daniel, *Langmuir* **2014**, *30*, 25.
[13] S. Utech, K. Bley, J. Aizenberg, N. Vogel, *J. Mater. Chem. A* **2016**, *4*, 18.
[14] P. Xue, J. Nan, T. Wang, S. Wang, S. Ye, J. Zhang, Z. Cui, B. Yang, *Small* **2016**, *13*, 4.
[15] T. M. Cai, Z. H. Jia, H. N. Yang, G. Wang, *Colloid Polym. Sci.* **2016**, *294*, 5.
[16] E. Bormashenko, *Adv. Colloid Interface Sci.* **2015**, *222*, 92.
[17] B. N. Young, *Colloids Surf., A* **2009**, *345*, 1.
[18] R. N. Wenzel, *Ind. Eng. Chem.* **1936**, *28*, 988.
[19] A. B. D. Cassie, S. Baxter, *Trans. Faraday Soc.* **1944**, *40*, 546.
[20] D. Murakami, H. Jinnai, A. Takahara, *Langmuir* **2014**, *30*, 8.
[21] P. Papadopoulos, L. Mammen, X. Deng, D. Vollmer, H. J. Butt, *Proc. Natl. Acad. Sci. USA* **2013**, *110*, 9.
[22] T. Koishi, K. Yasuoka, K. S. Fujikawa, T. Ebisuzaki, X. C. Zeng, *Proc. Natl. Acad. Sci. USA* **2009**, *106*, 21.
[23] Q. S. Zheng, Y. Yu, Z. H. Zhao, *Langmuir* **2005**, *21*, 26.
[24] L. Barbieri, E. Wagner, P. Hoffmann, *Langmuir* **2007**, *23*, 4.
[25] T. Liu, Y. Li, X. Li, W. Sun, *J. Phys. Chem. C* **2017**, *121*, 18.
[26] A. Shahraz, A. Borhan, K. A. Fichthorn, *Langmuir* **2012**, *28*, 40.

[27] G. Whyman, E. Bormashenko, *Langmuir* **2011**, *27*, 8171.
[28] W. Lei, Z. H. Jia, J. C. He, T. M. Cai, *Appl. Phys. Lett.* **2014**, *104*, 181601.
[29] G. Liu, L. Fu, A. V. Rode, V. S. Craig, *Langmuir* **2011**, *27*, 6.
[30] N. Kumari, S. V. Garimella, *Langmuir* **2011**, *27*, 17.
[31] Z. Liu, Y. Wu, B. Harteneck, D. Olynick, *Nanotechnology* **2012**, *24*, 1.
[32] K. Sekeroglu, U. A. Gurkan, U. Demirci, M. C. Demirel, *Appl. Phys. Lett.* **2011**, *99*, 063703.
[33] A. Marmur, C. Della Volpe, S. Siboni, A. Amirfazli, J. W. Drelich, *Surf. Innov.* **2017**, *5*, 3.
[34] M. L. Blow, J. M. Yeomans, *Int. J. Mod. Phys. C* **2012**, *23*, 1240013.
[35] D. J. Crisp, W. H. Thorpe, *Disc. Faraday Soc.* **1948**, *3*, 210.
[36] M. J. Hancock, M. C. Demirel, *MRS Bull.* **2013**, *38*, 391.
[37] N. A. Patankar, *Langmuir* **2010**, *26*, 8941.
[38] B. Liu, F. F. Lange, *J. Colloid Interface. Sci.* **2006**, *298*, 899.
[39] E. Bormashenko, R. Grynyov, G. Chaniel, H. Taitelbaum, Y. Bormashenko, *Appl. Surf. Sci.* **2013**, *270*, 98.
[40] E. So, M. C. Demirel, K. J. Whal, *J. Phys. D: Appl. Phys.* **2010**, *43*, 045403.
[41] F. Saffih, C. Con, A. Alshammari, M. Yavuz, B. Cui, *J. Vac. Sci. Technol., B* **2014**, *32*, 6.
[42] V. Kondrashov, J. Rühe, *Langmuir* **2014**, *30*, 4342.
[43] H. Jansen, M. de Boer, R. Legtenberg, M. Elwenspoek, *J. Micromech. Microeng.* **1995**, *5*, 115.
[44] K. Rykaczewski, A. T. Paxson, S. Anand, X. Chen, Z. Wang, K. K. Varanasi, *Langmuir* **2013**, *29*, 3.
[45] G. Sun, T. Gao, X. Zhao, H. Zhang, *J. Micromech. Microeng.* **2010**, *20*, 7.
[46] L. X. Yang, Y. M. Chao, L. Jia, C. B. Li, *Appl. Therm. Eng.* **2016**, *99*, 253.

4.2 Effect of monolayer and microstructures on wettability (Paper 6)

It has been assumed that wettability can be determined by the roughness and chemical properties of the surface. The roughness of the surface can be adjusted by microstructures, whereas the chemical properties of the surface can be changed by applying a monolayer or replacing the material. However, the question of which of the two is the dominant contributor for deciding wettability has not been clarified. In **Paper 6**, the biomimetic structures fabricated on silicon are modified by applying a silane monolayer and the surface topography is replicated in polydimethylsiloxane (PDMS) to compare the effect of different materials with the same geometrical structure. This allowed to vary the surface chemistry and topography independently. It is observed that the apparent contact angle in the hydrophobic state is determined by the microstructures despite the monolayer or surface material. The main results is that the geometric aspect of the surface plays a major role to decide apparent contact angle in Cassie-Baxter state when the apparent contact angle for the reference surface is above a given threshold.

Paper 6

Can the wettability be transferred while the topography is replicated?: Bioinspired conical microstructures from silicon to PDMS

Park, I. W., Ribe. J. M., Fernandino, M., and Dorao, C. A.

Can the wettability be transferred while the topography is replicated?: Bioinspired conical microstructures from silicon to PDMS

Il Woong Park, Jonas M. Ribe, Maria Fernandino, and Carlos A. Dorao*

Kolbjørn Hejes v1b, 7491, Trondheim, Norway

E-mail: carlos.dorao@ntnu.no

Abstract

The development of self-cleaning surfaces has motived a vast amount of research due to its potential in scientific and industrial applications such as solar panels and anti-icing. A possible route for achieving a self-cleaning surface is to coat a smooth surface with a monolayer which can control the wettability but is limited for achieving superhydrophobicity. Another possibility is to add microstructures to the surface for controlling the wettability however it could be complicated and expensive for applications requiring large surfaces. In this work, polydimethylsiloxane (PDMS) which can replicate the topography is considered as a material for overcoming the previously discussed drawbacks. Conical microstructures which show self-cleaning properties in silicon are replicated in PDMS. It is observed that the wettability can be transferred while the topography is replicated in the Cassie-Baxter state. Here we show that both the microstructures and the self-cleaning properties (apparent contact angle > 170^{o}, tilting angle < 5^{o}) are transferred to PDMS from the silicon master. Such surfaces should allow for controlled wettability and transferability.

1. Introduction

Controlling the wettability of a surface has been of great interest due to a large number of applications [1–4]. For example, superhydrophobic surfaces which can be defined by greater than 150 degrees of apparent contact angle has been considered for antifogging [5–6], anticorrosion [7–8], antifouling [9], antiicing [10-11], drag reduction [12], antibacterial [13–14], energy harvesting [15–16] and condensation [17–18]. Especially, the lotus effect has been extensively studied for the self-cleaning [19–24] which is characterized by a high apparent contact angle and a low contact angle hysteresis or a tilting angle. Several research groups have attempted to mimic these properties by creating the artificial self-cleaning surfaces [19–22]. Feng et al. achieved a high apparent contact angle (166 degrees) and a low tilting angle (about 3 degrees) by fabricating aligned carbon nanotubes. [19]. However, some challenges remain in terms of the optimization of the artificially textured surface for controlling and understanding the wettability [25].

In order to control the wettability, microstructured surfaces with well-defined parameters have been studied by us and others [21-23]. In particular, we have shown that the apparent contact angle and contact angle hysteresis is directly dependent on the height and center-to-center distance for the conical microstructures [21]. Frankiewicz et al. showed how superhydrophobic surfaces can be obtained by adjusting the roughness in three tiers [22]. It has been observed that the number of the tiers of roughness can determine the wettability by Frankiewicz et al. Liu et al. showed that the surface becomes super repellent against the liquid in low surface tension by texturing doubly reentrant structure [23]. However, the microstructures in two or three tiers could have difficulties when they are applied to a large area in terms of fabrication. Moreover, the fabrication of such structures will be relatively expensive due to the inherent complexity of the process limiting the potential for industrial applications.

A relatively simple and inexpensive method for obtaining superhydrophobic surfaces consists of applying a hydrophobic coating to the target substrate. For example, silanization treatments have been used for controlling the wettability [26–27]. Fadeev and McCarthy observed that a planar silicon wafer will be hydrophobic (around 110 degrees of apparent contact angle) after Octadecyltrichlorosilane self-assembled monolayer coating [26]. Zimmermann et al. reported that the apparent contact angle increased to 165 degrees with the same silane coating when the silicon was structured with nanofilaments [27]. Silanization has also been applied to bioinspired surfaces for obtaining superhydrophobicity in previous studies [19–20]. However, there is a limitation of the apparent contact angle. An apparent contact angle higher than 150 degrees has not been observed when the silanization process is applied to a smooth surface [26–27]. On the other hand, Chen et al. reported that the cone-like structures can present a robust and easy-repairable superhydrophobic surface by thermal spraying [28]. It was reported that the structures can be fabricated by plasma spray deposition using titania on the shielding plate of stainless steel mesh. As the following step, composites of polytetrafluoroethylene and nano-copper were deposited by flame spray over the titania coating. 153 degrees of the apparent contact angle and 2 degrees of the sliding angle were reported. However, thermal spray coating can be limited by the operating temperature if the substrate is not applicable for such the severe condition.

In order to overcome the drawbacks of the microtextured surface and coating for the superhydrophobicity, polydimethylsiloxane (PDMS) could be one of the solutions for a simple fabrication for the superhydrophobic surface. PDMS replication has been well studied in applications such as superhydrophobic surface, lab-on-a-chip and electronics [29–31]. Considering the replication process, it could be beneficial if the structures can be easily peeled after the molding process. The cone shape could be a proper feature due to its structural stability against the pulling

force. In this work, the replicating of conical microstructure on silicon [21] on PDMS is shown as an alternative to transferring the self-cleaning property.

2. Results and Discussion

Figure 1 shows SEM images of the fabricated samples. Truncated cones with photoresist (TC_PR) and hierarchical cones with photoresist (HC_PR) were fabricated by a combined photolithography and dry etching process [21]. TC_PR and HC_PR samples were treated with oxygen plasma in order to remove the photoresist. After stripping the photoresist, the samples are named cleaned truncated cones (TC_C) and cleaned hierarchical cones (HC_C). The cleaned samples are functionalized with a monolayer of silane and named silanized truncated cones (TC_S) and silanized hierarchical cones (HC_S). TC_S was replicated into PDMS and named truncated cones in PDMS (TC_PDMS). The cleaned hierarchical cones were not replicated into the PDMS due to the fragility of the high aspect ratio structures on. The fabrication is described in detail in the experimental section.

Figure 2 shows the apparent contact angle for the TC_PR, TC_C, TC_S, and TC_PDMS and contact angle hysteresis for the TC_PR, TC_S, and TC_ PDMS. When the center-to-center distance becomes high (>150 μm), the apparent contact angle is no longer dependent on the center-to-center distance. In this region, the apparent contact angle is increased by ~50 degrees when the sample is silanized compared with the case with photoresist. The apparent contact angle increases by another ~10 degrees when the sample is replicated into PDMS. This could imply that the apparent contact angle is determined by the wettability of the bottom surface between the microstructures when the center-to-center distance is high. The apparent contact angles for the reference surfaces which are representing the bottom surface between the microstructures were

measured around 56, 105, 115 degrees for TC_PR, TC_S, and TC_ PDMS, respectively. This shows that the apparent contact angle approaches the reference surface when the density of microstructures is small because of the high center-to-center distance.

Wetting transitions corresponding to the breakdown of the superhydrophobic state are observed when the center-to-center distance is increased for TC_PR, TC_S, and TC_ PDMS. The transition for TC_PR and TC_S is abrupt compared to TC_ PDMS. Furthermore, the conical microstructures in PDMS show a broader range of center-to-center distances where a superhydrophobic state can be fabricated compared with in silicon. This could be due to a difference in mechanical properties between solid matter (TC_PR and TC_S, silicon and photoresist) and soft matter (TC_ PDMS, PDMS). The effect might be attributed to the characteristics of the soft matter which might deform in the presence of the droplet. Further study is required to identify the differing trend of the wetting transition.

For conical microstructures with low center-to-center distance (<100 μm), the apparent contact angle for TC_C is zero while the other three samples have a high apparent contact angle. A zero contact angle for TC_C could be explained by the wettability of the top surface of the conical microstructures after removing the photoresist. After the cleaning process, the top surface of the conical microstructure become close to the polished side of the silicon wafer which gives an apparent contact angle around 20 degrees. It might imply that the wettability of the top surface plays a role to decide the wettability of the structured surface. This shows that the surface chemistry can prevent a superhydrophobic state even when the geometric parameter is optimized. However, a high apparent contact angle is observed for the samples TC_PR, TC_S, and TC_ PDMS with low center-to-center distance. This suggests that the center-to-center distance is dominant for determining the apparent contact angle when the apparent contact angle of the top surface between the microstructures are higher than a certain value. When comparing TC_PR, TC_S and TC_

PDMS, it is evident that the superhydrophobic properties of the Si master are transferred to PDMS in the replication process.

For the Cassie-Baxter state, the Cassie-Baxter model can be considered to predict the apparent contact angle when the droplet is on top of the structures containing trapped air in the pores between the solid surfaces [1]. In this model, the apparent contact angle can be presented by the apparent contact angle of the reference surface and the solid fraction as:

$$cos\theta_{CB} = -1 + f_{SA}(cos\theta_{REF} + 1) \quad (1)$$

where θ_{CB} is the apparent contact angle for the Cassie-Baxter model, f_{SA} is the solid fraction and θ_{REF} is the apparent contact angle for the reference surface. The cosine of the apparent contact angle for the Cassie-Baxter model can be compared with the cosine of the apparent contact angle from the measurement as shown in **Figure 3**. The solid fraction was calculated by considering the diameter of the top surface of cones and the center-to-center distance between cones. For y-axis, measured apparent contact angle ($\theta_{Experiment}$) between 15 and 60 μm of the center-to-center distance for the samples TC_PR, TC_S, and TC_ PDMS in Figure 2 was considered. For x-axis, the cosine of the apparent contact angle for the Cassie-Baxter state was obtained from the equation (1). For the red square, measured apparent contact angles for the reference surfaces which were described in above were considered. However, for the blue triangle, the effect of the apparent contact angle of the reference surface was ignored by considering a constant apparent contact angle for all case. Comparing the cosine of the measured apparent contact angle, the cosine of the apparent contact angle for the Cassie-Baxter model with measured apparent contact angle for the reference surface can be more inaccurate than that for the Cassie-Baxter model with the constant apparent contact angle of the reference surface. This can be a disproof for the hypothesis of the Cassie-Baxter state which is the area weighted average of the cosine of the apparent contact angle for the solid and liquid for the given case. In other words, the solid fraction can be considered as the main parameter

for deciding the apparent contact angle for the Cassie-Baxter state. It should be mentioned that the limitation of the model such as the shape of the structures, volume of the droplet and external forces have been already reported in the previous studies [32].

The contact angle hysteresis is decreased with increasing center-to-center distance for the three samples (TC_PR, TC_S, and TC_ PDMS). After decreasing, the contact angle hysteresis suddenly increases with increasing center-to-center distance. Therefore it is possible to consider that there are optimal geometric parameters for obtaining the self-cleaning surface which requires a high apparent contact angle with a low contact angle hysteresis.

In Figure 4, the apparent contact angle for HC_PR and HC_S and contact angle hysteresis for HC_PR, HC_C, and HC_S are presented. For the HC_C, zero apparent contact angle is observed similar to TC_C, respectively. The apparent contact angles are higher than 150 degrees for all center-to-center distances in case of the HC_S. Similar to TC_PR and TC_S, HC_PR shows a drastic drop in the apparent contact angle as the center-to-center distance increases from 40 to 50 μm, implying a breakdown of the superhydrophobic state.

For the HC_PR and HC_S, the apparent contact angle is increasing and the contact angle hysteresis is decreasing with increasing center-to-center distance in the low center-to-center distance region. However, the apparent contact angle and contact angle hysteresis converge in the high center-to-center distance region. For the high center-to-center distance region, it seems like that the microstructures in the second-tier decide the apparent contact angle. There is a difference between the second-tier of the microstructures of HC_PR and HC_S. HC_S has silanized second-tier microstructures while the second-tier microstructure of HC_PR isn't silanized. However, for the low center-to-center distance, it seems like there is no significant effect of the second-tier structures on the apparent contact angle and the contact angle hysteresis when compared with the

truncated conical microstructure which has only single-tier structures. This indicates that a second-tier is not required for obtaining a self-cleaning surface.

Figure 5 shows the tilting angle for TC_S, TC_ PDMS, and HC_S. The three samples gave tilting angles below 5 degrees when adjusting the center-to-center distance of the microstructures. For TC_ PDMS, a tilting angle lower than 2 degrees was observed. This minimum tilting angle is lower than for the other samples. Therefore, the PDMS sample has the advantage of presenting a low tilting angle. Interestingly, the center-to-center distance for the highest apparent contact angle (60 μm) and the lowest tilting angle (80 μm) are different for TC_ PDMS. Where it is possible to achieve a high apparent contact angle with a low tilting angle is shown in terms of the center-to-center distance in this result.

The findings can be summarized for the Cassie-Baxter state, Cassie-Wenzel transition and Wenzel state as follows. For the Cassie-Baxter state, the wettability can be dominantly determined by the topography while the apparent contact angle of the reference surface can be considered as the threshold condition. Even though the drastic Cassie-Wenzel transition was observed in silicon, the sudden change of the apparent contact angle was not observed in PDMS. For the Wenzel state, the wettability can be determined by the chemical aspect which can decide the apparent contact angle of the reference surface while the surface topography plays no significant role.

For the application, the self-cleaning property is given by a high apparent contact angle, low contact angle hysteresis, and low tilting angle. A structured silicon surface expressing these properties can be replicated in PDMS using soft lithography and obtain similar self-cleaning properties. For the conical microstructures discussed here, the PDMS surface presents a broader range of center-to-center distances where the self-cleaning property is obtained when compared with the silicon surface it was replicated from.

3. Potential Application

The potential application of replicated micro-cones are the following:

- The hierarchical structures are not necessary for obtaining a superhydrophobic condition if the microstructure in single-tier is optimized.
- The self-cleaning property could be transferred by replicating the microstructures from silicon to PDMS.
- The conical microstructures in PDMS have the broader range of the center-to-center distance for the self-cleaning property compared with the surface in silicone.

The conical microstructures in single-tier were replicated as shown in Figure 6. It has an advantage in the peeling process for PDMS replication. This is because the conical shape has structural stability against the pooling force and the microstructure in the single-tier has a smaller interfacial area which causes the pooling force compared with hierarchical structures. From this optimized shape regarding the replication process, it seems possible to obtain superhydrophobic surface at low-cost. This is because it can be obtained using only the mixture of PDMS base and PDMS curing agent if the PDMS master is prepared once.

There are also advantages from PDMS itself. They are relatively cheap, replicable, transparent, and bendable. Since they are cheap to replicate it could be beneficial for coating relatively large areas. When we considering the transmission properties of the PDMS in the infrared, it could be beneficial to apply for the PV cell. A bendable characteristic could give the flexibility on the target surfaces. Furthermore, PDMS replication has been considered for fabricating textured surfaces in order to obtain an antifouling property [33] and an anti-reflection property [34].

4. Conclusion

In this study, conical microstructures on silicon were replicated in PDMS using a soft lithography process. The wettability of the silicon and PDMS conical microstructures were examined and the self-cleaning property of the silicon microstructures was found to be transferred to the PDMS. From the results, the dominant influence of the surface topography on the wettability in the Cassie-Baxter state was revealed. As PDMS is a relatively inexpensive material and soft lithography allows for multiple replications, this represents an important step towards low-cost self-cleaning surfaces. Furthermore, the transparency and elasticity of PDMS open up the possibility for novel applications.

5. Experimental Section

5. 1. Fabrication procedure of conical microstructures

The fabrication process is described in **Figure 7** and the dimensions of the microstructures are described in **Table 1**. The process was conducted on a single-side polished Si wafer ({100}, P-type, containing boron as dopant). The sample TC_ PDMS and HC_P were prepared from the previous study [7]. The process for fabricating the sample of TC_ PDMS and HC_P is described in a previous study [7]. The photoresist (SU-8) layer covering the conical microstructures was removed in an oxygen plasma etching process using an ICP-RIE Cryo Reactor (Plasmalab 100 - ICP180, Oxford Instruments). Energy Dispersive Spectroscopy (EDS) was performed in an FEI Helios dual-beam Focused Ion Beam Scanning Electron Microscopes (FIB-SEM). For the samples TC_C and HC_C, EDS did not detect carbon. After removing the photoresist, TC_S and HC_S were silanized in a desiccator using a droplet of Trichloro (1H, 1H, 2H, 2H-perfluorooctyl) silane.

The silicon wafer pattern was replicated in polydimethylsiloxane (PDMS) in a two-step process. First, a replica (dimples) was made from the original Si wafer in PDMS with relatively

high stiffness. Second, this PDMS replica was used as a master for molding the original cone structures. We, therefore, refer to the first replica with dimples as the PDMS master and the second with cones as the PDMS replica.

For the PDMS master, PDMS base and curing agent (Sylgard 184, Dow Corning) were mixed with a weight ratio of 10:1. The mixture was degassed to remove bubbles and cured over the Si master at 65 deg C for 2 h. The PDMS was peeled from the Si wafer and excess PDMS was cut away using a scalpel. The PDMS master was mounted on a glass slide (75 x 50mm, Sigma) by treating the back side of the PDMS with a short oxygen plasma and bonding it to the glass. Finally, the PDMS feature side was activated using a short oxygen plasma treatment and silanized in a desiccator using a droplet of Trichloro (1H, 1H, 2H, 2H-perfluorooctyl) silane, similar to the Si wafer. It should be noted that Trichloro is not needed for the further replication process once the PDMS master is coated.

For the PDMS replicas, PDMS base and curing agent (Sylgard 184, Dow Corning) were mixed with the normal weight ratio 10:1. The mixture was degassed to remove bubbles and poured on top of the PDMS master. A glass slide (75 x 50mm, Sigma) was placed on top of the uncured PDMS and the whole stack was placed in the oven at 65deg C for 2 h. The PDMS replica was peeled manually from the PDMS master using the glass slides.

5. 2. Scanning Electron Microscopes (SEM)

For the SEM image, an FEI Helios dual-beam Focused Ion Beam Scanning Electron Microscopes (FIB-SEM) was used. The stage was tilted 52 degrees for measuring the height of the microstructures. For the TC_ PDMS, a 10 nm gold layer was deposited by evaporation (Custom ATC-2200V, AJA International Inc.) before taking SEM image.

5. 3. Contact angle measurement

The apparent contact angle was measured for every sample. 9.8 μL of distilled water was gently deposited on top of each sample. Advancing and receding contact angles were measured by varying the volume of the droplet between 5 μL and 50 μL. Receding contact angle was measured just before the detachment of the droplet in case of the superhydrophobic condition. The tilting angle was measured by changing the tilted angle of the stage (GNL10/M, Thorlab). 9.8 μL of distilled water droplet was deposited before changing the tilted angle of the stage.

Acknowledgements

The Ph.D. fellowship (Il-Woong Park) financed by the NTNU-SINTEF Gas Technology Centre is gratefully acknowledged. The Research Council of Norway is acknowledged for the support to the Norwegian Micro- and Nano-Fabrication Facility, NorFab, for the fabrication and characterization of samples at the NTNU Nanolab facility.

Author contributions statements

Il Woong Park, Jonas M. Ribe wrote the main manuscript text and Il Woong Park prepared figures 1–7. All authors reviewed the manuscript.

References

[1] Cassie, A. B. D. & Baxter, S. Wettability of porous surfaces. *Trans. Faraday Soc.* **40**, 546–551 (1944).

[2] Wenzel, R. N. Resistance of solid surfaces to wetting by water. *Ind. Eng. Chem.* **28**, 988–994 (1936).

[3] Bormashenko, E. Progress in understanding wetting transitions on rough surfaces. *Adv. Colloid Interface Sci.* **222**, 92–103 (2015).

[4] Young, B. N. Wenzel and Cassie-Baxter equations as the transversality conditions for the variational problem of wetting Bormashenko, Edward. *Colloids Surf. A* 345, 1-3 (2009).

[5] Mouterde, T. et. al. Antifogging abilities of model nanotextures. *Nature materials*, **16**, 658. (2017).

[6] Sun, Z. et. al. Fly-Eye Inspired Superhydrophobic Anti-Fogging Inorganic Nanostructures. *Small*, **10**, 3001-3006. (2014)

[7] Wang, Z. et. al. Researching a highly anti-corrosion superhydrophobic film fabricated on AZ91D magnesium alloy and its anti-bacteria adhesion effect. *Materials Characterization*, **99**, 200-209. (2015).

[8] Isimjan, T. T. et. al. A novel method to prepare superhydrophobic, UV resistance and anti-corrosion steel surface. *Chemical engineering journal*, **210**, 182-187. (2012)

[9] Barish, J. A. and Goddard, J. M. Anti-fouling surface modified stainless steel for food processing. *Food and Bioproducts processing*, **91**, 352-361. (2013).

[10] Tang, Y., Zhang, Q., Zhan, X., & Chen, F. (2015). Superhydrophobic and anti-icing properties at overcooled temperature of a fluorinated hybrid surface prepared via a sol–gel process. Soft Matter, 11(22), 4540-4550.

[11] Wang, N., Xiong, D., Deng, Y., Shi, Y., & Wang, K. (2015). Mechanically robust superhydrophobic steel surface with anti-icing, UV-durability, and corrosion resistance properties. ACS applied materials & interfaces, 7(11), 6260-6272.

[12] McHale, G., Newton, M. I., & Shirtcliffe, N. J. (2010). Immersed superhydrophobic surfaces: Gas exchange, slip and drag reduction properties. Soft Matter, 6(4), 714-719.

[13] Wu, M., Ma, B., Pan, T., Chen, S., & Sun, J. (2016). Silver-nanoparticle-colored cotton fabrics with tunable colors and durable antibacterial and self-healing superhydrophobic properties. Advanced Functional Materials, 26(4), 569-576.

[14] Watson, G. S., Green, D. W., Schwarzkopf, L., Li, X., Cribb, B. W., Myhra, S., & Watson, J. A. (2015). A gecko skin micro/nano structure–A low adhesion, superhydrophobic, anti-wetting, self-cleaning, biocompatible, antibacterial surface. Acta biomaterialia, 21, 109-122.

[15] Choi, D., Lee, S., Park, S. M., Cho, H., Hwang, W., & Kim, D. S. (2015). Energy harvesting model of moving water inside a tubular system and its application of a stick-type compact triboelectric nanogenerator. Nano Research, 8(8), 2481-2491.

[16] Miljkovic, N., Preston, D. J., Enright, R., & Wang, E. N. (2014). Jumping-droplet electrostatic energy harvesting. Applied Physics Letters, 105(1), 013111.

[17] Miljkovic, N., Preston, D. J., Enright, R., & Wang, E. N. (2013). Electric-field-enhanced condensation on superhydrophobic nanostructured surfaces. ACS nano, 7(12), 11043-11054.

[18] Yoon, D., Lee, C., Yun, J., Jeon, W., Cha, B. J., & Baik, S. (2012). Enhanced condensation, agglomeration, and rejection of water vapor by superhydrophobic aligned multiwalled carbon nanotube membranes. ACS nano, 6(7), 5980-5987.

[19] Feng, L. et al. Super-hydrophobic surfaces: from natural to artificial. *Adv. Mater*. **14**, 1857-1860 (2002).

[20] Liu, K et al. Recent developments in bio-inspired special wettability. *Chem. Soc. Rev.* 39, 3240-3255 (2010).

[21] Park, I. W. et al. Wetting State Transitions over Hierarchical Conical Microstructures. *Adv. Mater. Interfaces* **5**, 1701039 (2018).

[22] Frankiewicz, C., & Attinger, D. Texture and wettability of metallic lotus leaves. *Nanoscale* **8**, 3982-3990 (2016).

[23] Liu, T., & Kim, C. J. Turning a surface superrepellent even to completely wetting liquids. *Science* **346**, 1096-1100 (2014).

[24] Blossey, R. Self-cleaning surfaces—virtual realities. *Nat. Mater*. **2**, 301 (2003).

[25] Yan, Y. Y. et al. Mimicking natural superhydrophobic surfaces and grasping the wetting process: A review on recent progress in preparing superhydrophobic surfaces. *Adv. Colloid Interface Sci.* **169**, 80-105 (2011).

[26] Fadeev, A. Y., & McCarthy, T. J. Self-assembly is not the only reaction possible between alkyltrichlorosilanes and surfaces: monomolecular and oligomeric covalently attached layers of dichloro-and trichloroalkylsilanes on silicon. *Langmuir* **16**, 7268-7274 (2000).

[27] Zimmermann, J. et al. Patterned superfunctional surfaces based on a silicone nanofilament coating. *Soft Matter* **4**, 450-452 (2008).

[28] Chen, X., Gong, Y., Li, D., & Li, H. (2016). Robust and easy-repairable superhydrophobic surfaces with multiple length-scale topography constructed by thermal spray route. Colloids and Surfaces A: Physicochemical and Engineering Aspects, 492, 19-25.

[29] Cheng, Q. et al. Janus interface materials: superhydrophobic air/solid interface and superoleophobic water/solid interface inspired by a lotus leaf. *Soft Matter*, **7**, 5948-5951 (2011).

[30] Comina, G. et al. PDMS lab-on-a-chip fabrication using 3D printed templates. *Lab on a Chip* **14**, 424-430 (2014).

[31] Zhang, Y. et. al. Flexible and Highly Sensitive Pressure Sensor Based on Microdome-Patterned PDMS Forming with Assistance of Colloid Self-Assembly and Replica Technique for Wearable Electronics. *ACS Appl. Mater. Interfaces* **9**, 35968-35976 (2017).

[32] Bormashenko, E. Progress in understanding wetting transitions on rough surfaces. *Adv. Colloid Interface Sci.*, **222**, 92-103 (2015).

[33] Chen, Z. et al. Designing environmentally benign modified silica resin coatings with biomimetic textures for antibiofouling. *RSC Advances* **5**, 36874-36881 (2015).

[34] Shin, J. H. et al. Anti-reflection and hydrophobic characteristics of M-PDMS based moth-eye nano-patterns on protection glass of photovoltaic systems. *Prog. Photovolt: Res. Appl*. **19**, 339-344 (2011).

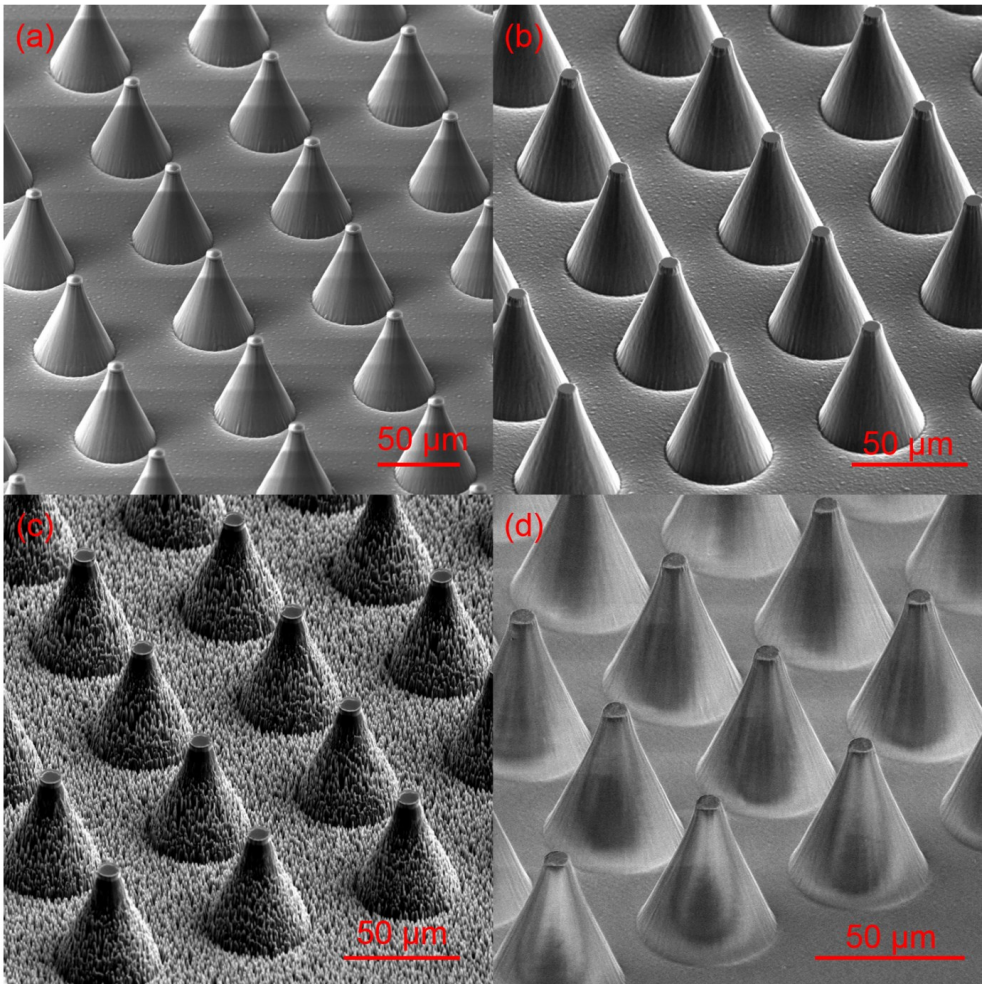

Figure 1. SEM images of micro conical structures. (a) TC_PR (b) TC_C (c) HC_C (d) TC_PDMS

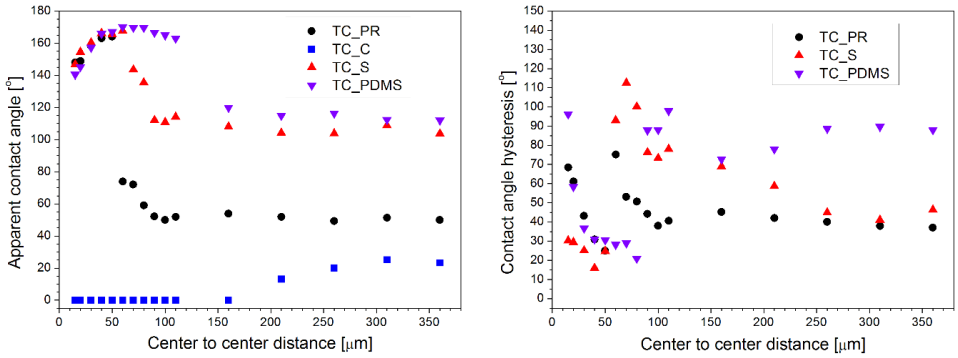

Figure 2. Apparent contact angle and contact angle hysteresis of Truncated Cones (TC)

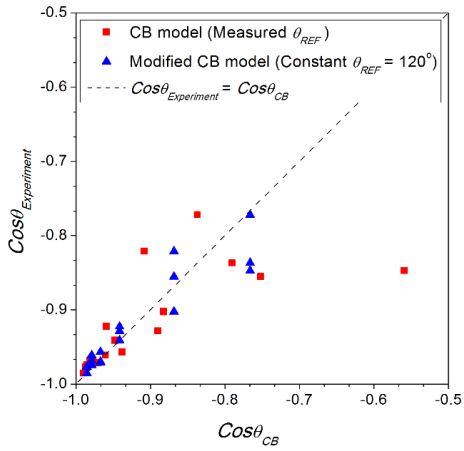

Figure 3. Comparison of the apparent contact angle for the Cassie-Baxter model and the experiment

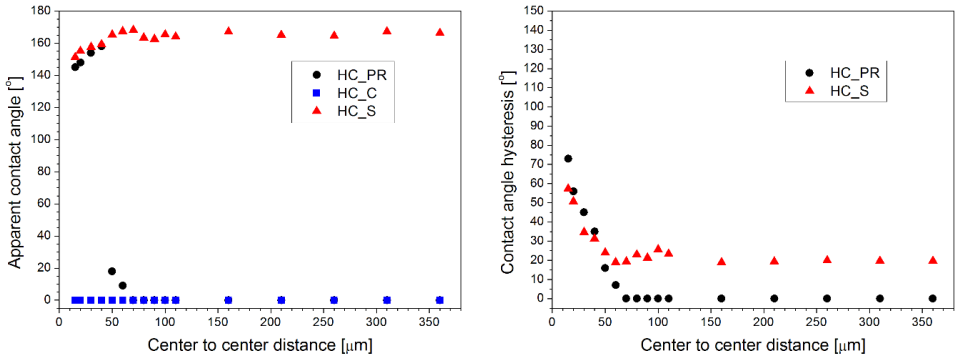

Figure 4. Apparent contact angle and contact angle hysteresis of Hierarchical Cones (HC)

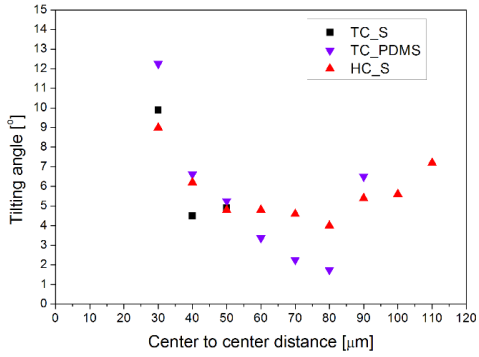

Figure 5. Tilting angle of Truncated Cones (TC) and Hierarchical Cones (HC)

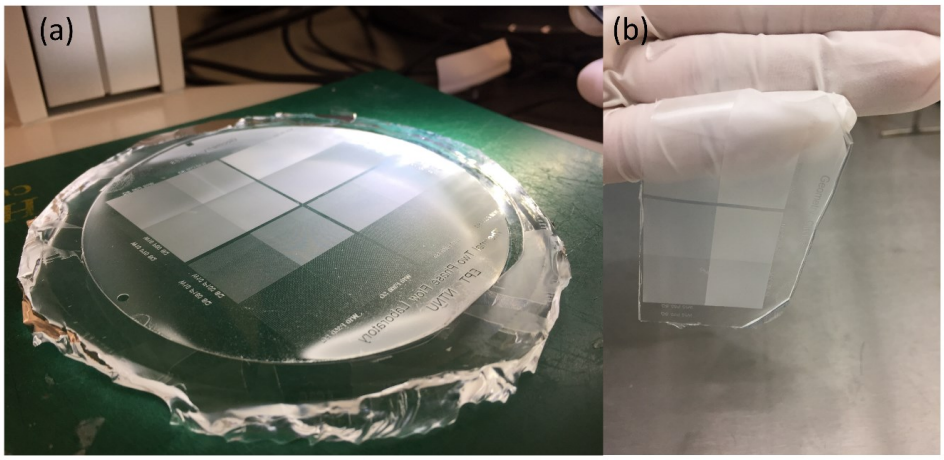

Figure 6. (a) PDMS master (4 inches mask), (b) TC_PDMS

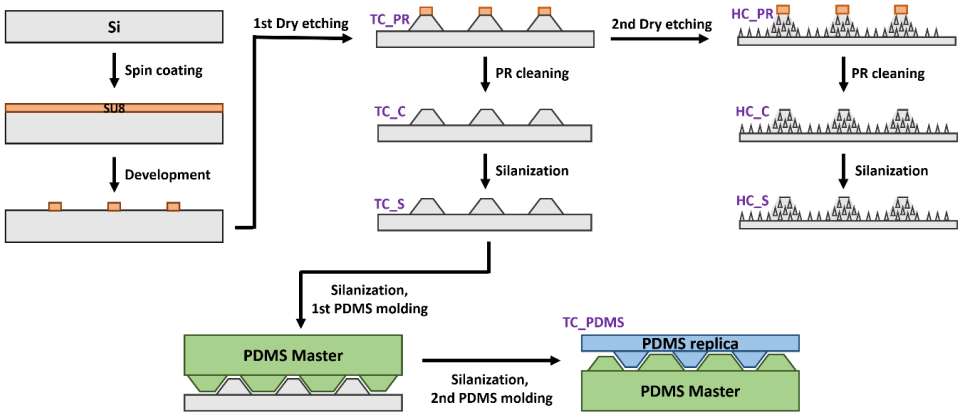

Figure 7. Fabrication process

Table 1. Parameters of the microstructures

	H_T [µm] [g]	H_P [µm] [h]	H_S [µm] [i]	D_T [µm] [j]	D_B [µm] [k]	P [µm] [l]	Substrate	Silanized
TC [a]_PR [b]	55	4	51	9	45	15 – 360	Si, SU8	X
TC_C [c]	51	0	51	9	45	15 – 360	Si	X
TC_S [d]	51	0	51	9	45	15 – 360	Si	O
TC_PDMS [e]	51	0	51	9	45	15 – 360	PDMS	X
HC [f]_PR	58	4	54	9	45	15 – 360	Si, SU8	X
HC_C	54	0	54	9	45	15 – 360	Si	X
HC_S	54	0	54	9	45	15 – 360	Si	O

[a] Truncated Cone; [b] Photoresist; [c] Cleaned; [d] Silanized; [e] Replicated; [h] hierarchical cone; [g] height of truncated cone; [h] height of photoresist; [i] height of silicon; [j] diameter of top surface of truncated cone; [k] diameter of bottom part of conical structure; [l] center-to-center distance.

Chapter 5 Enhancement of heat transfer

5.1 Leidenfrost point on the micro-structured surfaces (Paper 7)

It has been found that the Leidenfrost point (LFP) can be increased with micro or nanotextured surfaces. However, the LFP has been defined differently in previous studies. There are three LFPs: nominal LFP, non-wetting point, and dynamic LFP. Nominal LFP can be described as having the longest droplet evaporation time versus the surface temperature profile. The non-wetting point can be characterized by identifying the surface temperature that exhibits the sudden increase in the evaporation time. Dynamic LFP can be determined graphically. This temperature corresponds to the minimum surface temperature, which allows a droplet to jump on a heated surface.

In order to clarify the difference between the LFPs, an experimental study for measuring the three LFPs in the same micro-textured surface is conducted in **Paper 7**. Micro-textured surfaces consisting of cylindrical pillars were fabricated with different diameter, spacing and height for the Leidenfrost experiments. Results show that approximately 70K differences can occur between the three LFPs over microstructured surfaces, whereas differences in LFPs are negligible in smooth (untreated) surfaces. The main finding in this work is that a microstructured surface affects not only the heat transfer at the macroscale but it also introduces new phenomena like transition film boiling that is not observed on smooth surfaces.

Paper 7

Effect of Micropillar Characteristics on Leidenfrost Temperature of Impacting Droplets

Park, I. W., Fernandino, M., and Dorao, C. A.

In ASME 2016 14th International Conference on Nanochannels, Microchannels, and Minichannels collocated with the ASME 2016 Heat Transfer Summer Conference and the ASME 2016 Fluids Engineering Division Summer Meeting (pp. V001T09A001-V001T09A001). American Society of Mechanical Engineers.

Chapter 6 Conclusion and Future work

6.1 Conclusions

Part I

The occurrence of pressure drop oscillations and superimposed density wave oscillations was experimentally studied. It was observed that superimposed density wave oscillations on pressure drop oscillations occur in the intermediate region of the negative slope of the internal characteristic curve. A pressure drop to mass flux limit cycle was presented for illustrating the interaction between the oscillations.

Superimposed density wave oscillations and pressure drop oscillations were decoupled for identifying their characteristics. Density wave oscillations can be superimposed on pressure drop oscillations when the pressure drop oscillations have a fast rate of change in the mass flux. The amplitude of the mass flux oscillations during density wave oscillations was amplified because of the existence of the compressible volume which is essential for pressure drop oscillations. The level of the compressible volume can affect the profile of the pressure drop oscillations and the latter can trigger the density wave oscillations when the mass flux changes fast enough.

Heat transfer performance during pressure drop oscillations was experimentally studied. No significant deterioration of the time-averaged heat transfer coefficient was observed, contrary to what has been reported in previous studies. It was suggested that the difference between them could be attributed to the possible occurrence of dry-out when the mass flux is low. The characteristics of the heat transfer coefficient under the oscillations cycle were explained by comparing with that for the stationary condition which corresponds to the maximum and minimum mass flux under pressure drop oscillations.

During flow boiling, an experimental study on the deterioration of the heat transfer coefficient in the case of controlled flow oscillations was presented. It was observed that oscillations of the flow can deteriorate the time-averaged heat transfer coefficient, but it depends on the period and amplitude of the oscillations. In particular, deterioration is not noticeable until the period and amplitude reach given thresholds. A dry-out of the wall during the low flow condition was pointed out as the mechanism for the deterioration of the time-averaged heat transfer coefficient.

Part II

Conical microstructures with well-organized geometric parameters were fabricated by photolithography and dry-etching process. Two types of biomimetic microstructures, namely patterned truncated cones and hierarchical conical structures, were fabricated. In total, 96 different samples were fabricated in two structures types, three heights, and 16 spacing between the structures. Wettability from the superhydrophobic state to the superhydrophilic state was observed over the fabricated samples. A drastic wetting transition from Cassie-Baxter to Wenzel state was observed for both types of structures. It can be noted that the transition was achieved by the geometric parameters without external excitation.

Conical microstructures on silicon were replicated in polydimethylsiloxane (PDMS) using a soft lithography process. Wettability for both microstructures in silicon and PDMS were examined. It was observed that the self-cleaning property of the silicon microstructures can be transferred to the PDMS. In the results, the chemical aspect of the surface contributes to the apparent contact angle in Wenzel state, while the geometrical aspect of the microstructures is dominant for deciding the apparent contact angle in the Cassie–Baxter state. Furthermore, the fabrication of the replicated surface in PDMS can be considered as a flexible low-cost self-cleaning surface for various applications.

Effects of the width, height, and spacing of microstructures on Ledienfrost temperatures were investigated experimentally. Dynamic Leidenfrorst point and nominal Leidenfrost point were obtained in the condition of the surface with microstructures. It was observed that the

LFP can be increased or decreased by changing the parameters of the microstructures. Up to 70K difference between the different definitions of the LFP was observed depending on the geometric parameters of the microstructures, while the untreated smooth surface had less than 10K difference between the different LFPs. The transition film boiling region was observed on the surface with microstructures. It was characterized by visual observation of the droplet dynamics from high-speed images or the gradual increase of the droplet lifetime.

6.2 Major Contributions of this study

- The conditions for the occurrence of pure pressure drop oscillations has been observed a systematic experimental study.
- The mechanisms triggering superimposed density wave oscillations are identified by decoupling the effect of the expansion tank and the rate of change in the mass flux.
- This thesis shows that under certain given conditions, flow oscillations are not detrimental to the heat transfer coefficient, as it has commonly suggested in the literature.
- A fabrication process for bioinspired conical microstructures with control of the surface geometrical parameters is successfully implemented even though dry-etching process requires very sensitive control of the variables.
- Control of the wetting state including the Cassie-Wenzel transition is achieved without external excitation.
- It is observed that the wettability is determined by the geometry of the conical microstructures and can thus be replicated into a different substrate. This can be applied to the design of flexible low-cost self-cleaning surfaces.
- Differences between the LFPs which can be broadened for the case of micro-engineered surfaces as compared with smooth surfaces are reported. This finding can be helpful for understanding the discrepancies from previous studies.

6.3 Recommendations for future work

The recommendations for the future works are presented with the keywords.

- **Effect of the wall inertia.** Only a few studies have discussed the importance of the wall inertia and its impact on the instability. As shown in this work, the wall inertia plays an important role in heat transfer deterioration. Feedback from the deterioration of the heat transfer due to the wall inertia during two-phase flow instabilities could provide valuable insights on this topic.
- **Model for predicting heat-transfer coefficient deterioration.** This study presented the experimental data of heat transfer with varying period and amplitude. This could be crucial for deriving the model for the heat transfer coefficient under an oscillatory flow. Furthermore, the influence of the deteriorated heat transfer to the characteristics of the two-phase flow instabilities should be considered.
- **Image of three-phase line on the microstructures.** It would be interesting to obtain high magnification images of the three-phase line on the microstructure using the confocal microscope. Consequently, the fabrication of the structure in transparent materials is recommended. Moreover, the wettability of the droplet, which is containing the fluorescents, should be identified.
- **Models for Leidenfrost point for microstructures.** A considerable amount of studies on Leidenfrost point for the surface with microstructures are available in open literature. It would be possible to find a correlation between the existing experimental results to identify the dominant contribution on Leidenfrost point. However, these studies have different measurements concerning the surface temperature, the characteristics of the droplet, including the size and the velocity, and different definition of the Leidenfrost point, which pose critical difficulties to the calculations.

References

[1] Pacio, J. C., & Dorao, C. A. (2011). A review on heat exchanger thermal hydraulic models for cryogenic applications. *Cryogenics*, 51(7), 366-379.

[2] Mayinger, F. (1997). Status of thermohydraulic research in nuclear safety and new challenges. *In Eight International Topical Meeting on Nuclear Reactor Thermal-Hydraulics*, Kyoto, Japan (pp. 1508-1518).

[3] Zhang, T., Wen, J. T., Peles, Y., Catano, J., Zhou, R., & Jensen, M. K. (2011). Two-phase refrigerant flow instability analysis and active control in transient electronics cooling systems. *International Journal of Multiphase Flow*, 37(1), 84-97.

[4] Boure, J. A., Bergles, A. E., & Tong, L. S. (1973). Review of two-phase flow instability. *Nuclear Engineering and Design*, 25(2), 165-192.

[5] Tadrist, L. (2007). Review on two-phase flow instabilities in narrow spaces. *International Journal of Heat and fluid flow*, 28(1), 54-62.

[6] Kakac, S., & Bon, B. (2008). A review of two-phase flow dynamic instabilities in tube boiling systems. *International Journal of Heat and Mass Transfer*, 51(3-4), 399-433.

[7] Liang, N., Shao, S., Xu, H., & Tian, C. (2010). Instability of refrigeration system–*A review. Energy conversion and management*, 51(11), 2169-2178.

[8] Chiapero, E. M., Fernandino, M., & Dorao, C. A. (2012). Review on pressure drop oscillations in boiling systems. *Nuclear Engineering and Design*, 250, 436-447.

[9] Yüncü, H., Yildirim, O. T., & Kakac, S. (1991). Two-phase flow instabilities in a horizontal single boiling channel. *Applied Scientific Research*, 48(1), 83-104.

[10] Çomaklı, Ö., Karslı, S., & Yılmaz, M. (2002). Experimental investigation of two phase flow instabilities in a horizontal in-tube boiling system. *Energy Conversion and Management*, 43(2), 249-268.

[11] Ding, Y., Kakac, S., & Chen, X. J. (1995). Dynamic instabilities of boiling two-phase flow in a single horizontal channel. *Experimental Thermal and Fluid Science*, 11(4), 327-342.

[12] Liu, H. T., & Kakac, S. (1991). An experimental investigation of thermally induced flow instabilities in a convective boiling upflow system. *Waerme-und Stoffuebertragung*, 26(6), 365-376.

[13] Menteş, A., Kakaç, S., Veziroğlu, T. N., & Zhang, H. Y. (1989). Effect of inlet subcooling on two-phase flow oscillations in a vertical boiling channel. *Wärme-und Stoffübertragung*, 24(1), 25-36.

[14] Yin, J., Lahey Jr, R. T., Podowski, M. Z., & Jensen, M. K. (2006). An Analysis of Interacting Instability Modes. *Multiphase Science and Technology*, 18(4).

[15] Sørum, M., & Dorao, C. A. (2015). Experimental study of the heat transfer coefficient deterioration during Density Wave Oscillations. *Chemical Engineering Science*, 132, 178-185.

[16] Guo, L. J., Feng, Z. P., & Chen, X. J. (2002). Transient convective heat transfer of steam–water two-phase flow in a helical tube under pressure drop type oscillations. *International journal of heat and mass transfer*, 45(3), 533-542.

[17] Chen, C. A., Lin, T. F., Yan, W. M., & Amani, M. (2018). Time periodic evaporation heat transfer of R-134a in a narrow annular duct due to mass flow rate oscillation. *International Journal of Heat and Mass Transfer*, 118, 154-164.

[18] Wang, S. L., Chen, C. A., & Lin, T. F. (2013). Oscillatory subcooled flow boiling heat transfer of R-134a and associated bubble characteristics in a narrow annular duct due to flow rate oscillation. *International Journal of Heat and Mass Transfer*, 63, 255-267.

[19] Chen, C. A., Chang, W. R., & Lin, T. F. (2010). Time periodic flow boiling heat transfer of R-134a and associated bubble characteristics in a narrow annular duct due to flow rate oscillation. *International Journal of Heat and Mass Transfer*, 53(19-20), 3593-3606.

[20] Jaikumar, A., & Kandlikar, S. G. (2015). Enhanced pool boiling heat transfer mechanisms for selectively sintered open microchannels. *International Journal of Heat and Mass Transfer*, 88, 652-661.

[21] Farokhnia, N., Sajadi, S. M., Irajizad, P., & Ghasemi, H. (2017). Decoupled Hierarchical Structures for Suppression of Leidenfrost Phenomenon. *Langmuir*, 33(10), 2541-2550.

[22] Woodcock, C., Yu, X., Plawsky, J., & Peles, Y. (2015). Piranha Pin Fin (PPF)—Advanced flow boiling microstructures with low surface tension dielectric fluids. *International Journal of Heat and Mass Transfer*, 90, 591-604

[23] Bigham, S., & Moghaddam, S. (2015). Role of bubble growth dynamics on microscale heat transfer events in microchannel flow boiling process. *Applied Physics Letters*, 107(24), 244103.

[24] Kandlikar, S. G. (2013). Controlling bubble motion over heated surface through evaporation momentum force to enhance pool boiling heat transfer. *Applied Physics Letters*, 102(5), 051611.

[25] Kim, H., Truong, B., Buongiorno, J., & Hu, L. W. (2011). On the effect of surface roughness height, wettability, and nanoporosity on Leidenfrost phenomena. *Applied Physics Letters*, 98(8), 083121

[26] Kwon, H. M., Bird, J. C., & Varanasi, K. K. (2013). Increasing Leidenfrost point using micro-nano hierarchical surface structures. *Applied Physics Letters*, 103(20), 201601.

[27] Tran, T., Staat, H. J., Susarrey-Arce, A., Foertsch, T. C., van Houselt, A., Gardeniers, H. J., ... & Sun, C. (2013). Droplet impact on superheated micro-structured surfaces. *Soft Matter*, 9(12), 3272-3282.

[28] Kim, D. E., Yu, D. I., Jerng, D. W., Kim, M. H., & Ahn, H. S. (2015). Review of boiling heat transfer enhancement on micro/nanostructured surfaces. *Experimental Thermal and Fluid Science*, 66, 173-196.

[29] Kandlikar, S. G. (2001). A theoretical model to predict pool boiling CHF incorporating effects of contact angle and orientation. *Journal of Heat Transfer*, 123(6), 1071-1079.

[30] Betz, A. R., Xu, J., Qiu, H., & Attinger, D. (2010). Do surfaces with mixed hydrophilic and hydrophobic areas enhance pool boiling?. *Applied Physics Letters*, 97(14), 141909.

[31] Betz, A. R., Jenkins, J., & Attinger, D. (2013). Boiling heat transfer on superhydrophilic, superhydrophobic, and superbiphilic surfaces. *International Journal of Heat and Mass Transfer*, 57(2), 733-741.

[32] Frankiewicz, C., & Attinger, D. (2017). On Temporal Biphilicity: Definition, Relevance, and Technical Implementation in Boiling Heat Transfer. *Journal of Heat Transfer*, 139(11), 111511.

[33] Lei, W., Jia, Z. H., He, J. C., Cai, T. M., & Wang, G. (2014). Vibration-induced Wenzel-Cassie wetting transition on microstructured hydrophobic surfaces. *Applied Physics Letters*, 104(18), 181601.

[34] Liu, G., Fu, L., Rode, A. V., & Craig, V. S. (2011). Water droplet motion control on superhydrophobic surfaces: exploiting the Wenzel-to-Cassie transition. *Langmuir*, 27(6), 2595-2600.

[35] Kumari, N., & Garimella, S. V. (2011). Electrowetting-induced dewetting transitions on superhydrophobic surfaces. *Langmuir*, 27(17), 10342-10346.

[36] Liu, T., & Kim, CJ. (2014). Turning a surface superrepellent even to completely wetting liquids. *Science*, 346(6213), 1096-1100.

[37] Chu, D., Nemoto, A., & Ito, H. (2014). Enhancement of dynamic wetting properties by direct fabrication on robust micro–micro hierarchical polymer surfaces. *Applied Surface Science*, 300, 117-123.

[38] Bellanger, H., Darmanin, T., Taffin de Givenchy, E., & Guittard, F. (2014). Chemical and physical pathways for the preparation of superoleophobic surfaces and related wetting theories. *Chemical reviews*, 114(5), 2694-2716.

[39] Ems, H., & Ndao, S. (2015). Microstructure-alone induced transition from hydrophilic to hydrophobic wetting state on silicon. *Applied Surface Science*, 339, 137-143.

[40] Koch, K., & Barthlott, W. (2009). Superhydrophobic and superhydrophilic plant surfaces: an inspiration for biomimetic materials. Philosophical Transactions of the Royal Society of London A: Mathematical, *Physical and Engineering Sciences*, 367(1893), 1487-1509.

[41] Uddin, R. (1994). On density-wave oscillations in two-phase flows. *International journal of multiphase flow*, 20(4), 721-737.

[42] Dorao, C. A. (2015). Effect of inlet pressure and temperature on density wave oscillations in a horizontal channel. *Chemical engineering science*, 134, 767-773.

[43] Saha, P., & Zuber, N. (1974). *Point of net vapor generation and vapor void fraction in subcooled boiling.* United States: Scripta Book Co.

[44] Guo, Y., Huang, J., Xia, G., & Zeng, H. (2010). Experiment investigation on two-phase flow instability in a parallel twin-channel system. *Annals of Nuclear Energy*, 37(10), 1281-1289.

[45] Strømsvåg, D. (2011). Fundamental mechanisms of density wave oscillations and the effect of subcooling (Master's thesis, Institutt for energi-og prosessteknikk).

[46] Padki, M. M., Palmer, K., Kakac, S., & Veziroğlu, T. N. (1992). Bifurcation analysis of pressure-drop oscillations and the Ledinegg instability. *International journal of heat and mass transfer*, 35(2), 525-532.

[47] Collier, J. G., & Thome, J. R. (1994). *Convective boiling and condensation*. Clarendon Press.

[48] Chen, J. C. (1966). Correlation for boiling heat transfer to saturated fluids in convective flow. *Industrial & engineering chemistry process design and development*, 5(3), 322-329.

[49] Gungor, K. E., & Winterton, R. H. S. (1986). A general correlation for flow boiling in tubes and annuli. *International Journal of Heat and Mass Transfer*, 29(3), 351-358.

[50] Shah, M. M. (1982). Chart correlation for saturated boiling heat transfer: equations and further study. *ASHRAE Trans.*;(United States), 88(CONF-820112-).

[51] Kandlikar, S. G. (1990). A general correlation for saturated two-phase flow boiling heat transfer inside horizontal and vertical tubes. *Journal of heat transfer*, 112(1), 219-228.

[52] Kattan, N., Thome, J. R., & Favrat, D. (1998). Flow boiling in horizontal tubes: part 3—development of a new heat transfer model based on flow pattern. *Journal of Heat Transfer*, 120(1), 156-165.

[53] Kim, S. M., & Mudawar, I. (2014). Review of databases and predictive methods for heat transfer in condensing and boiling mini/micro-channel flows. *International Journal of Heat and Mass Transfer*, 77, 627-652.

[54] Dorao, C. A., Drewes, S., & Fernandino, M. (2018). Can the heat transfer coefficients for single-phase flow and for convective flow boiling be equivalent?. *Applied Physics Letters*, 112(6), 064101.

[55] Young, T. (1805). III. An essay on the cohesion of fluids. *Philosophical transactions of the royal society of London*, 95, 65-87.

[56] Cassie, A. B. D., & Baxter, S. (1944). Wettability of porous surfaces. *Transactions of the Faraday society*, 40, 546-551.

[57] Wenzel, R. N. (1936). Resistance of solid surfaces to wetting by water. *Industrial & Engineering Chemistry*, 28(8), 988-994.

[58] Bormashenko, E. (2015). Progress in understanding wetting transitions on rough surfaces. *Advances in colloid and interface science*, 222, 92-103.

[59] Zhang, X., Zhang, J., Ren, Z., Li, X., Zhang, X., Zhu, D & Yang, B. (2009). Morphology and wettability control of silicon cone arrays using colloidal lithography. *Langmuir*, 25(13), 7375-7382.

[60] Chen, X., Patel, R. S., Weibel, J. A., & Garimella, S. V. (2016). Coalescence-induced jumping of multiple condensate droplets on hierarchical superhydrophobic surfaces. *Scientific reports*, 6, 18649.

[61] Kondrashov, V., & Rühe, J. (2014). Microcones and nanograss: toward mechanically robust superhydrophobic surfaces. *Langmuir*, 30(15), 4342-4350.

[62] Chen, X., Gong, Y., Li, D., & Li, H. (2016). Robust and easy-repairable superhydrophobic surfaces with multiple length-scale topography constructed by thermal spray route. *Colloids and Surfaces A: Physicochemical and Engineering Aspects*, 492, 19-25.

[63] Arce, A. S. (2014). *Switching activation barriers: new insights in E-field driven processes at the interface: perspectives in physical chemistry and catalysis.*

[64] Xue, P., Nan, J., Wang, T., Wang, S., Ye, S., Zhang, J., ... & Yang, B. (2017). Ordered Micro/Nanostructures with Geometric Gradient: From Integrated Wettability "Library" to Anisotropic Wetting Surface. *Small*, 13(4).

[65] Kandlikar, S. G. (2003, January). Heat transfer mechanisms during flow boiling in microchannels. *In ASME 2003 1st International Conference on Microchannels and Minichannels* (pp. 33-46). American Society of Mechanical Engineers.

[66] Farokhnia, N., Sajadi, S. M., Irajizad, P., & Ghasemi, H. (2017). Decoupled Hierarchical Structures for Suppression of Leidenfrost Phenomenon. *Langmuir,* 33(10), 2541-2550.

[67] Tran, T., Staat, H. J., Susarrey-Arce, A., Foertsch, T. C., van Houselt, A., Gardeniers, H. J., ... & Sun, C. (2013). Droplet impact on superheated micro-structured surfaces. *Soft Matter*, 9(12), 3272-3282.

[68] Tran, T., Staat, H. J., Prosperetti, A., Sun, C., & Lohse, D. (2012). Drop impact on superheated surfaces. *Physical review letters*, 108(3), 036101.

Appendix A Fabrication of the micro-engineered surface

A.1 Dry-etching parameters for conical microstructures

The cryogenic reactive ion etching was conducted in an ICP-RIE Cryo Reactor (Plasmalab 100 – ICP180, Oxford Instruments, UK). This is the most sensitive step for fabricating the bioinspired conical microstructures in chapter 4.1.

The main challenge of the dry-etching is that there are many control variables which affect the profile of the microstructures. The variables are cryogenic temperature, pressure, the flow of Sulfur hexafluoride, the flow of Oxygen, capacitive coupled plasma radio frequency (RF) power, inductively coupled plasma (ICP) power and time. Cryogenic temperature affects the amount of the reaction of the etching gas. Pressure decides the amount of the etching gas in the chamber. Both temperature and pressure can affect the etching selectivity for silicon and mask material, etching rate, sidewall roughness and profile or the sidewall. A proportion of the etching gas can affect the profiles of the sidewall due to the amount of the additional gas for sidewall passivation. Simply, the ICP power affects the number of the plasma and the RF power determine the momentum for driving the ion from the plasma to the surface.

Figure A.1 presents the effect of the RF power to the roughness of the upper part of the sidewall. Other variables were selected as 600 Watts of ICP power, 11 sccm of O_2 flow, 60 sccm of SF_6 flow, 10 mTorr of pressure, –110ºC of the cryogenic temperature and 10 minutes of the etching times. It is possible to observe more damage on the upper part of the sidewall when the RF power is higher. It could imply that deducted parameter of the proportion of the etching gasses for smooth sidewall profile could not be valid when the RF power is varied.

Figure A.2 shows the effect of the ICP power. In order to generate dense plasma, the ICP power can be increased. The conditions for etching the silicon were selected as 2 Watts of RF power, 11 sccm of O_2 flow, 60 sccm of SF_6 flow, 10 mTorr of pressure, –80^{o}C of the cryogenic temperature and 10 minutes of the etching times. It can be observed that there is threshold power of ICP for etching the silicon. However, it should be noted that randomly generated undesired microcones can be generated in this condition.

Effect of the Oxygen plasma on the condition of the sidewall is depicted in Figure A.3. 500 Watts of ICP power, 2 Watts of RF power, 60 sccm of SF_6 flow, 10 mTorr of pressure, –110^{o}C of the cryogenic temperature and 10 minutes of the etching times were selected as etching parameters. Considering the ratio between the etching gases which are O2 to SF6, only 0.8 percent of difference causes the different profile of the sidewall. This represent that control of the etching profile is very sensitive process.

For the conical shape, higher pressure (50 mTorr) and temperature (–80^{o}C) were considered for the conical shape of the etching profile and suppression of the random generation of the structures in paper 5. However, further increase of the temperature up to –65^{o}C of cryogenic temperature could remove the photoresist as depicted in Figure A.4. Etching variables are considered as 500 Watts of ICP power, 20 Watts of RF power, 20 sccm of O_2 flow, 100 sccm of SF_6 flow, 50 mTorr of pressure and 45 minutes of the etching times. The photoresist could be removed by the oxygen plasma as described in chapter 4.2. However, the result shows the possibility to control the profile of not only the sidewall and bottom surface but also top surface by varying the etching variables.

In summary, etching profile is determined based on the combination of the control variables (ICP power, RF power, O2 flow, SF6 flow, pressure and cryogenic temperature) sensitively. Complex effects between the control variables should be considered in order to find desired etching profile. Even though the process is very sensitive, truncated conical microstructures without randomly generated microstructures and hierarchical conical microstructures are fabricated for controlling the wetting properties.

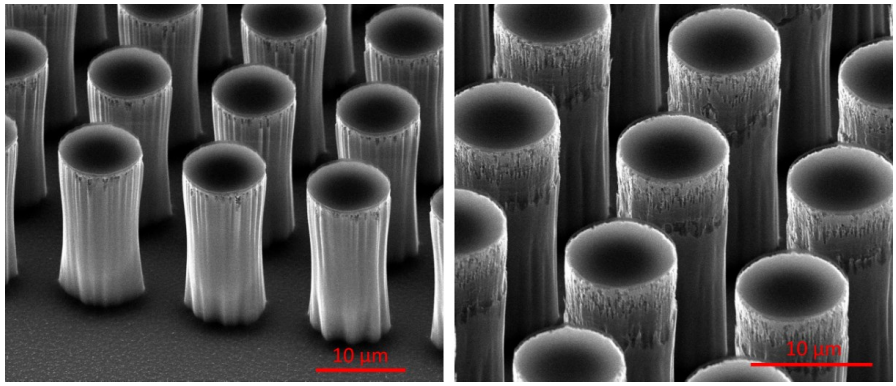

Figure A.1 Effect of the RF power: 4 Watts (left) and 6 Watts (right)

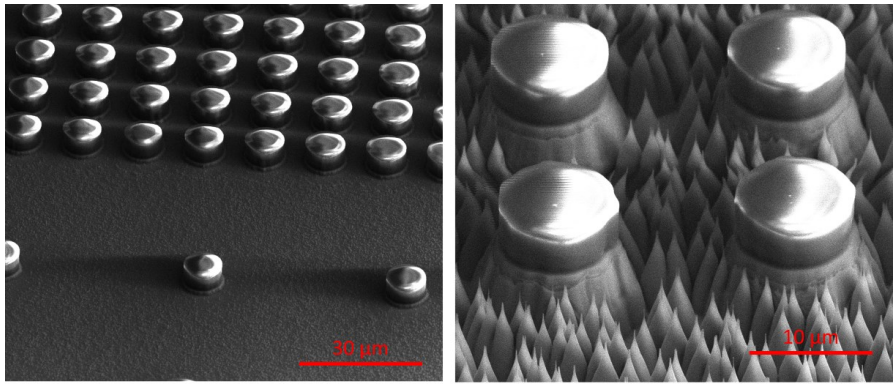

Figure A.2 Effect of the ICP power: 100 Watts (left) and 200 Watts (right)

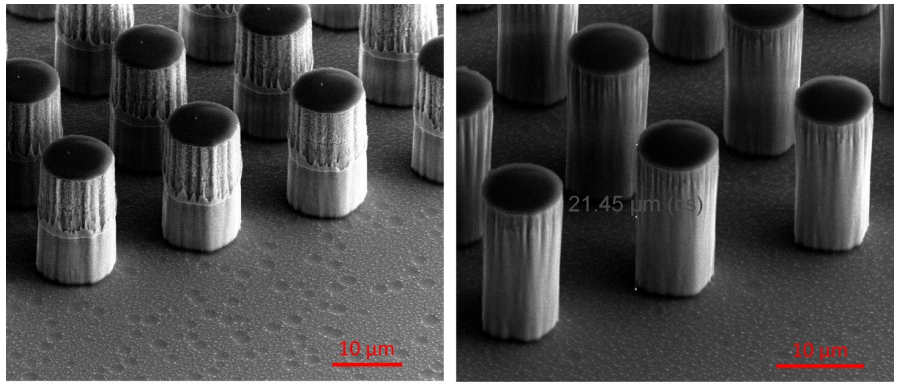

Figure A.3 Effect of the Oxygen flow: 10.0 sccm (left) and 10.5 sccm (right)

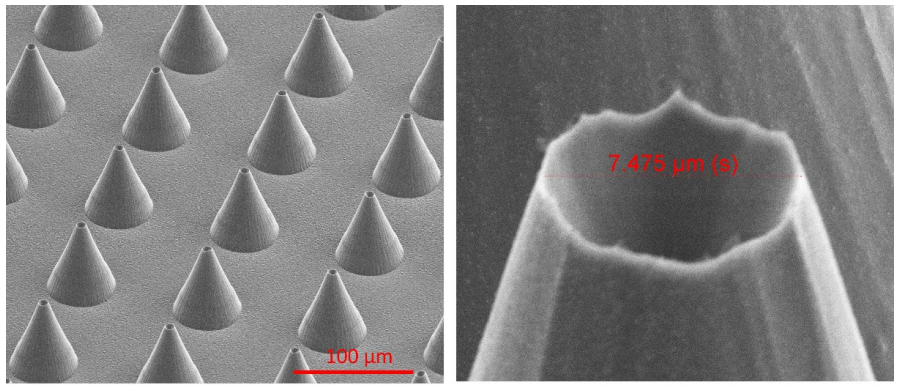

Figure A.4 Conical microstructures without the photoresist on top surface

Appendix B Details of the experiments for two-phase flow instability

This appendix is correspond to the supplementary material for paper 2 and paper 4.

B.1 Experimental setup and procedure

The experimental facility consists of a closed loop consisting of a main tank, a pump, a conditioner, a heated test section, a visualization glass, an adiabatic test section and a condenser. The working fluid (R134a) is circulated by a magnetically coupled gear pump. The pressure in the facility is controlled by the saturation conditions at the store tank. The inlet temperature of the refrigerant before entering the test section is adjusted by a pre-heater that is a shell and tube heat exchanger with glycol in the shell side. A Coriolis mass flow meter is installed before the heated test section. The heated test section is a stainless steel tube with 5 mm inner diameter and 8 mm outer diameter and 2035 mm length (Figure B.1). Joule effect is used for heating the test section with a rectified sine wave and the test section is insulated to reduce heat loss to the surroundings. The heated section is divided into 5 independent sections of 40cm length each. Ten thermocouples are distributed along the outside bottom wall of the test section while there are seven on top. In particular, at 1117 mm and 1917 mm from the inlet thermocouples are installed on top, bottom and sides of the wall plus an inflow internal thermocouple. All the variables are logged with a National Instruments NI RIO data acquisition system. The temperatures, absolute pressures, pressure differences and mass flow rates were acquired at a frequency of 10 Hz.

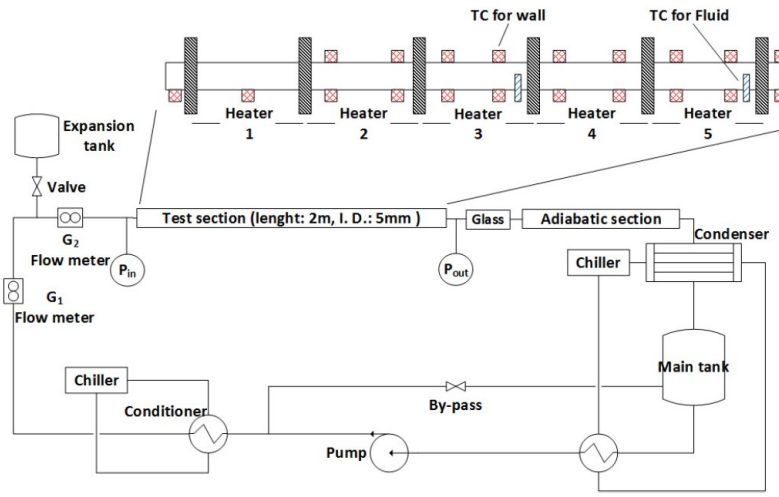

Figure B.1 Sketch of the test facility.

B.2 Measurements and accuracy of measurements

A description of the instrumentation, calibration and characterization of the facility can be found in [B1–B4]. For the temperature measurements, type-T thermocouples with 0.5 mm diameter have been used with an accuracy of 0.1 K (in-house calibration) [B5]. The absolute pressure at the inlet and outlet of the heated section was used for determining the saturation temperature, T_{sat}, of the fluid based on the equilibrium properties calculated with software REFPROP version 9.1 [B6].

The pressure at the inlet and outlet were measured with absolute pressure transducers with an accuracy of 0.04% at full-scale (2500 kPa) given by the supplier. The two-phase total pressure drop along each test section was measured with a differential pressure transducer with an accuracy of 0.075 % at full-scale (50 kPa) given by the supplier. For the heat flux, q", the error coming from the propagation is the error associated with the voltage and current measurements. The thermal heat transfer to the fluid under stationary conditions was calibrated against the electrical value for different temperatures and conditions for single-phase liquid

arriving to a final accuracy of 5% for high heat fluxes and up to 14% for very low heat fluxes. The vapour quality is obtained by performing a heat balance along the test section as shown below

$$x(z) = \frac{\int_{z_0}^{z} q\pi D_i dz - GAcp_l T_{Sub}}{GAh_{lv}} \quad \text{(B.1)}$$

here $x(z)$ is the fluid quality at point z [m] along the heated section, G is the mass flux, A is the cross section area of the pipe, c_{pl} is the liquid phase heat capacity of the fluid, h_{lv} is the enthalpy of vaporization and T_{sub} the inlet subcooling. A mass flow rate accuracy of 0.2% of the reading was given by the supplier.

The local heat transfer coefficient is determined at 1917mm from the inlet by applying the Newton equation

$$h = \frac{q}{T_{W,i} - T_F} \quad \text{(B.2)}$$

where h is the heat transfer coefficient, $T_{w,i}$ is the internal wall temperature which is calculated from the measured outside wall temperature $T_{w,o}$ by applying a one-dimensional, radial, steady-state heat conduction equation for a hollow cylinder with a uniform heat generation and T_f is the fluid temperature measured with the in-flow thermocouple. The heat transfer coefficient will be based on the measurement of the fluid temperature. The outside wall temperature $T_{w,o}$ is measured at 4 positions (top, bottom, left right side of the tube). The mutual measurement difference between the thermocouples was less than 0.4°C.

The experimental heat transfer coefficient presents a mean value of the measurement uncertainty of about 10%, but this can reach up to 30% when the heat is reduced.

B.3 Experimental validation

The reliability of the measurements was first verified comparing the liquid and vapour single-phase heat transfer coefficient measurements against the Dittus-Boelter correlation. The

comparison is presented in Figure B.2 showing a good agreement. The two-phase flow heat transfer coefficient was validated by comparing it to different cases in the literature with similar working conditions. Figure B.3 depicted a comparison of one selected case showing good agreement. Finally, a test of reproducibility of the heat transfer coefficient is presented in Figure B.4 where two data sets are shown corresponding to the same working conditions but measured one month apart.

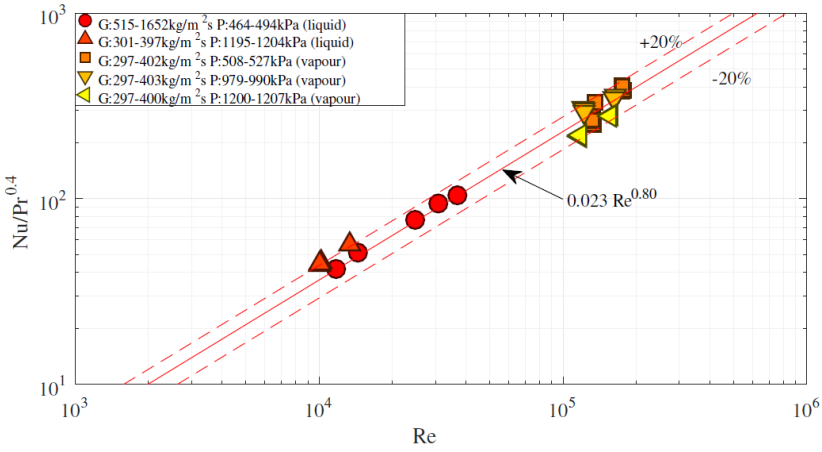

Figure B.2 Single-phase liquid and vapour heat transfer coefficient measurement and prediction by Dittus-Boelter correlation.

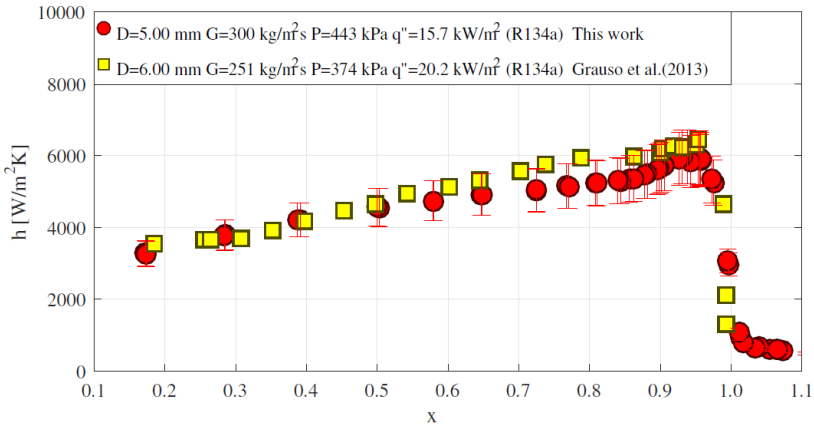

Figure B.3 Comparison of the two-phase flow heat transfer coefficient to a similar case form the literature.

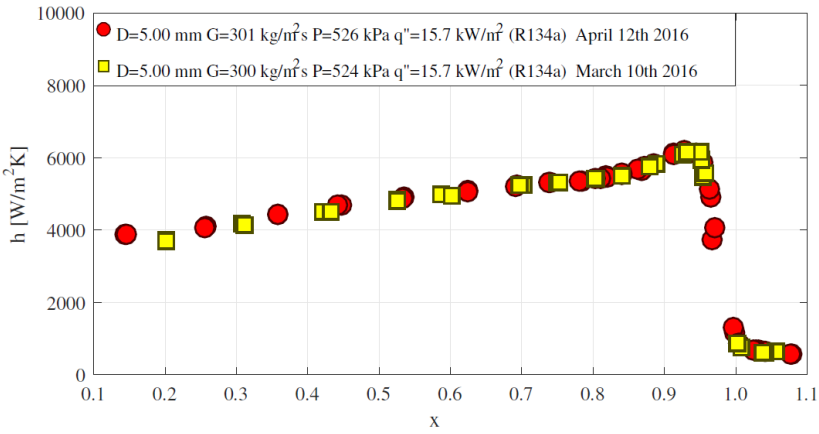

Figure B.4 Test of repeatability of the heat transfer coefficient.

B.4 Experimental method

For each experiment, the pressure at the outlet of the heated section was kept constant. Before starting recording data for each point, extreme care was taken to assure that steady-state

conditions were established. Steady-state conditions were declared when the variation in the time-averaged values of both the mass flux, pressures, and inlet temperature varied less than 6% for about 200 seconds. For each point, about 100 s were recorded corresponding to about 1000 points.

For the experiments, the facility was first heated up with the maximum planned power in the heated section. Each experimental point was then obtained by decreasing the applied electrical heat for each point. This procedure avoids the jump in the wall temperature that is observed for example when the onset of nucleate boiling (ONB) occurs or changes of the flow pattern. This approach allows a good repeatability of the experiments reducing the dispersion of the data.

[B1] Chiapero, E. M., Doder, D., Fernandino, M., & Dorao, C. A. (2014). Experimental parametric study of the pressure drop characteristic curve in a horizontal boiling channel. *Experimental Thermal and Fluid Science*, 52, 318-327.

[B2] Sørum, M., & Dorao, C. A. (2015). Experimental study of the heat transfer coefficient deterioration during Density Wave Oscillations. *Chemical Engineering Science*, 132, 178-185.

[B3] Dorao, C. A. (2015). Effect of inlet pressure and temperature on density wave oscillations in a horizontal channel. *Chemical engineering science*, 134, 767-773.

[B4] Dorao, C. A., Langeland, T., & Fernandino, M. (2017). Effect of heating profile on the characteristics of pressure drop oscillations. *Chemical Engineering Science*, 158, 453-461.

[B5] Chiapero, E. M., Fernandino, M., & Dorao, C. A. (2014). Experimental results on boiling heat transfer coefficient, frictional pressure drop and flow patterns for R134a at a saturation temperature of 34° C. *International Journal of Refrigeration*, 40, 317-327.

[B6] Lemmon, E. W., Huber, M. L., & McLinden, M. O. (2002). NIST reference fluid thermodynamic and transport properties—REFPROP. *NIST standard reference database*, 23, v7.